UNIVERSIDAD DE CHILE
FACULTAD DE CIENCIAS FÍSICAS Y MATEMÁTICAS
DEPARTAMENTO DE ASTRONOMÍA

EXOPLANET DETECTION AND CHARACTERIZATION USING BAYESIAN FORMALISMS

TESIS PARA OPTAR AL GRADO DE
DOCTOR EN CIENCIAS, MENCIÓN ASTRONOMÍA

JOSÉ IGNACIO VINES LÓPEZ

PROFESOR GUíA:
RICARDO MUÑOZ VIDAL
PROFESOR CO-GUíA:
JAMES JENKINS FISHER

MIEMBROS DE LA COMISIÓN:
DAVID ANDERSON
PATRICIO ROJO RUBKE
VALENTINO GONZALEZ CORVALÁN
MIKKO TUOMI

Este trabajo ha sido parcialmente financiado por CONICYT-PFCHA/Doctorado Nacional-21191829

SANTIAGO DE CHILE
2023

RESUMEN DE LA TESIS PARA OPTAR
AL GRADO DE DOCTOR EN CIENCIAS, MENCIÓN ASTRONOMÍA
POR: JOSÉ IGNACIO VINES LÓPEZ
FECHA: 2023
PROF. GUÍA: RICARDO MUÑOZ VIDAL

DETECCIÓN Y CARACTERIZACIÓN DE SISTEMAS EXOPLANETARIOS UTILIZANDO FORMALISMOS BAYESIANOS

Esta tesis se basa en cuatro artículos científicos de primer autor. Primero, describo el descubrimiento de un exoplaneta tipo Júpiter caliente con un período orbital ultra-corto alrededor de la estrella tipo K NGTS-6, con un período orbital de solo 21.17 horas. El análisis muestra que NGTS-6b tiene una masa y un radio de 1.33 M_J y 1.27 R_J, respectivamente, lo que resulta en una densidad de 0.71 $g\,cm^{-3}$. Se estudió la correlación entre las velocidades radiales y el índice de actividad conocido como BIS, concluyendo que no hay correlaciones. Dada la naturaleza extrema del sistema, estudiamos los efectos de la fotoevaporación en el planeta, encontrando que a lo largo de los 9.5 Gyr de años de evolución del sistema, NGTS-6b debe haber perdido el 5% de su atmósfera gaseosa. NGTS-6b se suma a la corta lista de gigantes gaseosos con períodos ultra-cortos y es un excelente candidato para estudios de decaimiento por mareas.

El segundo artículo consiste en un nuevo algoritmo, llamado `ARIADNE`, para el modelado de la distribución de energía espectral (SED) utilizando formalismo Bayesiano, específicamente, el promedio Bayesiano de modelos. El algoritmo consta de ajustar diferentes modelos de atmósferas estelares a la fotometría disponible públicamente y calcular la evidencia Bayesiana correspondiente a cada modelo. Luego se realiza un promedio Bayesiano sobre los modelos, utilizando la probabilidad de cada uno como peso estadístico durante el promedio. Como resultado, se obtienen distribuciones más robustas para cada parámetro de interés, particularmente la temperatura superficial y el radio estelar, resultando en un método cuasi-agnóstico con respecto a los modelos.

Esta metodología fue probada con 135 estrellas observadas con interferometría que cubren el rango espectral A a M, y a través de seis diferentes modelos de atmósfera. Encontramos discrepancias que llegan hasta 0.6 $R_\odot$ en radio estelar, una diferencia tal tiene un efecto del 60% en el radio de un posible planeta, negando completamente la homogeneidad al combinar resultados con diferentes modelos. Las estrellas más pequeñas que $0.4 - 0.5\ R_\odot$ muestran una tendencia creciente con la disminución del radio donde `ARIADNE` sobreestima el radio en comparación con el valor derivado de la interferometría. Esto muestra que aún se necesita más trabajo para modelar mejor estas estrellas. `ARIADNE` ya ha sido utilizado en la comunidad en varios descubrimientos de exoplanetas, junto con otros usos fuera de la ciencia planetaria.

Finalmente, el nuevo algoritmo de Promediación de Modelos Bayesianos se aplicó para calcular los parámetros de las estrellas huéspedes de 2 nuevos exoplanetas que descubrí. HD 18599 b es un planeta joven (300 Myr) que orbita una estrella altamente activa. El descubrimiento se hizo principalmente utilizando datos de *TESS* y velocidades radiales obtenidas con HARPS. HD 18599 b tiene una densidad inusualmente alta de $7\pm1\ g\,cm^{-3}$, y los modelos de composición sugieren que tiene un 23% de agua y un 77% de roca y hierro en su núcleo. Estudios posteriores de la fracción de masa de agua (WMF) revelaron que HD 18599 b tiene una WMF de 0.3 ± 0.1, sin embargo, la fracción de masa del núcleo de hierro sigue sin estar restringida. Este planeta existe en el límite del Desierto de Neptuno y es el primer planeta joven de su tipo en habitar esta región.

NGTS-Nb es un Júpiter caliente identificado inicialmente por *TESS*, y fue descubierto de manera independiente con NGTS. Orbita a su estrella anfitriona en 4.16 días y tiene una masa y radio de 1.12 M_Jy 1.61 R_J respectivamente, lo cual está significativamente inflado considerando que los modelos de inflación predicen un radio de 1.13 R_J. NGTS-Nb destaca entre las estrellas con radios similares al orbitar una estrella que es significativamente más fría que sus pares, lo que sugiere que el planeta podría estar experimentando una re-inflación ahora que la estrella anfitriona está entrando en la rama subgigante.

RESUMEN DE LA TESIS PARA OPTAR
AL GRADO DE DOCTOR EN CIENCIAS, MENCIÓN ASTRONOMÍA
POR: JOSÉ IGNACIO VINES LÓPEZ
FECHA: 2023
PROF. GUÍA: RICARDO MUÑOZ VIDAL

EXOPLANET DETECTION AND CHARACTERIZATION USING BAYESIAN FORMALISMS

This thesis is based on four first-author scientific articles. First, it describes the discovery of a hot Jupiter exoplanet with an ultra-short period orbiting the old K-type star NGTS-6, with an orbital period of just 21.17 hours. The analysis shows that NGTS-6b has a mass and radius of 1.33 M_J, and 1.27 R_J, respectively, resulting in a density of 0.71 $g\,cm^{-3}$. The correlation between radial velocities and the activity index known as BIS was studied, concluding that there are no correlations, supporting the hypothesis of the planetary origin of the signal. Given the extreme nature of the system, we studied the effects of photoevaporation on the planet, finding that over the 9.5 billion years of system evolution, NGTS-6b must have lost 5% of its gaseous atmosphere. NGTS-6b is added to the short list of gas giants with ultra-short periods and makes for an excellent candidate for tidal decay studies.

The second article consists of a new automatic algorithm, called `ARIADNE`, for the modeling of the spectral energy distribution (SED) using a Bayesian formalism, specifically, the Bayesian average of models. The algorithm involves fitting different grids of stellar atmosphere models to publicly available photometry and calculating the Bayesian evidence corresponding to each model. A Bayesian average is then performed over the models, using the probability of each one as a statistical weight during the average. As a result, more robust distributions are obtained for each parameter of interest, particularly the surface temperature and the stellar radius, resulting in a quasi-agnostic method with respect to the models.

This methodology was tested with 135 stars with interferometry observations covering the spectral range from A to M dwarfs, and across six different atmosphere model grids. We found differences reaching up to $0.6 R_\odot$ in radius, such an offset would give rise to a difference in planetary radius of 60%, completely negating homogeneity when combining results with different models. Stars smaller than $0.4 - 0.5 R_\odot$ show an increasing trend with decreasing radius where `ARIADNE` overestimates the radius compared to the interferometrically-derived parameter. This shows there is still more work needed to be done to better model these stars. `ARIADNE` has already been used in the community in several exoplanet discoveries, along with other uses outside planetary science.

Finally, the new Bayesian Model Averaging algorithm was applied to precisely constrain the host parameters of 2 new exoplanets I discovered, revealing some very interesting planetary properties: HD 18599 b, and NGTS-Nb. HD 18599 b is a young planet (300 Myr) orbiting a highly active star. The discovery was made primarily using TESS data and radial velocities obtained with HARPS. HD 18599 b has an unusually high density of 7 ± 1 $g\,cm^{-3}$, and composition models suggest that it has 23% water and 77% rock and iron in its core. Further studies of the water mass fraction (WMF) revealed HD 18599 b has a WMF of 0.3 ± 0.1, yet the iron core mass fraction is still unconstrained. This planet exists on the edge of the Neptune Desert and it is the first young planet of its type to inhabit this region.

NGTS-Nb is a hot Jupiter first identified by *TESS*, and it was independently discovered with NGTS. It orbits its host star in 4.16 days and has a mass and radius of 1.12 M_J, and 1.61 R_J respectively, which is significantly inflated considering inflation models predict a radius of 1.13 R_J. NGTS-Nb stands out amongst planets with similar radii by orbiting a star that is significantly colder than its peers, which suggests the planet might be undergoing re-inflation now that the host star is entering the subgiant branch.

to myself

Acknowledgements

First, I would like to thank James for his willingness to hand out a project to an up-and-coming undergrad student, and afterward, for his advice, guidance, and trust in me for pursuing the Ph.D. under his supervision. I would like to thank David Anderson for motivating me by the end of this journey to continue pursuing astronomy, and Maximiliano Moyano for giving me the opportunity to do this as a Postdoc. Last but not least I would like to thank Ricardo Muñoz for all of those Pokemon Go battles at Calán, pleasant conversations and useful advice.

Thanks to Javier Alarcón, a TIO at La Silla Observatory, for providing invaluable support at the telescope during the hardest time in my Ph.D., and of course for all of those hours of fun conversations and video games at the observatory. Thanks to the 2.2-m MPG/ESO telescope staff for teaching me how to use the telescope, and for carrying on observations remotely after the pandemic restrictions had passed.

To my dearest friends from my time as an undergrad at Universidad de Chile. Checho, Manu, Rodrigo, Esteban, Cris, Tere V and Tere P. I wouldn't be here without all of your support and friendship and I will always cherish those countless hours studying and doing our Classical Mechanics homework, and really, every other great times we had, which are quite numerous to write here.

To the friends I made at Calán; Dani, Patits, Carla, Jonathan, Blake, Richi, Nina, Sudeep, Nathan, and Pablo. It was awesome going to Calán and not getting any work done because of how easily distracted I am. I'll always look fondly to our conversations. To Matías with whom I shared my passion for photography, my frustrations with academia, and his valued advice as a senior Ph.D. student.

To Sebita, Tami, Negro, Pepe, Pancho, and Checho (again), for being there almost daily during the pandemic and being one of the biggest sources of support, laughter, memes, and general bullshittery during tough times.

To my mom and Sergio who played a fundamental role in making me the human being I am today. I will be forever thankful for everything you have done, and continue to do for me. To my dad and Areli, for their precious experience in academia and for being there for me whenever I needed them. To my sister who I will forever tease.

To Camila, the best partner I could have found in life, and her infinite patience with me.

Table of Content

List of Tables

List of Figures

Chapter 1

Introduction

1.1 A Brief History of Exoplanets

Exoplanets, worlds beyond the realm of our Solar System, have captivated scientists and the general public alike. The concept of planets orbiting other stars has been speculated about for centuries. Such planets were first hinted at in 1988 with γ Cephei Ab (Campbell et al. 1988), which was later confirmed by Hatzes et al. (2003) and in 1992 two planets were discovered orbiting the pulsar PSD 1257+12 (Wolszczan & Frail 1992), but it was not until 1995 that the exoplanet race truly began with the discovery of 51 Peg b, a Hot Jupiter orbiting a Sun-like star (Mayor & Queloz 1995). The leading discovery method was the radial velocity method until 2003 when the first exoplanet discovery was made with the transit method, OGLE-TR-56b (Konacki et al. 2003). Since then, developments in instrumentation (Vogt 2002; Pepe et al. 2002; Crane et al. 2010; Quirrenbach et al. 2016; Pepe et al. 2020) and analysis techniques (Anglada-Escudé et al. 2013; Tuomi et al. 2014; Feng et al. 2017; Ahrer et al. 2021) have allowed the discoveries of massive Jupiter-sized planets all the way down to planets similar in mass to Earth (Mayor et al. 2009; Vogt et al. 2010; Tuomi et al. 2014; Gilbert et al. 2020). In total more than 5000 exoplanets have been confirmed to date (Figure 1.1), and one thing has been abundantly clear, exoplanets do not adhere to either the individual or system properties extrapolated from the known architecture of our Solar System. For example, orbital properties vary widely with many exoplanets having elliptical orbits ($e \geq 0.3$) for example. Others similar to Jupiter in size orbit their host star much closer than Mercury does the Sun, painting an in-situ formation scenario unlikely.

Not five years after the discovery of 51 Peg b, the first transits were detected on a Hot Jupiter, HD 209458 b (Henry et al. 2000; Charbonneau et al. 2002), a discovery that ushered in a new era in the study of gas giants, since now their radii, and therefore their densities could be measured. Motivated by this, wide-field ground-based surveys were set up, such as WASP and NGTS (Pollacco et al. 2006a; Wheatley et al. 2018), significantly increasing the number of gas giants around bright stars. Now we know that, while easier to find, Hot Jupiters are quite rare, with about 1% of Sun-like stars hosting them (Wright et al. 2012; Zhou et al. 2019).

In addition to studying their orbital properties, we also aim to study their atmospheres. The two

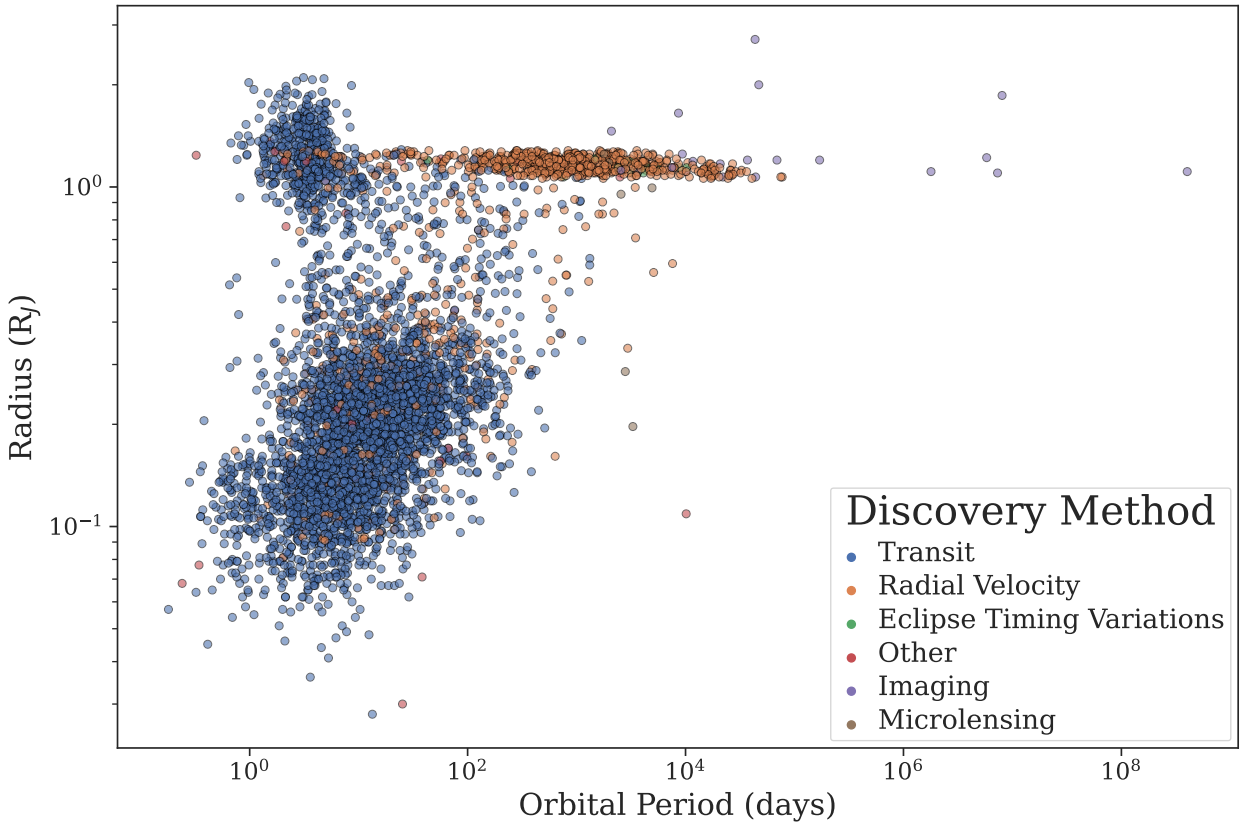

Figure 1.1: Radius-period diagram for discovered planets with measured radii colored by discover method from the NASA Exoplanet Archive Composite Data. The legend is limited to the main discover methods with the two most relevant ones being transit (blue points) and radial velocities (orange points). From the figure, it is evident that radial velocity detections are biased towards massive, Jupiter-sized planets, while transit detections are biased towards low-period companions. It's also important to note that smaller, longer-period planets are rarer, due to the transit probability being dependent on the orbital period, and the Keplerian signal being highly dependent on the planetary mass.

most studied planets in this aspect are HD 189733 b (Bouchy et al. 2005) and HD 209458 b. The latter was the first exoplanet on which elements and molecules (Na and CO) were detected escaping its atmosphere (Charbonneau et al. 2002). Other atomic metals have been observed in the UV and optical, and through these features, we have learned that Hot Jupiters typically have low geometric albedos, lower than 0.1 (Esteves et al. 2015; Parmentier et al. 2016), much lower than our own Jupiter's albedo of ~ 0.5. Instruments such as *Hubble* have detected water vapor in several objects (Kreidberg et al. 2015; Sing et al. 2016), and sometimes reaching high enough SNR to determine the water mixing ratio. Photometry from *Spitzer* in the 3.6 and 4.5 μm bands have shown evidence for CO and CO_2 absorption (Stevenson et al. 2017). Higher resolution transmission spectroscopy has shed light on atmospheric dynamics, allowing us to assess the velocity and direction of atmospheric flow (Flowers et al. 2019).

There are three main hypotheses to explain how Hot Jupiters came to orbit so close to their host stars: in-situ formation, disk migration, and high eccentricity migration. In-situ formation requires that Hot Jupiters form their cores and accrete their atmospheres at their current location, while migration hypotheses posit that the planets formed far away from the star and either migrated inward through the gaseous disk surrounding a young star or after the disk has dissipated, a jovian planet far from its star would be pushed into a highly elliptical orbit and making it migrate through tidal dissipation. While the three scenarios described are theoretically viable, no single one successfully reproduces the observed distribution of Hot Jupiters.

For a giant planet to form, a rocky proto-planet core needs to accrete several times its mass in gas from the surrounding protoplanetary disk Pollack et al. (1996), or gravitational instability, where part of the proto-planetary disk fractures into clumps (Durisen et al. 2007). At typical Hot Jupiter periods ($\sim$ 3 days), gas conditions prevent gravitational instability (Rafikov 2005), while core accretion becomes immensely challenging. In-situ formed Hot Jupiters are expected to be formed at $\sim$ 10 days (Lee & Chiang 2017).

Clues to the formation mechanisms at play come from the observed eccentricity distributions from Hot Jupiters. At the shortest orbital periods, most Hot Jupiters have circular orbits, while at longer periods (3-10 days) there is a mixture of circular orbits and moderate eccentricities that can reach up to 0.6. This suggests a mixture of in-situ and migration scenarios for formation channels. A planet's misalignment with the spin of its host star, however, is not an indication of its formation pathway. It would be expected that planets formed in-situ or through disk migration have their orbits aligned with the host star rotation, yet it has been observed that many Hot Jupiters have heavily misaligned orbits (Albrecht et al. 2012), a result consistent with high eccentricity migration mechanism (Chatterjee et al. 2008), yet tidal interactions can realign the orbit (Albrecht et al. 2012), wiping away the evidence for high eccentricity migration. Other physical processes can misalign the orbit further (Storch et al. 2014).

Other Hot Jupiter characteristics we have uncovered serve to test the different formation mechanisms. For instance, we have learned that giant planet occurrence is a function of the metallicity of the host star (Fischer & Valenti 2005), with this correlation being even stronger for Hot Jupiters (Jenkins et al. 2017), supporting in-situ formation or high eccentricity migration theories directly. Recently, however, it has been found that the planetary metallicity does not need to correlate with

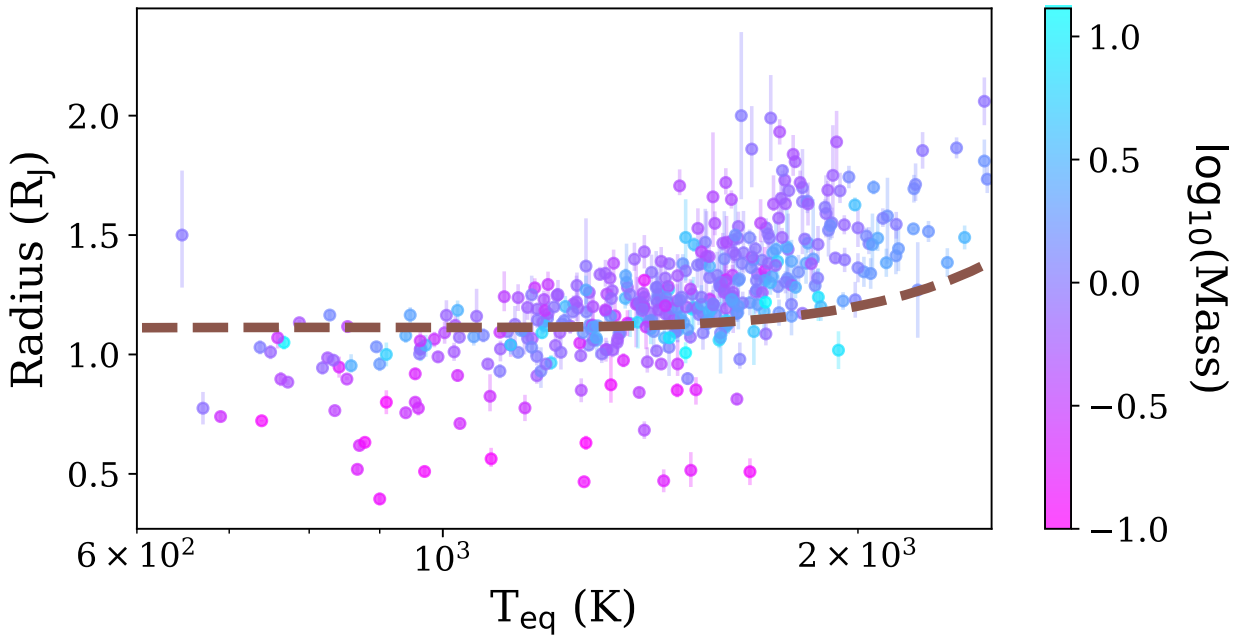

Figure 1.2: Exoplanets with masses ranging from 0.1 to 13 M_J, where both the masses and radii are determined to better than 20% precision taken from TEPCat (Southworth 2011). Each planet has been color-coded by its mass in $\log_{10}$ scale. The dashed line shows an evolutionary model from Thorngren & Fortney (2018) for a Jovian planet without inflation-inducing effects, with an age of 4.5 Gyr.

the stellar metallicity (Teske et al. 2019).

Even though we have learned a lot about gas giants, there are still more mysteries regarding the mechanism behind their formation and evolution yet to be uncovered. For instance, an even more extreme population of ultra-short period Hot Jupiters has been emerging (Southworth et al. 2009, 2015; Penev et al. 2016; Oberst et al. 2017; Vines et al. 2019; McCormac et al. 2020), which have opened a window to studying star-planet tidal interactions and orbital decay, the latter being a particularly starved area of study with just the one planet showing strong evidence for orbital period variations (Patra et al. 2020). An interesting result of Hot Jupiters planet-star interactions is the radius anomaly (Figure 1.2), a higher than-predicted increase in radius on planets that present higher incident flux from their host stars. Multiple mechanisms have been proposed to explain the radius anomaly, such as Hot Jupiters having an increased atmospheric opacity (Burrows et al. 2007), having double-diffusive layered convection interiors (Kurokawa & Inutsuka 2015), or tidal circularization of Hot Jupiters (Bodenheimer et al. 2001; Leconte et al. 2010). These are not all the proposed mechanisms, and we invite the reader to see Fortney et al. (2021) for a more comprehensive review. While there might be multiple effects at play (Sarkis et al. 2021), there is one effect that seems to dominate the radius inflation: incident stellar flux (Weiss et al. 2013; Thorngren & Fortney 2018).

There have been significant efforts in creating statistical and physical models and studies in recent years that aim to characterize the underlying relationship between radii inflation, incident flux, and other proposed mechanisms (e.g. Baraffe et al. 2008; Thorngren et al. 2016; Sestovic et al. 2018; Komacek et al. 2020; Sarkis et al. 2021).

On the opposite side of the spectrum are the elusive Warm Jupiters, a population of gas giant planets with orbital periods ranging from the tens to hundreds of days (e.g. Díaz et al. 2020a; Gill et al. 2020; Jordán et al. 2020a). Even though they are similar in mass to their short-period counterpart, the formation scenarios of these two populations need not be the same. Indeed, the origins of hot and warm Jupiters is an area of intense study and debate. A planet's dynamical properties (Triaud 2018) and atmospherical chemical composition (Öberg et al. 2018) are expected to relate to its formation and evolution history. For example, disk migration is expected to produce planets with low orbital eccentricities and obliquities far more than are high-eccentricity tidal migration mechanisms (Dawson & Johnson 2018), and a planet's atmospheric C/O ratio is thought to be able to provide constraints on where and how it formed (Öberg et al. 2018).

Unlike their Hot Jupiter counterparts, when we move downwards in mass and radius scale, we encounter a region mainly devoid of planets, an area known as the Neptune Desert. This region of the parameter space is 'dry' but it is not completely empty (see Figure 1.3).

While Neptune-sized planets are fairly common and abundant (e.g., Espinoza et al. 2016; Luque et al. 2019; Mayo et al. 2019; Palle et al. 2019), this is not true in the short-period regime ($P \leq 4$ days). This paucity is called the Neptune Desert. While the Neptune Desert is 'dry', it is not completely devoid of planets. Recently a few planets have been discovered that orbit close to their host stars with masses and radii in the desert (see Figure 1.3 West et al. 2019; Jenkins et al. 2020b; Armstrong et al. 2020).

1.2 Transiting Exoplanet Survey Satellite

The Transiting Exoplanet Survey Satellite (*TESS*) is a NASA-funded MIT-led space-based mission dedicated to the detection and characterization of exoplanets through the transit method (Ricker et al. 2015). *TESS* follows on from the success of the *Kepler*/K2 missions, and it was launched on April 18, 2018. *TESS* is equipped with four wide-field-of-view CCD cameras, each with a 24×24 deg^2 field of view, which together cover a 96×24 deg^2 region of the sky in a single observation. It has a pixel scale of 21×21"/pixel and observes in a red bandpass (600-1000 nm), optimized for detecting small exoplanets around bright, cool stars, such as M dwarfs. Each observation is aligned to cover strips of the sky called *TESS* sectors, each one spanning 27.4 days, after which the data is transferred to Earth for processing (see Figure 1.4).

In each sector, *TESS* produces over ~19,000 sets of 2-minute images called *TESS* pixel files (TPFs), alongside ~1,200 sets of 30-minute Full Frame Images (FFIs). The data is then processed into calibrated light curves by two pipelines. The Science Processing Operations Center (SPOC, Jenkins et al. 2016b, 2020a) for 2-minute cadence images and the MIT Quick Look Pipeline (QLP, Huang et al. 2020a,b) for the FFIs.

The primary goal of the *TESS* mission is to discover Earth-sized and super Earth-sized planets (r$\leq 4\ R_\oplus$) transiting stars brighter than V=12. *TESS* aims to detect at least 50 planets of this nature, allowing high-precision Doppler spectroscopy to measure precise masses (Level 1 Science Requirement). Following the successful completion of the two-year primary mission, an extended mission began on July 2020. During the extended mission, *TESS* introduced shorter 20-second

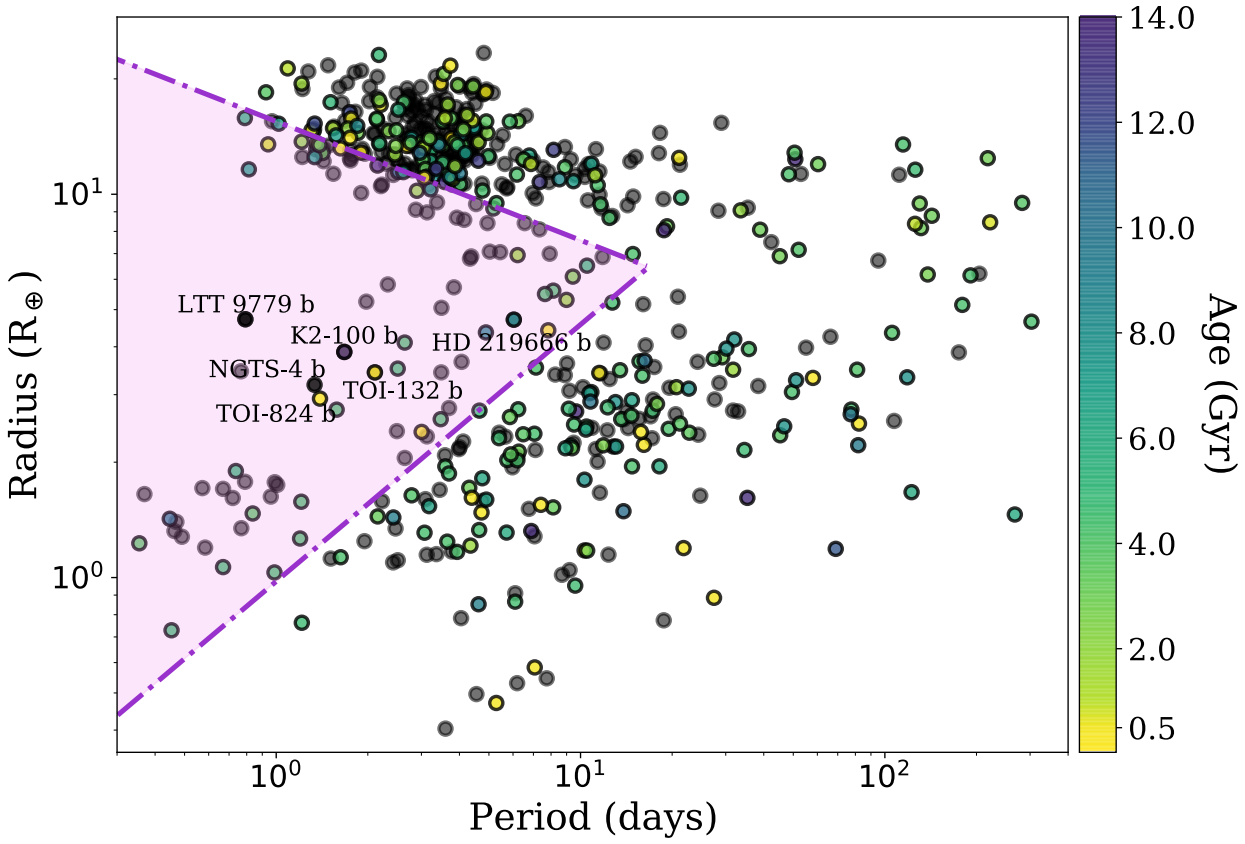

Figure 1.3: Period-radius diagram for planets with radii measured to a precision better than 5%. Relevant discoveries are named. The pink shaded area shows the Neptune desert, with the edges defined by Mazeh et al. (2016). The colors show the ages of the systems and black shows systems without an estimated age. Ages have not all been measured in a uniform way.

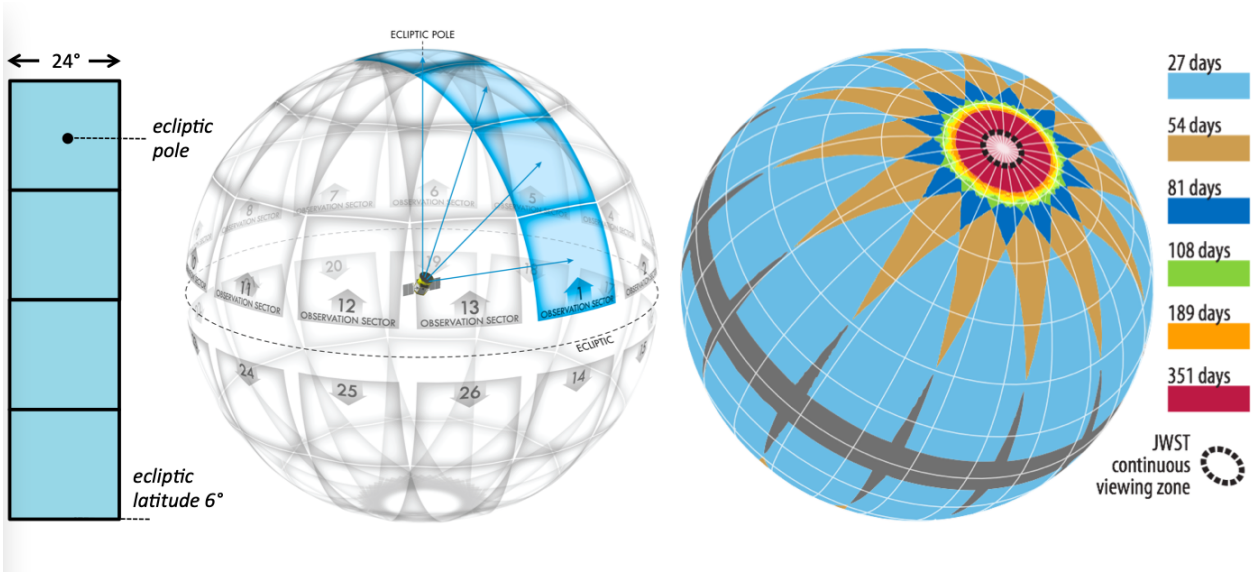

Figure 1.4: Diagram showing the sky coverage of the TESS spacecraft. A sector is composed of the images of the 4 cameras. Each sector overlaps with the previous enabling the detection of planets with periods longer than the 27-day baseline of each sector. Image from Ricker et al. (2015).

exposure TPFs and 10-minute FFIs, which enable easier detection of ultra-short period planets. The extended mission also includes additional observations of the ecliptic plane, which were not covered during the primary mission.

To date, more than 6,000 planet candidates have been identified[1] with 331 confirmed planets. *TESS* expanded the number of small planets around cool stars, and combining these results with the detections from *Kepler*, there is a striking planet population that emerges when studying the planet mass vs radius plane. One of the most surprising is the large population of planets with sizes between Earth and Neptune, a population that is completely absent from our Solar System.

[1] https://exoplanetarchive.ipac.caltech.edu/cgi-bin/TblView/nph-tblView?app=ExoTbls&config=TOI

1.3 The Next Generation Transit Survey

The Next Generation Transit Survey (NGTS; Wheatley et al. 2018) is an advanced ground-based wide-field survey designed to search for small transiting exoplanets around bright stars. The survey builds on the legacy of previous ground-based surveys, most notably WASP (Pollacco et al. 2006a). The facility is based on the Paranal Observatory in Chile. It employs an array of 12 fully robotic small 20cm, f/2.8 telescopes which have been fitted with a back-illuminated 2K×2K deep-depleted Andor IKon-L CCD camera with a 96% peak quantum efficiency (See Figure 1.5). Each telescope has a custom filter designed to operate in red light in the wavelength range of 520-890 nm, maximizing sensitivity towards late K and early M stars over an instantaneous field of view of 100 deg^2.

Figure 1.5: The NGTS telescope array at the Paranal Observatory.

The NGTS consortium operates the telescopes robotically, with observations conducted automatically based on a pre-defined observing strategy. Observations are prioritized by target brightness, sky position, and the likelihood of detecting small exoplanets. The system has been designed to achieve a photometric precision of 1 mmag for stars brighter than 13th magnitude, allowing for the detection of Neptune-sized planets and smaller.

The NGTS data processing pipeline is divided into several steps, including image calibration, astrometric and photometric reduction, and transit search and vetting. NGTS observations are detrended nightly using an adapted version of the SysRem algorithm (Tamuz et al. 2005), after which aperture photometry extraction is performed using the CASU Tools photometry package. The processed light curves are searched for transit-like signals using `ORION`, a modified Box Least Squares algorithm (Kovács et al. 2002; Collier Cameron et al. 2006). Candidate signals are identified based on their transit depth, duration, periodicity, and signal detection efficiency (Pope et al. 2016).

These candidates are then subjected to a series of vetting procedures, including the examination of odd-even transit depth differences, transit shape analysis, and centroid motion analysis. This vetting process helps to distinguish genuine exoplanet transits from false positives caused by eclipsing binaries, background stars, and instrumental artifacts.

Given the significant difference in pixel size (5×5" as opposed to the 21×21" of *TESS*), NGTS is less affected by blending due to background stars. This allows NGTS to follow up candidates in crowded fields, and to detect blended eclipsing binary false-positives within the TESS Objects of Interest. Additionally, NGTS has a significantly higher cadence than the 10-minute *TESS* FFIs, an important factor in resolving and sampling transits in ultra-short period planets and Hot Jupiters, which can be of the order of 1 hour. Not only ultra-short periods benefit from NGTS observations, but single transit features in TESS light curves, termed monotransits, are prime candidates for continuous observations from NGTS, which significantly increases the chances of capturing additional transits and finally solving the periods for these candidates.

NGTS has led to the discovery of 25 systems, including NGTS-4b, a sub-Neptune in the desert (West et al. 2019), two ultra-short period planets, including the one with the shortest orbital period discovered to date, NGTS-6b and NGTS-10b (Vines et al. 2019; McCormac et al. 2020), a tidally locked brown dwarf, NGTS-7Ab (Jackman et al. 2019), the first planet confirmed on the basis of a *TESS* monotransit, NGTS-11b Gill et al. (2020).

In 2019, NGTS started shifting its operations from the survey to pursuing specific goals, splintering the consortium into several sub-programs, or working groups, such as monotransits, focused on following up *TESS* single or duo transit event stars in order to resolve their periods, where I participated in eyeballing and vetting monotransit candidates; clusters, focused on observing open clusters; bright stars, a working group that provided follow-up light curves for several *TESS* discoveries, some of which I previously modeled to assess the quality of the light curves; and follow-up, concerned with providing ground-based follow-up to NGTS discoveries, where I was in charge of leading the FEROS proposals for radial velocity follow-up, an effort that has led to the publication of 10 different systems (Vines et al. 2019; Bryant et al. 2020; Gill et al. 2020; Tilbrook et al. 2021; Jackson et al. 2023).

1.4 Detection Methods

Here we describe the two most relevant methods for detecting exoplanets in this thesis. Radial velocities have been used since the beginning of the field in the early 90s, producing the first discoveries of exoplanets. The transit method is the most successful one, having produced the vast majority of discoveries to date, mainly due to how inexpensive photometric observations are compared to spectroscopic ones.

1.4.1 Radial Velocities

Radial velocity observations have come a long way since the discovery of 51 Peg b (Mayor & Queloz 1995) with the ELODIE spectrograph in 1995. Instruments such as HARPS (Mayor et al. 2003) and ESPRESSO (Pepe et al. 2020) have brought down the precision to below 1 m s^{-1}, allowing the discovery of multiple systems down to super-Earths in mass, and enabling more detailed studies of exoplanet atmospheres.

The way this method works is by observing multiple spectra of a star in order to measure how its velocity changes in time, a change produced by the gravitational effects of an unseen planet orbiting around it.

Two bodies orbiting each other do so around the center of mass, or barycenter, of the system. When one of the bodies is significantly more massive than the other (e.g. a star and a planet), intuitively one might be inclined to make the simplification that said barycenter lies perfectly at the center of the massive body, yet in reality this is seldom the case. Instead, the actual barycenter is sufficiently offset from the interior of the massive body such that there is an actual measurable wobble. Doppler spectroscopy leverages this fact as indirect evidence of a planet orbiting a star by measuring the velocity of the latter in the line of sight of an observer located on Earth. When a source is moving, the light emitted at frequency f will experience a change δf in frequency, so the observer will measure $f + \delta f$.

Translating the problem into the wavelength domain, this effect can be measured directly from the acquired spectrum of the star as the light originally emitted at λ_0, will experience a wavelength shift due to the fact that it is moving with respect to the observer.

This change in wavelength can be written according to

$$\lambda = \lambda_0 \sqrt{\frac{1 - v/c}{1 + v/c}} \tag{1.1}$$

where v is the velocity of the moving source and c corresponds to the speed of light.

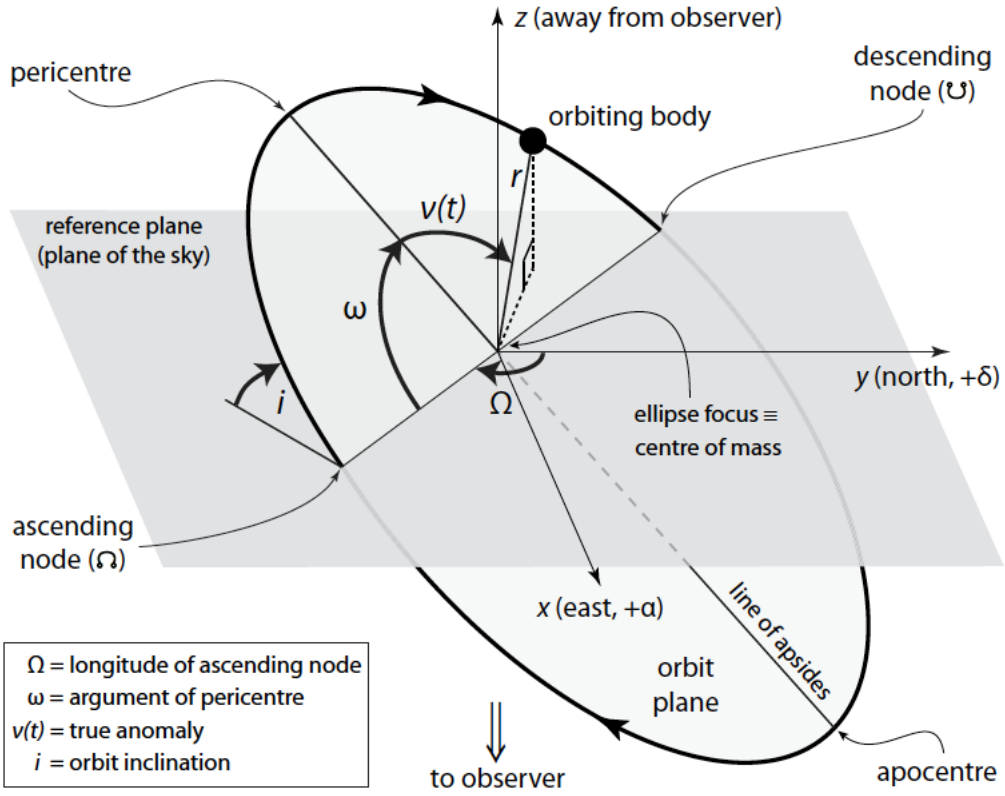

Figure 1.6: Radial velocity orbital diagram showing the orbital elements of a body (planet) moving in an elliptical orbit. The reference plane is tangent to the celestial sphere. Ω is the longitude of the ascending node, measured in the reference plane. ω is the fixed angle defining the argument of pericenter relative to the ascending node. $\nu(t)$ is the true anomaly, a time-dependent angle characterizing the position of the object along the orbit. i is the orbital inclination angle with respect to the reference plane, i = 0 deg corresponds to a face-on orbit. Figure from Perryman (2018).

Hence, we rewrite it as

$$\frac{\Delta\lambda}{\lambda_0} = \frac{v}{c} \tag{1.2}$$

Therefore, if the source is moving towards us, we say the light will be blueshifted. On the other hand, if the source is moving away from the observer, the light will instead be redshifted, according to Equation 1.2.

The basic mathematical model of the radial velocity of a star is given by the Keplerian:

$$v_r(t) = K[\cos(\omega + \nu(t)) + \mathrm{e}\cos\omega] + \gamma \tag{1.3}$$

where ω, the argument of periastron, of the star's orbit with respect to the barycenter, $\nu(t)$ is the true anomaly of the orbit at the time of transit, e is the eccentricity and γ is the systemic velocity (or rest frame velocity) of the system (see also Figure 1.6). K corresponds to the radial velocity semi-amplitude given by

$$K = \left(\frac{2\pi G}{P}\right)^{\frac{1}{3}} \frac{M_{\rm p} \sin {\rm i}}{(M_\star + M_{\rm p})^{\frac{2}{3}}} \frac{1}{(1-{\rm e}^2)^{\frac{1}{2}}} \tag{1.4}$$

Where P corresponds to the orbital period of the planet around the star, $M_\star$ and $M_{\rm p}$ are the mass of the star and the mass of the planet, respectively and i is the inclination of the orbital plane with respect to the line-of-sight.

In the case of exoplanets, we can safely assume that $M_{\rm p} \ll M_\star$.

Equation 1.4 shows that the radial velocity of a star strongly depends on the (minimum) mass and period of the planet candidate. A planet like Jupiter on a year orbit around the Sun will produce a semi-amplitude of ~ 28 m s^{-1}, while an Earth-like planet on a 1-day orbit around the Sun translates to a semi-amplitude of just 0.64 m s^{-1}. This sheds light on an inherent bias of radial velocity surveys towards low-period massive planets and highlights the challenges behind the detection of small companions around Sun-like stars.

A more in-depth discussion of the radial velocity method and the intricacies behind the technique and technology that allows for ultra-precise measurements of radial velocities lies outside the scope of this thesis.

Cross-Correlation technique

Once the spectrum of a star has been observed, the radial velocity needs to be extracted. One of the most used techniques (and the one featured throughout this thesis) is the Cross-Correlation Function (CCF), a method that relies on the creation of a numerical binary mask containing the relevant absorption lines for a given stellar type (Queloz 1995). Extracting the radial velocity, v_R, is done by cross-correlating the binary mask with the observed spectra, and then building a final CCF:

$$f_{\rm CC} = f_{\rm CC}(v_R) \propto \int S(\lambda) M(v_R)\, {\rm d}\lambda \tag{1.5}$$

Where the CCF is the result of integrating the product of the observed spectrum, S, multiplied by the binary mask, M, shifted by a velocity v_R.

We can decompose the binary mask as the sum of individual masks, $M_{\rm i}$, each containing a specific absorption line. Then the CCF is rewritten as:

$$f_{\mathrm{CC}} = \int S(\lambda) \sum_{\mathrm{i}} M_{\mathrm{i}}(\lambda_{v_R})\, \mathrm{d}\lambda \tag{1.6}$$

$$= \sum_{\mathrm{i}} f_{\mathrm{CC,i}}(v_R) \tag{1.7}$$

Knowledge of how deep each line is can be incorporated into the CCF by creating a weighted mask instead, producing a weighted CCF, $\mathrm{CCF^W}$, this way deeper lines, which contain more information about the radial velocity, are given more importance than weaker lines, increasing the overall precision of the final radial velocity.

Introducing the $\mathrm{CCF^W}$ modifies Equation 1.7 to become:

$$f^W_{\mathrm{CC}} = \sum_{\mathrm{i}} f_{\mathrm{CC,i}}(v_R)\, c_{\mathrm{i}} \tag{1.8}$$

$$= \int I(\lambda) \sum_{\mathrm{i}} (M_{\mathrm{i}}(\lambda_{v_R})\, c_{\mathrm{i}})\, \mathrm{d}\lambda \tag{1.9}$$

where $I(\lambda)$ corresponds to the continuum intensity in the spectrum and c_{i} is the relative intensity of the i-th absorption line.

Once the final CCF is acquired a Gaussian function is fit to it, after which we find the radial velocity as the lowermost point of said Gaussian (see Figure 1.7).

1.4.2 Transits

The transit method consists of measuring how much the perceived brightness of a star dims due to an unseen companion passing between the stellar disk and our line of sight. This decrease in flux is produced by the companion blocking part of the surface of the star for a short amount of time, a process that repeats with a period equal to the orbital period of the system. Figure 1.8 depicts this idea alongside the geometry of a planet transiting in front of its host star (adapted from Winn et al. 2011). The first planet confirmed to be transiting was HD 209458 b (Charbonneau et al. 2000; Henry et al. 2000), while the first true transit discovery was OGLE-TR-56 b (Konacki et al. 2003).

The main difference between the radial velocity and transit methods is that the former excels in the orbital characterization of the system (e.g. constraining the eccentricity, mean anomaly) and provides an insight into the mass of the companion, while the latter provides the radius and orbital inclination. In conjunction, the companion is fully characterized, providing bulk densities and orbital configurations.

The radius of the planet can be directly related to the depth of the transit, δ, by

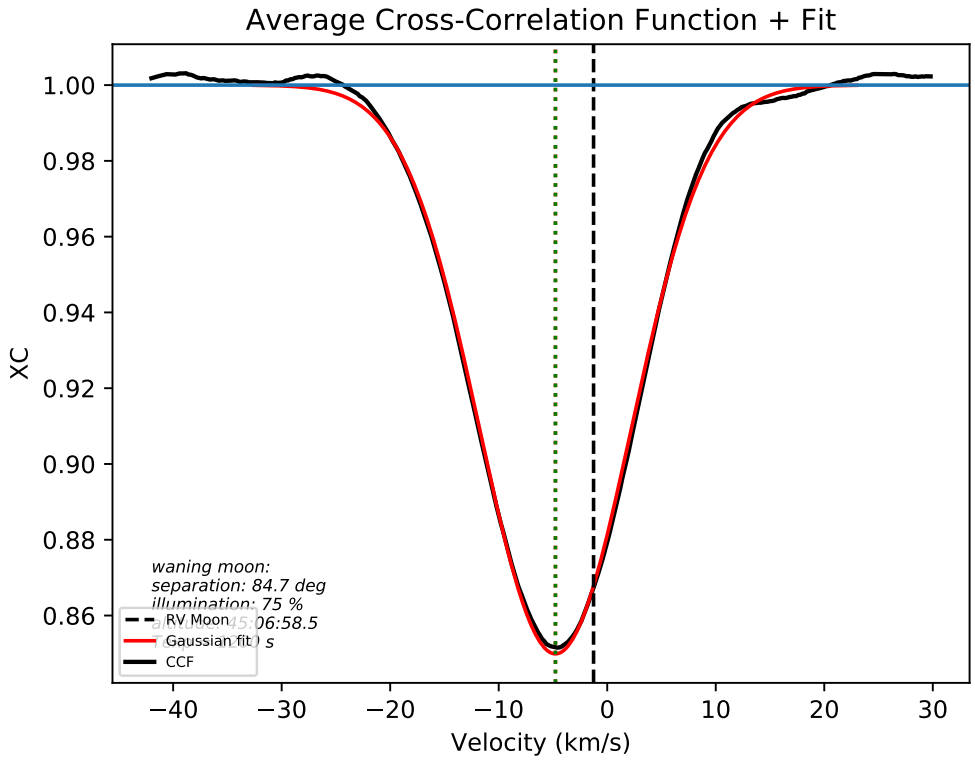

Figure 1.7: Example of a CCF extracted from a FEROS spectrum. The solid black line shows the computed CCF and the red line shows the Gaussian fit. The dashed black line shows the predicted contribution to the CCF by sunlight reflected by the Moon, which is computed by first calculating the coordinates of the moon at the time of observations, and estimating the radial velocity at which the solar spectrum should show up in the CCF.

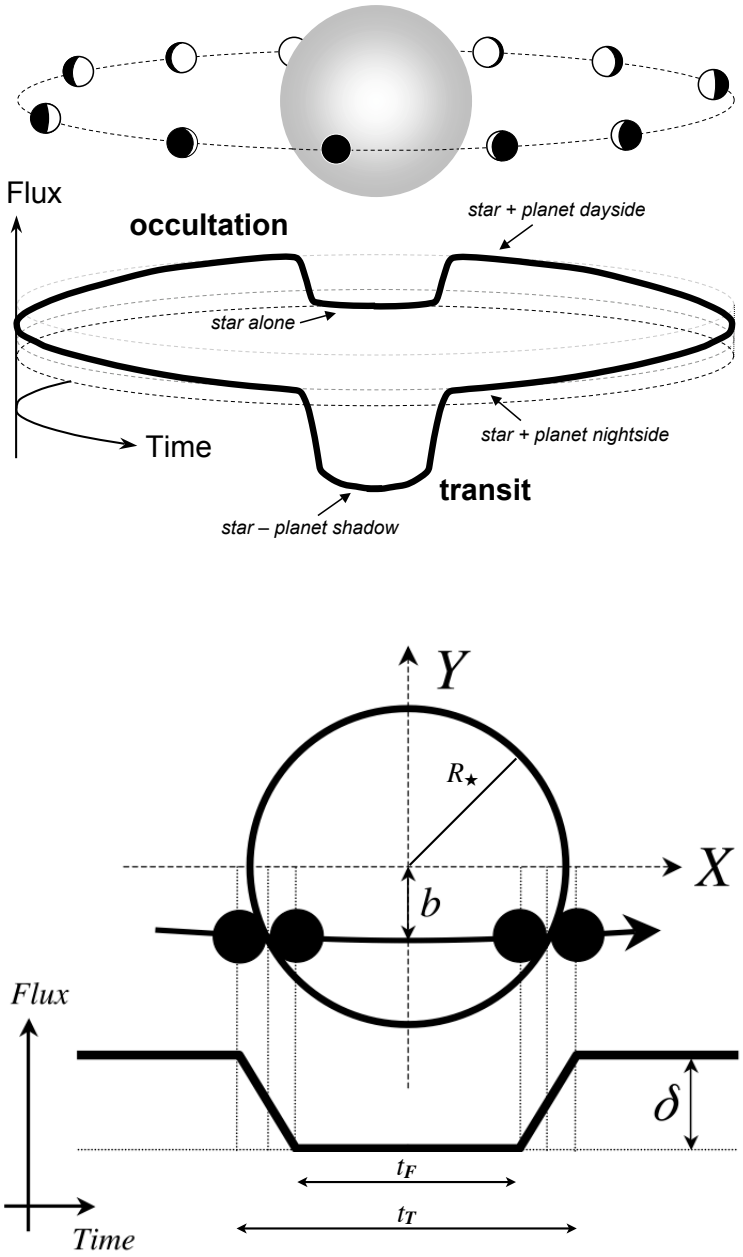

Figure 1.8: Top: Diagram showing the flux variations from a transit (and occultation) around a star. Bottom: Geometry of a transit light curve showing the depth of the transit δ, the radius of the star $R_\star$, the duration of the transit t_T, the impact parameter b and the duration of the transit between ingress and egress t_F. Figure adapted from Winn (2010).

$$\delta = \Delta F = \frac{F_{\text{notransit}} - F_{\text{transit}}}{F_{\text{notransit}}} = \left(\frac{R_p}{R_\star}\right)^2 \tag{1.10}$$

where ΔF, R_p and $R_\star$ denote the change in flux (contrast) measured in the light curve, the radius of the planet, and the radius of the star, respectively.

If the mean flux radiated by the star, measured in the light curve is denoted by F, the typical contrast for a Jupiter-sized planet orbiting around a Sun-like (1 $R_\odot$) star, the contrast would be of order 1% or 0.01 mag.

Ground-based surveys can find planets with typical contrast ratios of $\frac{\Delta F}{F} \sim 1\%$. On the other hand, space-based surveys, in the absence of atmospheric effects, can reach down to $\frac{\Delta F}{F} \sim 10^{-4}$, according to Perryman (2011).

The inclination of the system can be written, based on Figure 1.8 and according to Seager & Mallén-Ornelas (2003)

$$b = \frac{a}{R_\star}\cos \text{i} = \left(\frac{(1-\sqrt{\Delta F})^2[\,\sin^2(t_F\pi/P)/\sin^2(t_T\pi/P)]\,(1+\sqrt{\Delta F})^2}{1-[\,\sin^2(t_F\pi/P)/\sin^2(t_T\pi/P)]}\right)^{\frac{1}{2}} \tag{1.11}$$

and we can write the scale parameter $\frac{a}{R_\star}$, as

$$\frac{a}{R_\star} = \left(\frac{(1+\sqrt{\Delta F})^2 - b^2(1-\sin^2)(t_T\pi/P))}{\sin^2(t_T\pi/P)}\right)^{\frac{1}{2}} \tag{1.12}$$

Combining these relations, as shown by Seager & Mallén-Ornelas (2003) an expression for the stellar density, $\rho_\star$, can be found

$$\rho_\star = \frac{M_\star}{R_\star^3} = \left(\frac{4\pi^2}{P^2 G}\right)\left(\frac{(1+\sqrt{(\Delta F)^2} - b^2(1-\sin^2(t_T\pi/P))}{\sin^2(t_T\pi/P)}\right)^{\frac{3}{2}} \tag{1.13}$$

At this point, it is reasonable to consider that the total transit duration and transit duration between ingress and egress, will be both much smaller than the orbital period of the planet, i.e., $t_T\pi \ll P$ and $t_F\pi \ll P$. Therefore, we can rewrite equations 1.10, and 1.11 and 1.12 into more simpler expressions:

$$b = \left(\frac{(1-\sqrt{\Delta F})^2 - (t_F/t_T)^2(1+\sqrt{\Delta F})^2}{1-(t_F/t_T)^2}\right)^{\frac{1}{2}} \tag{1.14}$$

and finally

$$\frac{a}{R_\star} = \frac{2P}{\pi} \frac{\Delta F^{\frac{1}{4}}}{(t_T^2 - t_F^2)^{\frac{1}{2}}} \tag{1.15}$$

and

$$\rho_\star = \frac{32P}{\pi G} \frac{\Delta F^{\frac{3}{4}}}{(t_T^2 - t_F^2)^{\frac{3}{2}}} \tag{1.16}$$

It is important to note that these relations are valid for circular orbits and neglect the effects of limb-darkening. Limb-darkening is the effect produced by the non-uniform brightness of the stellar disk (Schwarzschild & Villiger 1906) and it can be seen in transit at the times of ingress and egress. Let $I(\cos\theta)$ be the specific intensity of a star, at an angle θ with respect to the normal to the stellar disk, the limb-darkening is commonly parametrized as:

$$I(\mu) = I(1)[\,1 - u_1(1-\mu)] \qquad \text{linear} \tag{1.17}$$

$$I(\mu) = I(1)[\,1 - u_1(1-\mu) - u_2(1-\mu)^2] \qquad \text{quadratic} \tag{1.18}$$

$$I(\mu) = I(1)[\,1 - u_1(1-\mu) - u_2(1-\sqrt{u})] \qquad \text{square-root} \tag{1.19}$$

with $\mu = \cos\theta$, so $I(1)$ corresponds to the intensity at the center of the disk ($\theta = 0$) and u_i are the limb-darkening coefficients. A detailed discussion on the selection of the appropriate limb-darkening law can be found in Espinoza & Jordán (2016). For modeling the transits the parametrization of Kipping (2013) is usually used (see e.g. Espinoza 2018; Espinoza et al. 2019).

1.5 Bayesian Statistics

Bayesian statistics is a powerful framework for probabilistic reasoning and inference, grounded in the principles of conditional probability and Bayes theorem (Gelman et al. 2014). In the Bayesian approach, probabilities are interpreted as degrees of belief, and prior knowledge is combined with observed data to update our beliefs about model parameters or hypotheses. In this context, Bayes theorem plays a central role in the inference process and can be expressed as:

$$P(\boldsymbol{\theta}|\mathcal{D},\mathcal{I}) = \frac{P(\mathcal{D}|\boldsymbol{\theta},\mathcal{I})P(\boldsymbol{\theta}|\mathcal{I})}{P(\mathcal{D}|\mathcal{I})}, \tag{1.20}$$

where $\boldsymbol{\theta}$ represents the vector of model parameters, $\mathcal{D}$ is the observed data, and $\mathcal{I}$ is Prior Information. In this equation, $P(\boldsymbol{\theta}|\mathcal{D},\mathcal{I})$ is the posterior distribution, $P(\mathcal{D}|\boldsymbol{\theta},\mathcal{I})$ is the likelihood, $P(\boldsymbol{\theta}|\mathcal{I})$ is the prior distribution, and $P(\mathcal{D}|\mathcal{I})$ is the marginal likelihood, also known as the Bayesian evidence (hereafter evidence). The evidence serves as a normalization constant, ensuring that the posterior distribution integrates to one:

$$P(\mathcal{D}|\mathcal{I}) = \int P(\mathcal{D}|\boldsymbol{\theta}, \mathcal{I}) P(\boldsymbol{\theta}|\mathcal{I}) \mathrm{d}\boldsymbol{\theta}. \tag{1.21}$$

The process of Bayesian inference typically involves the selection of appropriate prior distributions, the calculation of likelihoods based on the observed data, and the estimation of posterior distributions using numerical techniques, such as Markov Chain Monte Carlo or Nested Sampling algorithms (Gelman et al. 2014; Skilling 2004, 2006).

1.5.1 Bayesian Model Averaging

Bayesian Model Averaging (BMA) is a technique used to account for model uncertainty when making inferences or predictions. Instead of selecting the best model based on some criterion, such as the Bayesian Information Criterion (BIC) or the Akaike Information Criterion (AIC), BMA considers all candidate models and weights their contributions according to their posterior probabilities.

Given a set of candidate models $\mathcal{M}_1, \mathcal{M}_2, \ldots, \mathcal{M}_K$ and corresponding prior probabilities $P(\mathcal{M}_k)$, the model-averaged posterior distribution for a parameter θ can be computed as:

$$P(\theta|\mathcal{D}) = \sum_{k=1}^{K} P(\theta|\mathcal{D}, \mathcal{M}_k) P(\mathcal{M}_k|\mathcal{D}), \tag{1.22}$$

where $P(\theta|\mathcal{D}, \mathcal{M}_k)$ is the posterior distribution of θ under model $\mathcal{M}_k$, and $P(\mathcal{M}_k|\mathcal{D})$ is the posterior probability of model $\mathcal{M}_k$ given the observed data $\mathcal{D}$. The model posterior probabilities can be computed using Bayes' theorem for models:

$$P(\mathcal{M}_k|\mathcal{D}) = \frac{P(\mathcal{D}|\mathcal{M}_k) P(\mathcal{M}_k)}{\sum_{j=1}^{K} P(\mathcal{D}|\mathcal{M}_j) P(\mathcal{M}_j)}, \tag{1.23}$$

where $P(\mathcal{D}|\mathcal{M}_k)$ is the evidence or marginal likelihood for model $\mathcal{M}_k$, and $P(\mathcal{M}_k)$ is the prior probability of model $\mathcal{M}_k$. The evidence can be computed as mentioned earlier, by integrating the product of the likelihood and the prior over the parameter space. This, however, assumes that the parameter θ has the same interpretation or physical meaning across all models being averaged, otherwise, the methodology could be applied to some function of the parameters that take into account the differences in interpretation.

In Bayesian model averaging, several border cases can arise:

1. Dominant Model: If one model has a significantly higher posterior probability than the others, it effectively dominates the model-averaged posterior distribution. In this case, the results of BMA are reduced to selecting the best model and discarding the others.
2. No Dominant Model: When no model is dominant, the posterior probabilities are relatively uniform across the candidate models. In this situation, BMA yields a robust and less biased

estimate of the parameter distributions by incorporating the contributions of all models and properly weighting them by their Evidence.

3. Model Prior Sensitivity: The choice of model priors can have a significant impact on the results of BMA. In cases where the data are not very informative, the model-averaged posterior distribution may be sensitive to the choice of prior probabilities for the models. In these situations, it is essential to perform a sensitivity analysis to assess the robustness of the BMA results with respect to the model priors.

In the case where there is no dominant model, we can compute the averaged posterior distribution of the parameter vector $\bar{\boldsymbol{\theta}}$ as:

$$P(\bar{\boldsymbol{\theta}}) = \sum_{n=1}^{N} P(\boldsymbol{\theta}_n|\mathcal{D}, \mathcal{M}_k)P(\mathcal{M}_n|\mathcal{D}) \tag{1.24}$$

By incorporating the evidence to compute the posterior probabilities of the models, BMA provides a principled approach to dealing with model uncertainty, accounting for the contributions of multiple models in the inference process. By considering all candidate models and their corresponding posterior probabilities, BMA can lead to more robust and reliable parameter estimates and predictions.

1.6 MCMC and Nested Sampling Algorithms

Monte Carlo methods are a class of stochastic computational algorithms that randomly sample a target statistical distribution, commonly a Gaussian, with a given mean function (in the context of exoplanet discovery, this mean function is the Keplerian model given by Equation 1.3). Usually, Monte Carlo methods are combined with Bayesian statistics in order to incorporate external information (hopefully physical in nature) on a given system, solving the problem at hand by providing a set of parameters and uncertainties for the assumed model.

A Markov Chain is a sequence of random variables where the probability distribution of each depends only on the value of the previous one. Formally, a Markov Chain X_n with steps $x^n_{\mathrm{i}=0}$, satisfies the Markov property:

$$P(X_{n+1} = x_{n+1}|X_n = x_n, X_{n-1} = x_{n-1}, \ldots, X_0 = x_0) = P(X_{n+1} = x_{n+1}|X_n = x_n), \tag{1.25}$$

for all $n \geq 0$ and all possible values of $x_0, x_1, \ldots, x_{n+1}$. That is, the $n+1$th step of the Markov Chain only depends on the present state and has no memory of past history.

Markov Chain Monte Carlo (MCMC) methods are a powerful statistical tool that allows us to draw samples from complex, and possibly high-dimensional distributions, that may not have an analytical expression and thus are difficult to sample directly, making parameter inference easier.

The general MCMC algorithm can be summarized as follows:

1. Initialize the Markov chain with an initial state $\boldsymbol{\theta}_0$.
2. Propose a new state $\boldsymbol{\theta}'$ based on the current state $\boldsymbol{\theta}t - 1$.
3. Compute the acceptance probability $\alpha(\boldsymbol{\theta}_{t-1}, \boldsymbol{\theta}')$.
4. Draw a random number $u \sim U(0, 1)$.
5. If $u < \alpha(\boldsymbol{\theta}_{t-1}, \boldsymbol{\theta}')$, set $\boldsymbol{\theta}_t = \boldsymbol{\theta}'$; otherwise, set $\boldsymbol{\theta}_t = \boldsymbol{\theta}_{t-1}$.

After enough samples have been gathered, the Markov Chain approaches the equilibrium distribution, and the samples can then be used to estimate various quantities of interest, such as posterior means or confidence intervals.

1.6.1 Affine-Invariant Sampler

The affine-invariant ensemble MCMC sampler, first introduced by Goodman & Weare (2010), is designed to overcome the limitations of traditional MCMC methods, which can require some customization in order to sample ill-shaped densities. This is achieved through the use of an ensemble of points where the proposal of a new point is generated using the current position of other points in the ensemble.

While this sampler typically has two kinds of steps, we focus our attention on the "stretch move", where one walker is chosen as the "proposer", and another as the "receiver".

Let's denote the current state of the ensemble as $\boldsymbol{\theta}_{\mathrm{i=1}}^{N}$, where N is the number of walkers (points in the ensemble), and $\boldsymbol{\theta}_{\mathrm{i}}$ represents the position of the i-th walker in the parameter space.

In the stretch move, one walker, $\boldsymbol{\theta}_j$, is chosen as the receiver, and another walker, $\boldsymbol{\theta}_k$, is chosen as the proposer, where $k \neq j$. Then, a new position for the receiver is proposed according to:

$$\boldsymbol{\theta}'_j = \boldsymbol{\theta}_k + Z \cdot (\boldsymbol{\theta}_j - \boldsymbol{\theta}_k) \tag{1.26}$$

where Z is a random variable with a specific distribution. Goodman & Weare (2010) suggests a distribution of Z that satisfies detailed balance and is symmetric around 1, namely:

$$p(Z) = \begin{cases} \frac{1}{\sqrt{Z}}, & Z \in \left[\frac{1}{a}, a\right] \\ 0, & \text{otherwise} \end{cases} \tag{1.27}$$

where $a > 1$ is the stretch factor parameter.

This new position $\boldsymbol{\theta}'_j$ is then accepted or rejected according to a standard Metropolis-Hastings criterion:

$$P_{\text{accept}} = \min\left[1, Z^{N-1} \cdot \frac{p(\boldsymbol{\theta}'_j)}{p(\boldsymbol{\theta}_j)}\right] \tag{1.28}$$

where $p(\boldsymbol{\theta})$ is the target probability distribution. If the move is accepted, the walker moves to the new position, $\boldsymbol{\theta}_j = \boldsymbol{\theta}'_j$; otherwise, it stays at its current position. This is repeated for all walkers in the ensemble.

The affine-invariant sampler has been shown to have superior performance in sampling from complex distributions with highly correlated parameters, and in particular, it has been extensively used in the context of exoplanet analysis (see Hou et al. 2012). The affine-invariant sampler forms the basis of several popular MCMC packages, such as the Python library `emcee` (Foreman-Mackey et al. 2013)

1.6.2 Parallel Tempering Markov Chain Monte Carlo

Parallel tempering MCMC (PTMCMC), also known as replica exchange MCMC, is an advanced MCMC technique designed to improve the exploration of multi-modal distributions by simulating multiple chains at different temperatures. The basic idea is to run several Markov chains in parallel at different temperatures and occasionally exchange their states, allowing the chains at higher temperatures to explore the state space more efficiently.

The effect of temperature $T_n = 1/\beta_n$ on the posterior space can be explicitly represented by modifying the posterior density with an inverse temperature β_n:

$$\mathcal{L}_{\beta_n}(x) = \mathcal{L}^{\beta_n}(x)\Pi(x) \tag{1.29}$$

where $\Pi(x)$ is the prior density and $\mathcal{L}$ is the likelihood. This effectively flattens the posterior space with increasing temperature, converging to the prior distribution when $T \rightarrow \inf$.

The PTMCMC algorithm can be summarized as follows:

1. Initialize N chains with initial states $\boldsymbol{\theta}_0^n$, $n = 1, \ldots, N$, at temperatures $T_n = 1/\beta_n$, with β_n being the inverse temperature.
2. Update the state of each chain $\boldsymbol{\theta}_t^n$ using some MCMC update method, such as the affine-invariant sampling described previously, with the modified posterior density $\mathcal{L}_{\beta_n}$.
3. With some probability, propose an exchange of states between adjacent chains with indices n and $n+1$.
4. Compute the acceptance probability for the exchange:

$$\alpha(\boldsymbol{\theta}_t^n, \boldsymbol{\theta}_t^{n+1}) = \min\left[1, \frac{P(\boldsymbol{\theta}_t^n|D)^{\beta n+1} P(\boldsymbol{\theta}_t^{n+1}|D)^{\beta_n}}{P(\boldsymbol{\theta}_t^n|D)^{\beta_n} P(\boldsymbol{\theta}_t^{n+1}|D)^{\beta n+1}}\right]. \tag{1.30}$$

5. Draw a random number $u \sim U(0,1)$.
6. If $u < \alpha(\boldsymbol{\theta}_t^n, \boldsymbol{\theta}_t^{n+1})$, swap the states of the chains.

This method has been shown to work in an agnostic search of exoplanet signals on RVs and LCs (Tuomi et al. 2014; Jenkins et al. 2020b)

1.6.3 Nested Sampling Algorithms

Nested Sampling (NS; Skilling 2004, 2006) is a powerful algorithm used for evidence estimation, which generates parameter distributions as a useful side-product. They are widely used in astrophysics, especially in the area of cosmology due to their ability to efficiently explore high-dimensional parameter spaces and the computation of evidence, which is vital for model comparison. NS is mainly a Monte Carlo-based technique where the central idea is to transform the multi-dimensional integral over the prior space for calculating the evidence into a one-dimensional integral. To achieve this, the prior volume is compressed iteratively, and at each iteration, a sample is drawn from a constrained prior distribution.

The evidence is given by:

$$\mathcal{Z} = \int \mathcal{L}(\boldsymbol{\theta})\pi(\boldsymbol{\theta})\mathrm{d}\boldsymbol{\theta}, \tag{1.31}$$

where $\mathcal{L}(\boldsymbol{\theta})$ is the likelihood function, and $\pi(\boldsymbol{\theta})$ is the prior probability density over the parameter space $\boldsymbol{\theta}$. The evidence is a key quantity for model comparison in a Bayesian framework.

To compute the evidence, NS introduces a new variable, X, representing the prior volume:

$$X(\lambda) = \int_{\mathcal{L}(\boldsymbol{\theta})>\lambda} \pi(\boldsymbol{\theta})\mathrm{d}\boldsymbol{\theta}, \tag{1.32}$$

where λ is the likelihood threshold. The evidence can now be expressed as:

$$\mathcal{Z} = \int_0^1 \mathcal{L}(X)\mathrm{d}X. \tag{1.33}$$

By drawing samples from the constrained prior distribution at each iteration, NS produces a set of points with decreasing prior volumes and increasing likelihood values. These samples can be used to approximate the evidence integral and produce posterior inferences.

The basic NS algorithm can be outlined as follows:

1. Draw N points, called "live points," uniformly from the prior distribution $\pi(\boldsymbol{\theta})$ and calculate their likelihoods $\mathcal{L}(\boldsymbol{\theta}_\mathrm{i})$.
2. Set the initial prior volume $X_0 = 1$ and $\mathrm{i} = 0$.
3. Find the point with the lowest likelihood, $\boldsymbol{\theta}_\mathrm{min}$, and its corresponding likelihood $\mathcal{L}_\mathrm{min}$.
4. Estimate the prior volume $X_{\mathrm{i}+1} = X_\mathrm{i} \exp(-1/N)$.
5. Update the evidence approximation: $\mathcal{Z}_{\mathrm{i}+1} = \mathcal{Z}_\mathrm{i} + \mathcal{L}_\mathrm{min}(X_\mathrm{i} - X_{\mathrm{i}+1})$.
6. Replace $\boldsymbol{\theta}_\mathrm{min}$ (now a "dead point") with a new point drawn from the constrained prior distribution with $\mathcal{L}(\boldsymbol{\theta}) > \mathcal{L}_\mathrm{min}$, and calculate its likelihood.

7. Increment i and go back to step 3. Continue until a stopping criterion is met, usually when the remaining prior volume is negligibly small or the evidence converges.
8. Compute the final evidence estimate $\mathcal{Z} = \sum_{i=1}^{n} \mathcal{L}_i (X_{i-1} - X_i)$, where n is the total number of iterations.

   Subsequently, posteriors can be estimated "for free" from the same n dead points by re-weighting them with their importance weight, given as follows:

$$w_i = \frac{\mathcal{L}_i (X_{i-1} - X_{i+1})}{\mathcal{Z}}, \tag{1.34}$$

   With the weights w_i, we can obtain the marginalized posterior distribution for a single parameter θ_j as:

$$p(\theta_j|\mathcal{D}) \approx \sum_{i=1}^{n} w_i \delta(\theta_j - \theta_{j,i}), \tag{1.35}$$

   where $\mathcal{D}$ is the observed data and $\delta(\cdot)$ is the Dirac delta function. The same procedure can be applied to obtain the posterior distributions for all other parameters in $\boldsymbol{\theta}$.

NS algorithms have seen wide use in some branches of physics and astronomy, yet only recently they have been used within the exoplanet community, thanks to implementations such as `MultiNest` (Feroz et al. 2009; Buchner et al. 2014), `dynesty` (Speagle 2020), `UltraNest` (Buchner 2016, 2019, 2021), and `Nautilus` (Lange 2023) and their availability in exoplanet fitting software (Espinoza et al. 2019; Günther & Daylan 2019, 2021a).

1.7 Stellar Activity

Modeling and mitigating the effects of stellar activity on radial velocities is one of the most important efforts currently being pursued in radial velocity modeling. There have been a significant amount of candidates whose planetary nature has been challenged as being the measurement of different brands of stellar activity. For example, HD 189733 was theorized to have a third body in the system (Boisse et al. 2009), but later it was attributed to the rotation of active regions on the star (Boisse et al. 2011). Other examples of disputed candidates include GJ 581 d (Robertson et al. 2014), which was later suggested to be caused by magnetic cycles of the host star by Anglada-Escudé & Tuomi (2015), HD 166435 (Queloz et al. 2001a), and HD 41248 (Santos et al. 2014) which was later disputed by Jenkins & Tuomi (2014).

1.7.1 Stellar Spots

Low-mass main-sequence stars, such as the Sun, generate magnetic activity that manifests itself as brighter or darker zones on their surface, such as spots or plage regions (unusually bright regions). The light emitted by the star is affected by these zones, which causes variations in the shape of the spectral lines, thus complicating radial velocity measurements (Reiners et al. 2010). Since these active regions are actively rotating in and out of view as the star spins, they can mimic or mask the radial velocity signals of orbiting exoplanets (Dumusque et al. 2011). This effect is especially

difficult to deal with when the stellar rotation period or its harmonics are close to the true radial velocity signal. For example, starspots can lead to an apparent emission in absorption lines, which later manifest as changes in the line asymmetries inducing radial velocity shifts that range from a few m s^{-1} up to 100 m s^{-1} for the most active stars.

1.7.2 Granulation

Studying the surface of the Sun has revealed a characteristic corrugated pattern called granulation. Individual granules are hot bubbles of gas, which in stars with an outer convective envelope, rise to the surface, cool down, and then sink back into the integranular lanes. These movements of plasma induce blue and red shifts accordingly, but since the granules are brighter and bigger than the intergranular lanes, there is a net blueshift in the observed line profiles, especially noticeable in short integration times.

1.7.3 Pressure Modes

Acoustic waves excited by convection in the near-surface layer of cool stars can set up internal standing waves. The resulting pressure modes (p-modes) can be detected by the gentle oscillations they give rise to. In Sun-like stars, these oscillations occur on a timescale of minutes, with an average of 5 minutes for solar-type stars (O'Toole et al. 2008).

1.7.4 Convection

Convection is related to the magnetic field of the star and is responsible for most of the stellar variability (Milbourne et al. 2019), it results in hot, bright granules rising to the surface, cooling, and then falling back, resulting in a net convective blueshift with an associated asymmetric line profile that changes as the granules evolve. In regions with enhanced magnetic activity, magnetic field lines can suppress convection, reduce the net blueshift, and alter the line shapes. These alterations can induce shifts of tens of m s^{-1}. All stars with a convective envelope exhibit radial velocity shifts from p-modes and granulation at the level of tens of cm s^{-1} to a few m s^{-1}.

1.7.5 Modeling Techniques

Now we focus on different mitigation techniques that can be applied to isolate true radial velocity signals. The most basic of techniques is the monitoring of stellar activity indices that are trivially derived from observed spectra, such as H_α and Ca II H&K (Wilson 1978; Saar 1998; Wright et al. 2004; Wright 2005; Jenkins et al. 2008, 2011). Studying their correlation with radial velocities and their periodograms (e.g. the Generalized Lomb Scargle Periodogram; Lomb 1976; Scargle 1982; Zechmeister & Kürster 2009) provide valuable information on the nature of a planet candidate. The CCF method also produces some indicators as a by-product, for example, the Bisector Velocity Span, which is the velocity difference between two bisector points of the CCF (Toner & Gray 1988), from which we compute the Bisector Inverse Slope (BIS; Dall et al. 2006), the FWHM of the Gaussian fit to the CCF, and the CCF contrast, defined as the minimum value reached by the CCF. It has been shown that correlations between the radial velocities and the BIS cast doubts on the planetary interpretation of the radial velocity variation (Queloz et al. 2001a). A more involved method

includes utilizing these activity indicators during radial velocity modeling as linear correlations (Tuomi et al. 2013b; Anglada-Escudé et al. 2016). In addition, Ahrer et al. (2021) studied the effect of more complex stellar activity models in conjunction with radial velocities.

Another method involves modeling correlated noise using classical statistical methods such as autoregression moving average models with an exponential time-decay kernel (ARMA Tuomi et al. 2013a), which in addition to being able to model stellar activity, also handles any systematic correlated noise that might be affecting the instruments. Machine learning algorithms such as Gaussian Processes have also been proposed for modeling correlated noise (e.g. Ambikasaran et al. 2015). Though there are also Gaussian Processes frameworks that implement physically motivated kernels, such as the one proposed by Rajpaul et al. (2015) that allows the joint modeling of radial velocities and activity indicators, or `celerite` (Foreman-Mackey et al. 2017a; Foreman-Mackey 2018) which works as a more general Gaussian Process framework.

Complementary observations are also used to isolate activity signals within radial velocity data. For example, photometric observations can be used to determine the rotation period of the host star, which later can be identified within the radial velocities or activity indicators and subsequently distinguish planetary signals from activity signals, in conjunction with the aforementioned methods (Díaz et al. 2020b; Toledo-Padrón et al. 2021). Finally, stellar activity can be wavelength-depending, allowing the decomposition of the radial velocities in the different wavelength components and studying different color radial velocities. This is known as the chromatic effect and has shown promise in disentangling stellar activity from radial velocities (Cale et al. 2021).

1.8 Thesis Outline

Including this introduction, the thesis is comprised of 5 chapters.

Chapter 2 presents the discovery and orbital characterization of NGTS-6b, an ultra-short period Hot Jupiter orbiting an old K dwarf. The joint analysis of the light curves and radial velocities show a planet orbiting at 21.17 h with a mass and radius of 1.22±0.03 M_J and 1.27±0.19 R_J respectively, adding a new planet to the small list of ultra-short period gas giants.

Chapter 3 describes in detail a new algorithm to derive stellar parameters from archival photometry data in an automatic manner. This method fits several atmospheric model grids to publicly available photometry using empirical priors for the temperature, metallicity and distance, allowing for a constrained posterior distribution for the radius of the star. The inclusion of averaging the different distribution parameters in a Bayesian manner allows for a model-agnostic approach with more robust distributions on key parameters such as the surface temperature and radius of the star.

Chapter 4 presents the confirmation and characterization of a dense mini-Neptune orbiting the bright young star HD 18599. An important discovery considering little is known about the young planet population due to the detection of small planets orbiting these stars is obscured by the effects of stellar activity and rotation, which mimic the Keplerian signature in radial velocity data. Using different stellar activity models and model selection, a planet is found orbiting HD 18599 in 4.138 days, with a mass of 25.5±4.6 $M_\oplus$ and a radius of 2.70±0.05 $R_\oplus$, resulting in a high density of 7±1 g cm^{-3}.

Chapter 5 presents the discovery of a new inflated Hot Jupiter from NGTS. The ~ 4.16 day period planet has an inferred mass and radius of 1.12±0.12M_J and 1.61±0.16R_J respectively, a significant amount inflation when considering an equilibrium temperature of 1410 K. Inflation models predict a radius of $1.13^{+0.14}_{-0.13}R_J$, which is significantly lower than the observed radius. This makes the Hot Jupiter stand out amongst other planets similar in radius and will serve to stress our current knowledge of inflation (and re-inflation) mechanisms.

The conclusions and future work are presented at the end of this thesis.

Chapter 2

NGTS-6b: An Ultra Short Period Hot-Jupiter Orbiting an Old K Dwarf

Based on the results published in Vines, J. I., et al., *NGTS-6b: An Ultra Short Period Hot-Jupiter Orbiting an Old K Dwarf*, 2019, MNRAS, 489, 4125.

In this chapter, we discuss the discovery and orbital characterization of NGTS-6b, an ultra-short period Hot Jupiter from NGTS. With a period of just 21.17 h, NGTS-6b joins the ranks of the ultra-short period giant planets. We found the mass and radius to be 1.33 M_J and 1.27 R_J respectively. Being such an extreme system we studied photoevaporation models and found that over the 9.5 Gyrs of evolution, NGTS-6b should have lost about 5% of its gaseous atmosphere.

2.1 Observations

2.1.1 NGTS Photometry

The NGTS is a ground-based wide-field transit survey located at the ESO Paranal Observatory in Chile, monitoring stars with $I < 16$ (Wheatley et al. 2018). It obtains full-frame images from twelve independent telescopes, each with a field of view of 8 square degrees, at 13 s cadence. The telescopes have apertures of 20 cm and observe at a bandpass of 520-890 nm. They have a total instantaneous field of view of 96 square degrees. A total of 213,549 10s exposures of the field containing NGTS-6 were taken between the nights of 16th of August 2017 and the 23rd of March 2018.

The NGTS data were processed using the NGTS pipeline (Wheatley et al. 2018). Aperture photometry based on the CASUtools (Irwin et al. 2004) software package was used to generate the light curve using an aperture of 3 pixels, with 5 arcseconds per pixel. To remove the most dominant systematic effects the SysRem algorithm (Tamuz et al. 2005) has been utilized. Finally, using ORION, our own implementation of the BLS algorithm (Kovács et al. 2002), a transit signal with a period of 0.882055 d for the star NGTS-6b was discovered. We show the transit in the NGTS phase folded light curve with the corresponding model and confidence region (see Section 2.3.2 for details) in Figure 2.1.

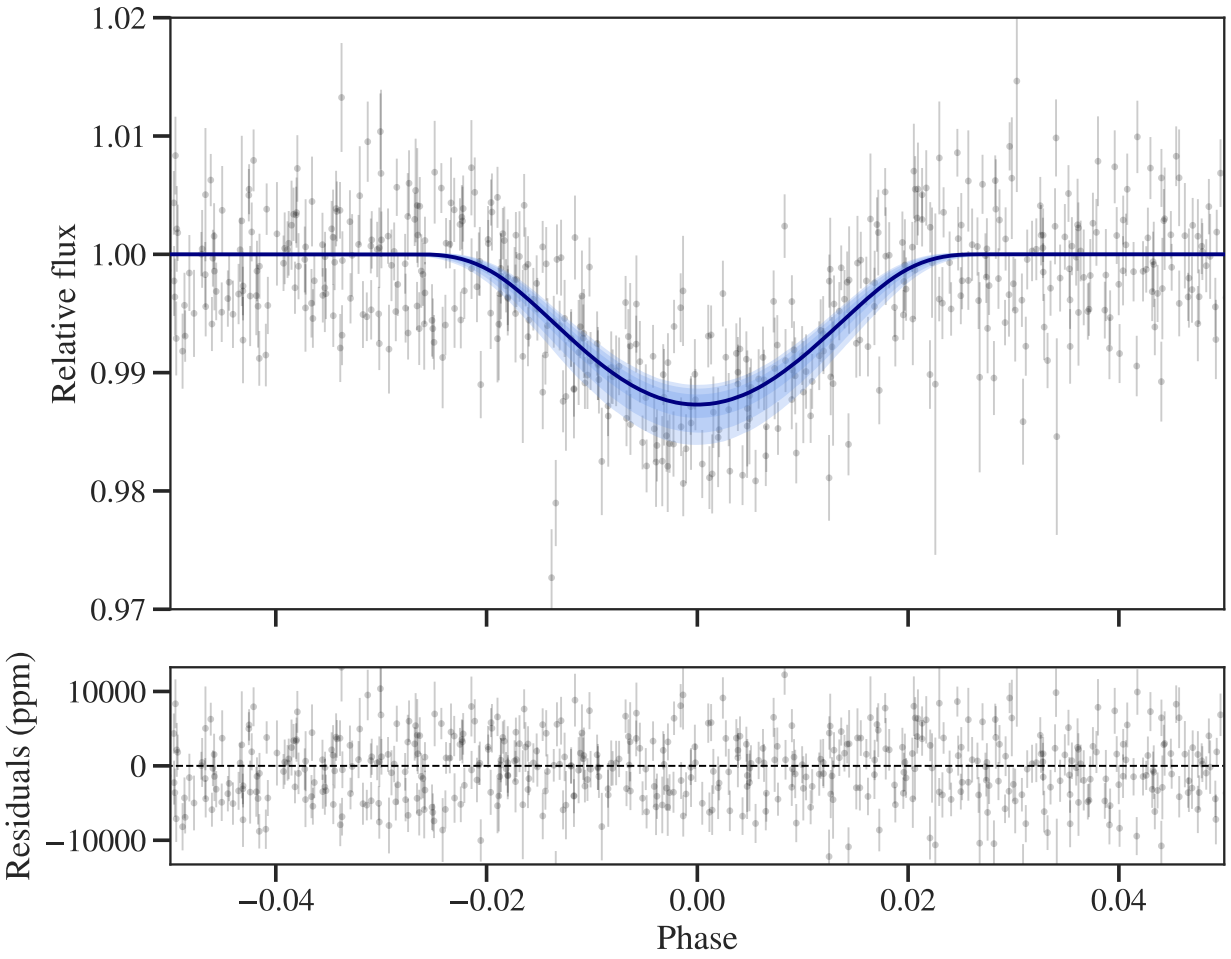

Figure 2.1: Light curve of NGTS photometry for NGTS-6 phase folded to the planets orbital period. The grey circles show the photometry observations binned to 10 minute cadence and the figure is zoomed to highlight the transit. The solid blue line and blue shaded regions represent the median, $1, 2, 3\sigma$ confidence levels, respectively, of the best posterior model. Bottom: The residuals of the fit in ppm.

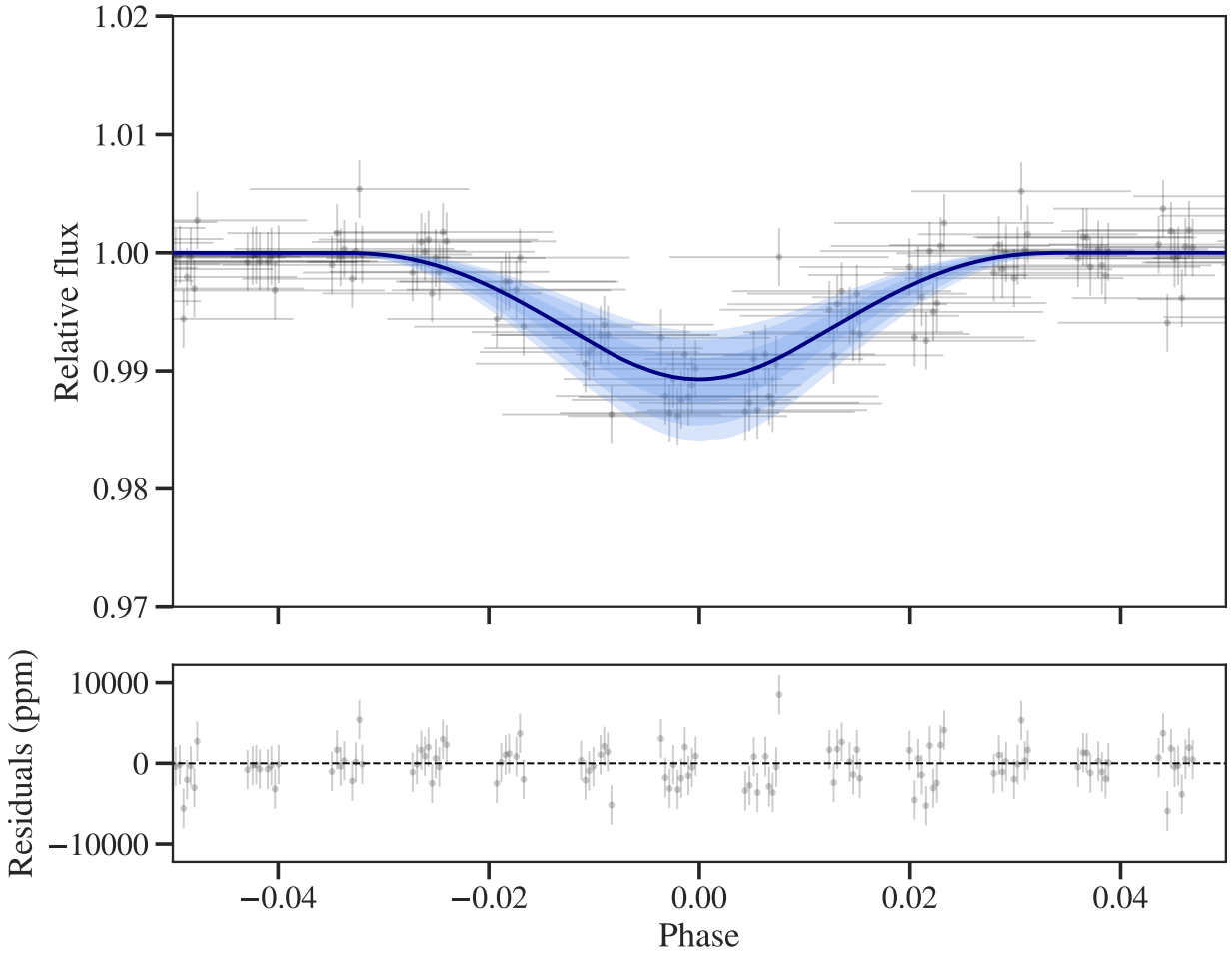

Figure 2.2: Phase folded TESS photometry. Horizontal errorbars show the 30 minute cadence of the observations. The solid blue line is the best fit for the photometry and the blue shaded regions represent the $1, 2, 3\sigma$ confidence levels. Bottom: The residuals of the fit in ppm.

2.1.2 TESS Photometry

The Transiting Exoplanet Survey Satellite (TESS) is a NASA-sponsored Astrophysics Explorer-class mission that is performing a wide-field survey to search for planets transiting bright stars (Ricker et al. 2015). It has four $24 \times 24°$ field of view cameras with four 2k×2k CCDs each, with a pixel scale of 21 arcseconds per pixel and a bandpass of 600-1000 nm. Using the TESSCut tool [1] we checked for available data in the TESS full frame images. NTGS-6b was observed by TESS in Sector 5 using CCD 2 of Camera 2. Between November 15th and December 11th 2018 1196 images with a typical cadence of 30 minutes were obtained. Using a small 2x2 pixel aperture to minimize contamination, we performed aperture photometry on the target. Long term trends visible in the data were removed using a Savitzky-Golay filter. The single transit events are directly visible in the TESS data, although with the long cadence and short transit duration, not well sampled. In Figure 2.2 we show the TESS light curve phase folded to the period obtained from the global modeling.

[1] https://mast.stsci.edu/tesscut

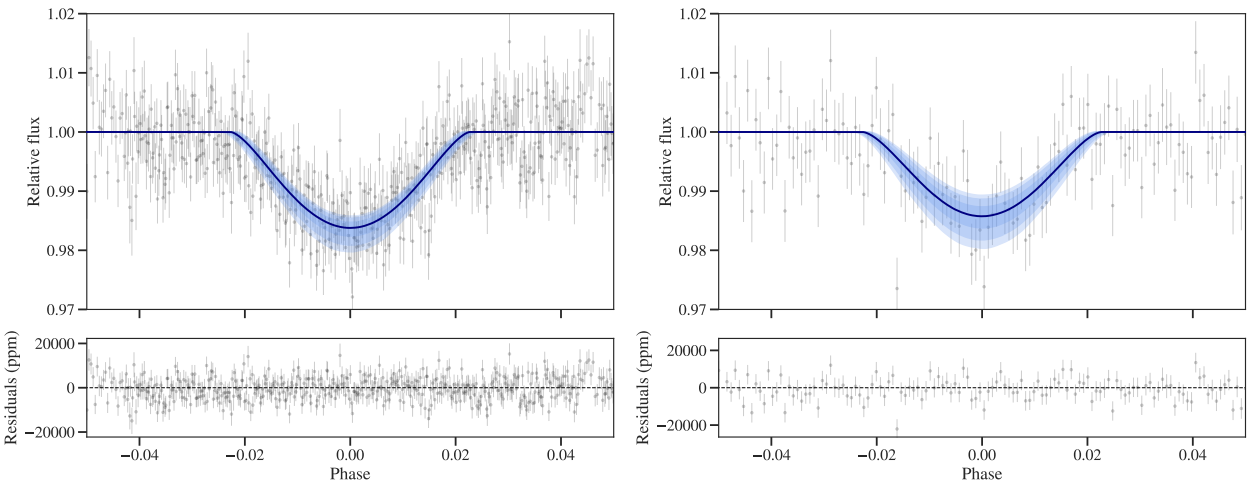

Figure 2.3: Top: Phase folded SAAO photometry in the I and V band respectively for (a) and (b). The solid blue line is the best fit for the photometry and the blue shaded regions represent the $1, 2, 3\sigma$ confidence levels. Bottom: The residuals of the fit in ppm.

2.1.3 SAAO Photometric Follow Up

Three transit light curves were obtained with the 1.0-m Elizabeth telescope at the South African Astronomical Observatory (SAAO) and one of the SHOC frame-transfer CCD cameras, "*SHOC'n'awe*" (Coppejans et al. 2013). The transits were collected on 2018 October 7 in V band (240×60 second exposures), and on 2018 November 14 and 15 in I band (470×30 second and 340×30 s exposures respectively. The scale of each pixel is 0.167 arcsec). The data were reduced with the local SAAO SHOC pipeline, which is driven by PYTHON scripts running IRAF tasks (PYFITS and PYRAF), and incorporating the usual bias and flat-field calibrations. Aperture photometry was performed using the Starlink package AUTOPHOTOM.

Differential photometry was performed on each light curve using 2 reference stars and altering the size of the aperture to reflect the sky conditions (4px for the V band light curve, 5px for the I band light curve on 2018 Nov 14 and 3px for the light curve obtained on the following night when the conditions were considerably better).

We show phase folded light curves of the three SAAO transit events in Figure 2.3 with their respective models and confidence regions. The complete light curve for all instruments is shown in Table 2.1

2.1.4 Spectroscopic Follow Up

We obtained multi-epoch spectroscopy for NGTS-6 with two different fiber-fed high precision échelle spectrographs: CORALIE and FEROS. Both are located at the ESO La Silla Observatory in Chile. CORALIE is mounted on the 1.2-m Leonard Euler telescope and has a spectral resolution of R = 60,000 (Queloz et al. 2001b). FEROS is mounted on the 2.2-m MPG/ESO telescope with a spectral resolution of $R = 48,000$ (Kaufer et al. 1999). The spectral observations were taken between October 23 2018 and January 8 2019 for CORALIE and December 23 2018 and January 2 2019 for FEROS.

The CORALIE data were reduced using the standard data reduction pipeline (Queloz et al. 2001b) and the radial velocities were calculated by cross-correlation with a binary G2 mask. The first 20 orders of the spectrum were discarded in the cross-correlation analysis as they contain little signal. All the CORALIE

Table 2.1: Photometry of NGTS, SAAO I, V and TESS for NGTS-6. The full table is available in a machine-readable format from the online journal. A portion is shown here for guidance.

BJD (-2,450,000)	Relative Flux	Relative Flux error	INST
...	...	...	...
8200.55123	1.0222	0.0169	NGTS
8200.55138	0.9660	0.0168	NGTS
8200.55153	0.9859	0.0169	NGTS
8200.55168	1.0206	0.0171	NGTS
8200.55183	0.9861	0.0169	NGTS
8399.47400	1.0049	0.0044	SAAOV
8399.47469	1.0077	0.0044	SAAOV
8399.47539	0.9974	0.0044	SAAOV
8399.47608	0.9982	0.0044	SAAOV
8399.47678	1.0014	0.0043	SAAOV
...	...	...	...

spectra were also stacked to make a high signal-to-noise spectrum for spectral analysis as presented in Sect. 2.2

FEROS data were reduced with the CERES pipeline (Brahm et al. 2017). CERES also calculates the cross-correlation function (CCF) using the reduced FEROS spectra and a binary G2 mask for each epoch and afterwards, depending on moonlight contamination, a single or double Gaussian is then fitted to find the radial velocity (depending on moonlight contamination). In the cases where the single or double Gaussian fits were unsatisfactory, a 4th order spline was fitted to find the radial velocity instead. The radial velocities from CORALIE and FEROS are shown in Table 2.2 along with the uncertainties and bisector velocity span. We present a total of 21 radial velocity data points, which constrain the orbit of the planet, 11 of which were taken with CORALIE and 10 with FEROS.

As a first check we searched for a correlation between the radial-velocity data and the bisector velocity span, which was calculated using the CCFs that were constructed to measure the velocity in the first place (see for example Boisse et al. 2009). Any correlation between radial-velocity measurements and the bisector velocity span would cast doubts on the validity of the planet interpretation of the radial-velocity variation (Queloz et al. 2001a). The bisector and radial-velocities are shown in Figure 2.4 along with a linear fit and a 2σ confidence region, with no correlation detected. We calculated the Pearson r coefficient to be 0.05, which reaffirms our claim of no significant linear correlation being present.

2.2 Stellar Parameters

Given the host star is relatively faint (V = 14.087), the high-resolution echelle spectra used for the calculation of the radial velocity measurements have SNR too low for the accurate measurement of the equivalent of individual absorption lines, therefore it is not possible to obtain a constrained solution from the SPECIES code (Soto & Jenkins 2018) for the stellar bulk parameters. Therefore, we used two methods: the empirical SpecMatch tool (Yee et al. 2017) with the combined CORALIE spectra, which given the observing conditions have a higher SNR than the FEROS spectra, and an SED fit of the star detailed in Sect. 2.2.1. The output of the two employed methods are shown in Table 2.3

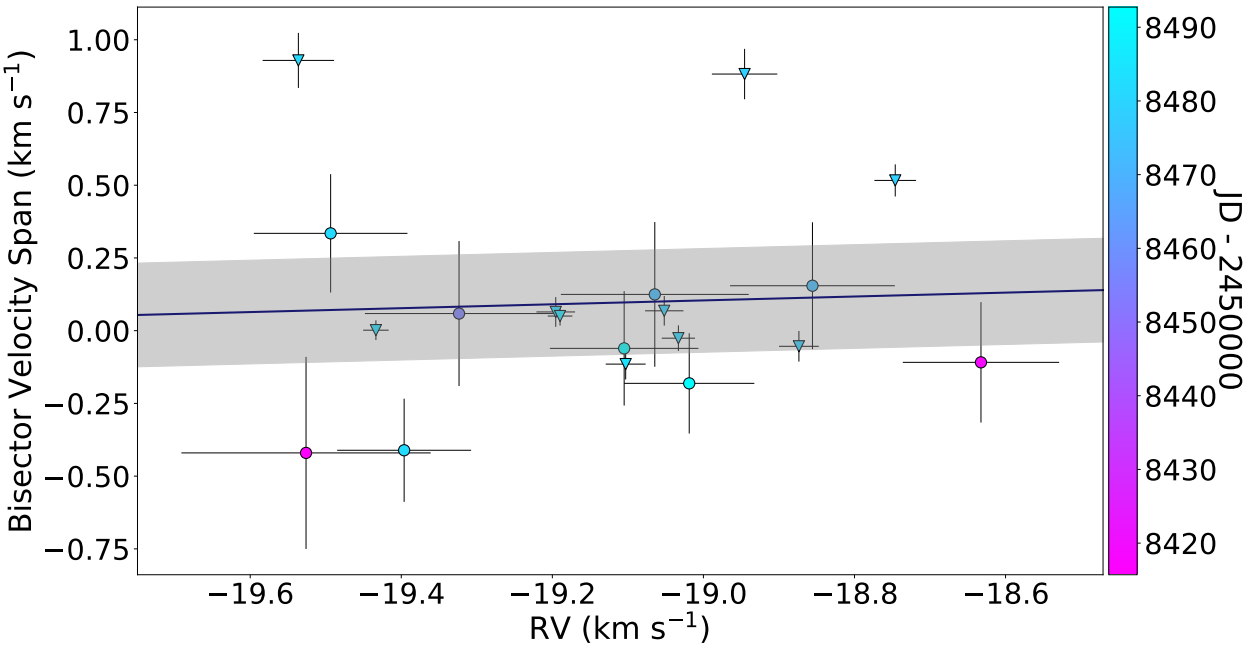

Figure 2.4: Bisector velocity span over radial velocity measurements color coded by observation time. Circles are CORALIE and upside-down triangles are FEROS datapoints. The blue solid line is a linear fit and the shaded region show the 2σ confidence region. No correlation is detected.

Table 2.2: CORALIE and FEROS Radial Velocities for NGTS-6

BJD (-2,450,000)	RV (km s^{-1})	σ_{RV} (km s^{-1})	BIS (km s^{-1})	INST
8415.71	-19.526	0.165	-0.420	CORALIE
8418.74	-18.633	0.104	-0.109	CORALIE
8454.65	-19.324	0.125	0.059	CORALIE
8472.59	-18.856	0.109	0.154	CORALIE
8472.75	-19.064	0.124	0.125	CORALIE
8475.69	-19.333	0.102	——	CORALIE
8475.79	-19.264	0.110	——	CORALIE
8481.71	-19.396	0.089	-0.411	CORALIE
8481.81	-19.494	0.102	0.335	CORALIE
8492.69	-19.019	0.086	-0.181	CORALIE
8492.73	-19.105	0.098	-0.061	CORALIE
8481.85	-19.536	0.047	0.929	FEROS
8480.75	-19.196	0.026	0.064	FEROS
8480.73	-19.033	0.022	-0.026	FEROS
8484.71	-19.189	0.016	0.050	FEROS
8478.79	-18.746	0.028	0.517	FEROS
8478.60	-19.052	0.025	0.068	FEROS
8478.81	-18.946	0.043	0.882	FEROS
8478.62	-18.874	0.026	-0.054	FEROS
8483.84	-19.103	0.026	-0.115	FEROS
8483.67	-19.434	0.017	0.002	FEROS

Table 2.3: Comparison of empirical SpecMatch and SED fitting outputs

Parameter	SpecMatch	SED
$T_{\rm eff}$ (K)	4409 ± 70	4730^{+44}_{-40}
log g	4.63 ± 0.12	$4.7^{+1.1}_{-0.7}$
R_s ($R_\odot$)	0.72 ± 0.1	0.754 ± 0.013
$[Fe/H]$	0.11 ± 0.09	—-
(†) M_s ($M_\odot$)	0.72 ± 0.08	0.767 ± 0.025
(†) Age (Gyr)	9.61 ± 0.17	$9.77^{+0.25}_{-0.54}$
distance (pc)	—-	308 ± 2
A_V	—-	0.017 ± 0.010

In the case of SED fitting, the parameters with (†) were calculated using the isochrones package.

We finally adopt the results from the SED fitting routine for $T_{\rm eff}$, log g, and R_s, and the metallicity from the SpecMatch tool. We used these parameters to calculate the mass and age of the star, using the isochrones package (Morton 2015). The projected rotational velocity, vsini, was estimated using the SPECIES code. We combined the individual spectra obtained with Coralie to obtain a high S/N spectrum from the target, and created synthetic absorption line profiles for four iron lines in the spectrum, using the ATLAS9 model atmospheres (Castelli & Kurucz 2003) and the atmospheric parameters previously obtained. We then broaden the absorption lines, by adjusting the rotational velocity, until they matched the observations. More details about this procedure can be found in Soto & Jenkins (2018). The obtained vsini is listed in Table 2.4. Thus we conclude that NGTS-6 is an old K dwarf with an effective temperature of 4730^{+44}_{-40} K, log g of $4.7^{+1.1}_{-0.7}$ dex, [Fe/H] of 0.11 ± 0.09 dex, radius of 0.754 ± 0.013 $R_\odot$, mass of 0.767 ± 0.025 $M_\odot$ and age of $9.77^{+0.25}_{-0.54}$ Gyrs. We show NGTS-6 catalogue information and stellar parameters in Table 2.4.

2.2.1 SED Fitting and Dilution

Using *Gaia* DR2 we identified a neighbouring source 5.4″ away that could be contaminating our photometry. Therefore, in order to determine the level of dilution from this source we performed SED fitting of both stars using the PHOENIX v2 models (Husser et al. 2013). This was done following a method similar to Gillen et al. (2017), by firstly generating a grid of bandpass fluxes in $T_{\rm eff}$ and log g space. To overcome the issue of possible blending in catalogue photometry (due to the small separation of the two sources) we fit only to the Pan-STARRS, 2MASS, *Gaia* and WISE photometry for each source. We fit for the $T_{\rm eff}$, log g, radius, distance, V band extinction A_V and an uncertainty term σ to account for underestimated catalogue uncertainties. We have used a Gaussian prior on the distance, constrained by the values calculated by Bailer-Jones et al. (2018) using *Gaia* DR2 data. We limit the V band extinction of each source to a maximum value of 0.032, taken from the Galactic dust reddening maps of Schlafly & Finkbeiner (2011). Before fitting we verified that neither source was flagged as extended in the catalogues used. Due to the larger size of the *TESS* aperture, an extra source 15.9″ was identified as possibly contributing light. Consequently, we also performed SED fitting on this source and included it for the *TESS* dilution value only. To sample the posterior parameter space for each source we used *emcee* (Foreman-Mackey et al. 2013) to create a Markov Chain Monte Carlo (MCMC) process for our fitting. In this process we used 100 walkers for 50,000 steps and discarded the first 10,000 as a burn in. The best fitting SED model for NGTS-6 is shown in Figure 2.5 and the values are given in Tab. 2.4.

To estimate the level of dilution in each bandpass we convolved the SED model for each star with the

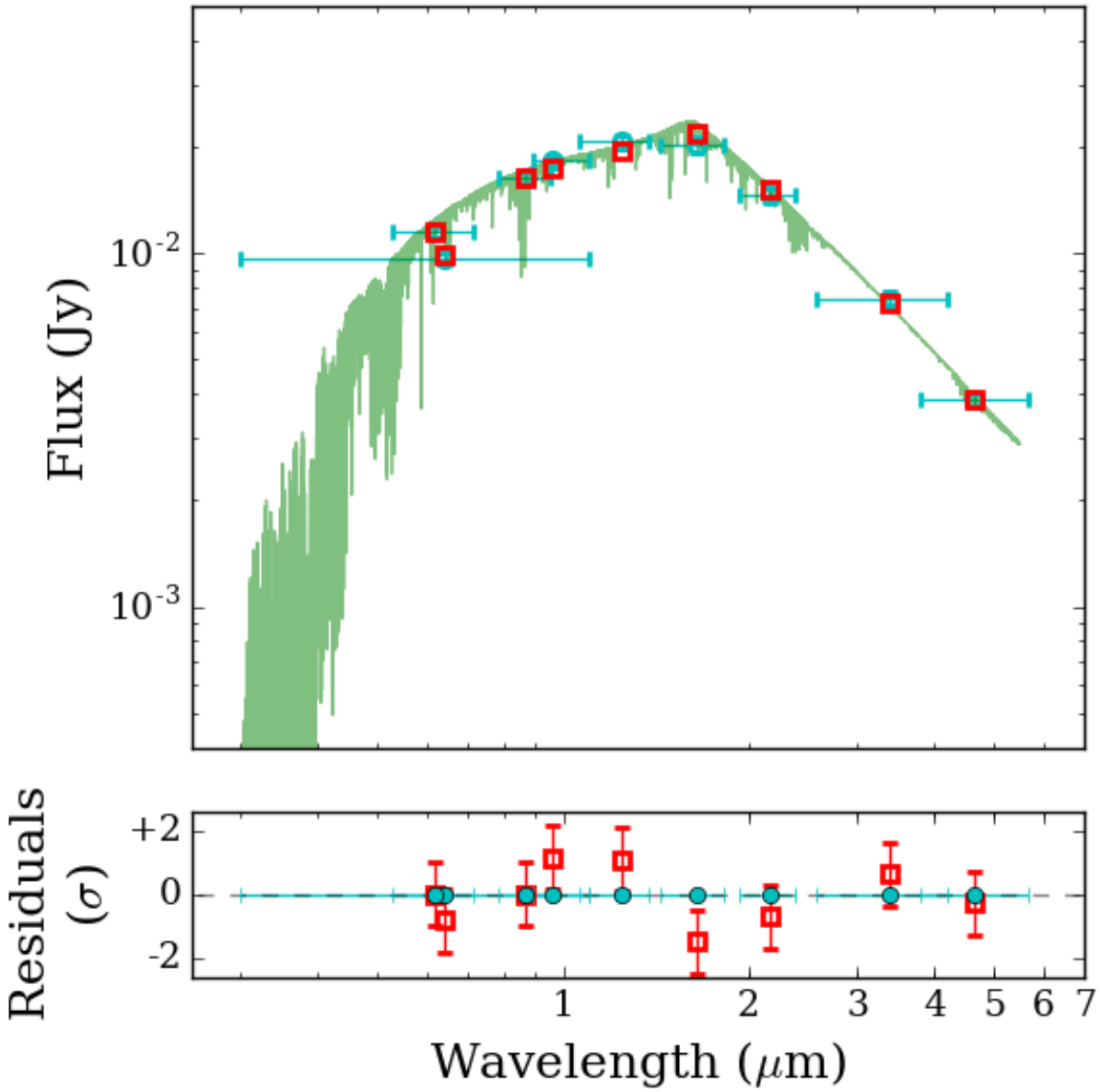

Figure 2.5: Top: The best fitting PHOENIX v2 SED model, obtained from fitting to unblended Pan-STARRS, *Gaia*, 2MASS and WISE photometry. The cyan and red points indicate the catalogue and synthetic photometry respectively. The horizontal error bars indicate the spectral coverage of each band. Bottom: Residuals of the synthetic photometry, normalised to the catalogue errors.

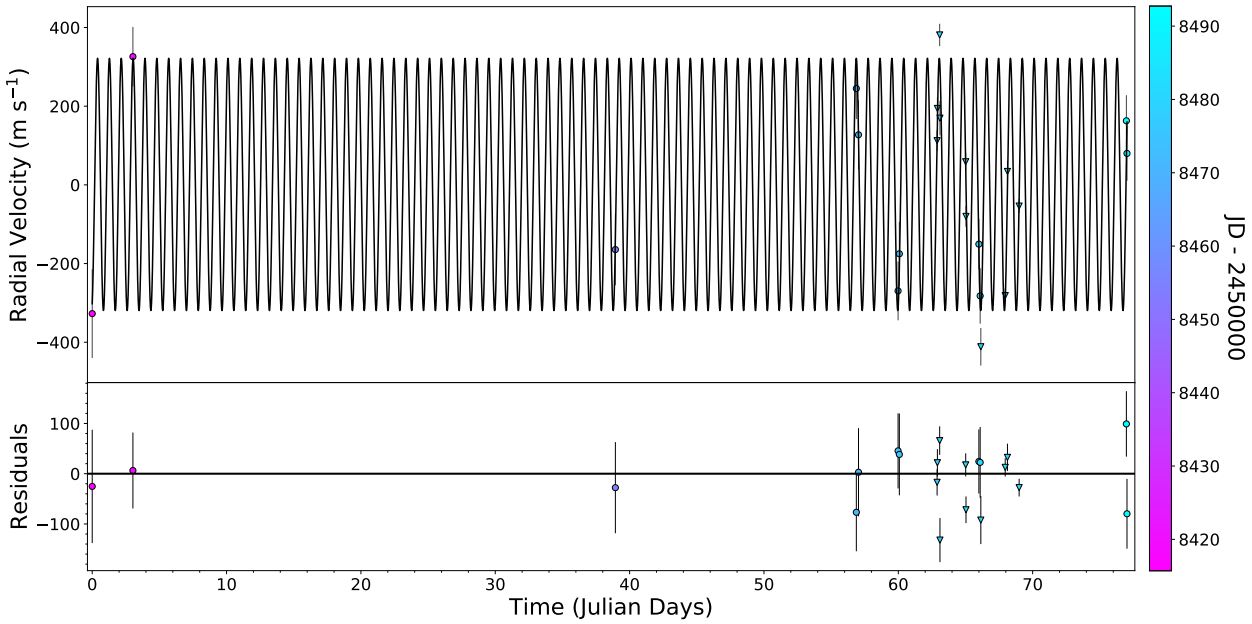

Figure 2.6: Top: The full timeseries of NGTS-6 radial velocity observations, color coded by observation time. Circles are CORALIE datapoints and upside-down triangles are FEROS. The solid black line is the best Keplerian fit. Bottom: The residuals of the fit.

specified filter, taking the ratio of the measured synthetic fluxes as the dilution value. In order to sample the full range of dilutions and thus provide an informative prior we draw our SED models directly from the posterior distribution for each star The calculated dilutions are $D_{NGTS} = 0.056 \pm 0.002$, $D_{SAAOV} = 0.025 \pm 0.002$, $D_{SAAOI} = 0.085 \pm 0.003$ and $D_{TESS} = 0.077 \pm 0.003$. With these results we generate priors for the dilution in our lightcurves, which are used in the transit fitting.

2.3 Data Modeling

2.3.1 Pure Radial Velocity Modelling

Firstly, a pure radial velocity search and model fit was made using the EMPEROR algorithm (Peña Rojas & Jenkins 2018). EMPEROR is a public, python-based code that is designed to search for small signals in radial-velocity data using Bayesian modeling techniques and MCMC tools. The algorithm allows for correlated noise models to be incorporated into the modeling, in particular moving averages of order selected by the user. The code uses the affine-invariant *emcee* sampler in parallel tempering mode to efficiently sample highly multi-modal posteriors.

In order to first test if the signal was present in the data without the use of inputs from the photometry, as a test of signal independence, we employed six chains with different temperature values (β = 1.0, 0.66, 0.44, 0.29, 0.19 and 0.13). The chain length was set to 15,000 steps and each chain had 150 walkers in the ensemble, giving rise to a total chain length of 13.5 million steps. A burn-in of 7,500 steps was also used. A first-order moving average correlated noise model was used to model the high-frequency noise in the velocity data set, and the priors were set to be the standard priors as explained in the EMPEROR manuscript and on the GitHub page[2]. In automatic mode, EMPEROR detects the planet's

[2]https://github.com/ReddTea/astroEMPEROR

Table 2.4: Stellar Properties for NGTS-6

Property	Value	Source
R.A.	$05^h03^m10^s90$	2MASS
Dec	$-30°23'57''.6420$	2MASS
2MASS I.D.	05031090-3023576	2MASS
Gaia DR2 I.D.	4875693023844840448	*Gaia*
TIC ID	1528696	TESS
$\mu_{\rm R.A.}$ (mas y^{-1})	-6.0 ± 7.0	UCAC4
$\mu_{\rm Dec.}$ (mas y^{-1})	-33.5 ± 10.1	UCAC4
ϖ (mas)	3.215 ± 0.015	*Gaia*
V (mag)	14.087 ± 0.021	APASS
B (mag)	15.171 ± 0.014	APASS
g (mag)	14.639 ± 0.058	APASS
r (mag)	13.703 ± 0.032	APASS
i (mag)	13.378 ± 0.057	APASS
r_{P1} (mag)	13.751 ± 0.002	Pan-STARRS
z_{P1} (mag)	13.364 ± 0.002	Pan-STARRS
y_{P1} (mag)	13.250 ± 0.006	Pan-STARRS
G (mag)	13.818 ± 0.001	*Gaia*
BP (mag)	14.401 ± 0.003	*Gaia*
RP (mag)	13.113 ± 0.002	*Gaia*
NGTS (mag)	13.460	This work
TESS (mag)	13.070	TESS
J (mag)	12.222 ± 0.033	2MASS
H (mag)	11.767 ± 0.038	2MASS
K (mag)	11.650 ± 0.032	2MASS
W1 (mag)	11.609 ± 0.028	WISE
W2 (mag)	11.688 ± 0.029	WISE
$T_{\rm eff}$ (K)	4730^{+44}_{-40}	SED fitting
log g	$4.7^{+1.1}_{-0.7}$	SED fitting
$[Fe/H]$	0.11 ± 0.09	CORALIE spectra
vsini (km s^{-1})	2.851 ± 0.431	CORALIE spectra
$\gamma_{CORALIE}$ (km s^{-1})	$-19.137^{+0.018}_{-0.018}$	Global Modelling
γ_{FEROS} (km s^{-1})	-19.142 ± 0.010	Global Modelling
$\sigma_{CORALIE}$ (km s^{-1})	$0.000^{+0.039}_{-0.041}$	Global Modelling
σ_{FEROS} (km s^{-1})	$0.036^{+0.023}_{-0.094}$	Global Modelling
$L_s(L_\odot)$	0.256 ± 0.009	SED fitting
$M_s(M_\odot)$	0.767 ± 0.025	SED fitting
$R_s(R_\odot)$	0.754 ± 0.013	SED fitting
ρ (g cm^{-3})	$3.9304^{+0.0815}_{-0.0812}$	Global Modeling
Age	$9.77^{+0.25}_{-0.54}$	SED fitting
Distance (pc)	311.042 ± 1.432	*Gaia*

2MASS (Skrutskie et al. 2006); UCAC4 (Zacharias et al. 2013);
APASS (Henden & Munari 2014); WISE (Wright et al. 2010);
Gaia (Gaia Collaboration et al. 2016, 2018); TESS (Stassun et al. 2018)
Pan-STARRS (Tonry et al. 2012; Chambers et al. 2016a)

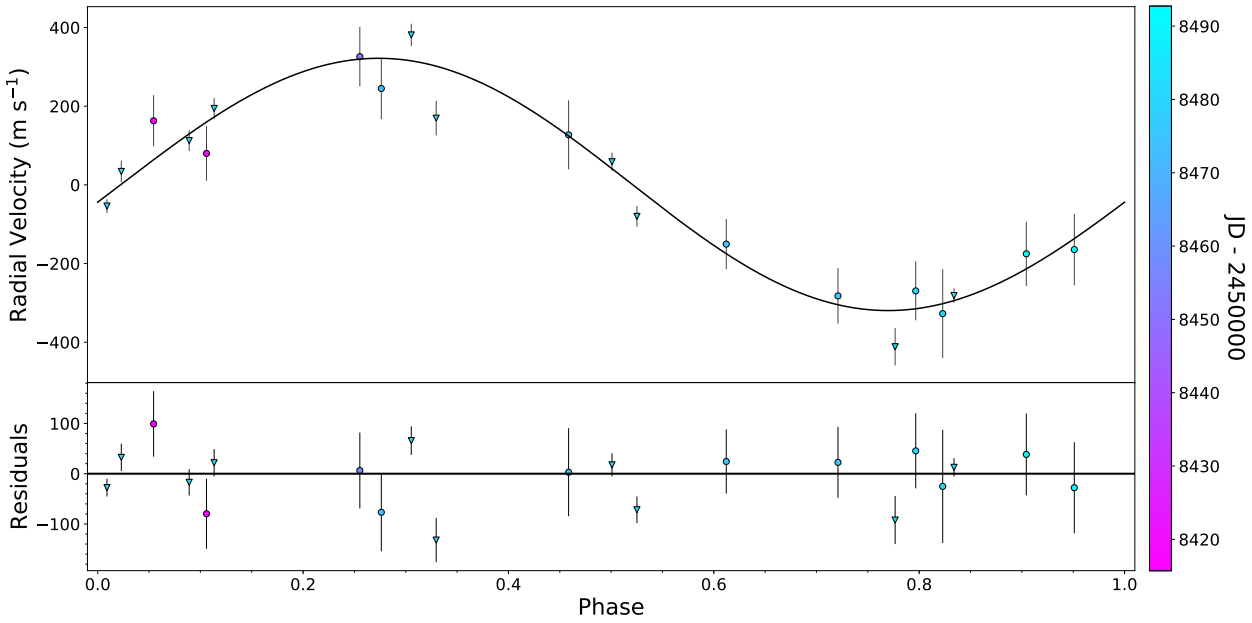

Figure 2.7: Top: NGTS-6 radial velocity measurements and model in orbital phase, color coded by obervation times. Circles are CORALIE datapoints and upside-down triangles are FEROS. The solid black line is the fit to best orbital solution. Bottom: Residuals of the fit.

orbital signature with a Bayes Factor value of 5, highly significant, in the combined FEROS+CORALIE data, confirming the existence of the planet. The best fit made by EMPEROR is shown in Figure 2.6 and the phase folded curve in Figure 2.7. No additional signal was detected. The best fitting model from EMPEROR with respective uncertainties were used as Gaussian priors to determine a global model for this system.

2.3.2 Global Modeling

For the global joint photometry and radial velocity modeling we used Juliet (Espinoza et al. 2019). Juliet is a python tool capable of analysis of transits, radial velocities, or both. It allows the analysis of multiple photometry and radial velocity instruments at the same time using Nested Sampling, Importance Nested Sampling, and Dynamic Nested Sampling algorithms. For the transit models, Juliet uses BATMAN (Kreidberg 2015), which has flexible options, in particular for limb-darkening laws. The Keplerian signal model is provided by radvel (Fulton et al. 2018). Finally for our Juliet run, given the high dimensionality of the model (29 free parameters between two radial velocity and four photometry instruments) we used Dynesty for Dynamic Nested Sampling as it has proven to be more efficient than regular Nested Sampling under these conditions.

The radial-velocity fit made by EMPEROR shows a low eccentricity orbit ($e < 0.01$) thus for the Juliet modeling we decided to fix the eccentricity to 0. Since we have 213, 549 NGTS photometry datapoints plus SAAO photometry in the V and I bands and TESS photometry, fitting such a large light curve is resource intensive, so we first binned the NGTS data in 10 minute cadence bins and then performed the fit with the binned data, supersampling the model light curve to 10 minute exposure times with 30 points in each bin. We also employed supersampling for the 30 minute TESS observations. For the limb darkening we assumed a quadratic law for each instrument. Using Juliet's and the SED fitting output and assuming a Jupiter's Bond albedo of 0.503 (Li et al. 2018) we calculated the equilibrium temperature of NGTS-6b to be $1283.90^{+12.49}_{-12.14}$ K. The parameters for the best fit are presented in Table 2.5 and in Figure 2.8 we show a corner plot with the main planetary parameters.

Table 2.5: Planetary Properties for NGTS-6b

Property	Value
P (days)	0.882059 ± 0.0000008
T_C (BJD - 2450000)	7982.3784 ± 0.0003
a/R_*	$4.784^{+0.043}_{-0.048}$
b	$0.976^{+0.015}_{-0.020}$
K ($km\,s^{-1}$)	0.322 ± 0.008
e	0.0 *(fixed)*
$M_p(M_J)$	1.339 ± 0.028
$R_p(R_J)$	$1.326^{+0.097}_{-0.112}$
ρ_p ($g\,cm^{-3}$)	$0.711^{+0.214}_{-0.136}$
a (AU)	0.01677 ± 0.00032
inc (deg)	$78.231^{+0.262}_{-0.210}$
T_{eq} (K)	$1283.90^{+12.49}_{-12.14}$

The light curves showcased in Section 2.1.3 show a clear V shape transit, suggesting the system is in fact, grazing since non-grazing transiting systems present U-shaped transits. This happens because the planetary disc is not fully encompassed in the stellar disk. This introduces a strong degeneracy between the planet-to-star radius ratio and impact parameter. As b increases, the transit duration and depth decrease (the latter due to stellar limb darkening), and since the transit depth is directly related to the planet-to-star ratio, modeling can produce extreme results (such as an extremely inflated planet). In order to address this issue, a prior for the stellar density constructed from the results of the SED fitting routine was used within Juliet, which allowed us to better decorrelate those two parameters and thus get more realistic results for the parameters of the planet.

2.4 Discussion and Conclusion

We report the discovery of NGTS-6b, a grazing transit ultra-short period hot Jupiter (USP HJ) with a period of 21.17 hours, mass of $1.330^{+0.024}_{-0.028} M_J$ and radius of $1.271^{+0.197}_{-0.188} R_J$, and the first USP HJ from the NGTS. We analyzed the joint photometry and radial velocity data using Juliet, testing its modeling abilities when given a likely grazing transit. There are only a handful of USP planets in the literature, of which only six are giant planets with $R_p > 8\,R_\oplus$(WASP-18b, WASP-43b, WASP-103b, HATS-18b, KELT-16b, and WASP-19b) and therefore our discovery of NGTS-6b represents a significant addition to this extreme population. In Figures 2.9, 2.10, 2.11 we show that NGTS-6b sits at the centre of the distinct clump of UHJs, and thus adds weight to this being a distinct population.

We investigated photoevaporation of the planet, applying empirical relations from Jackson et al. (2012), linking the ratio of the X-ray and bolometric luminosities, L_X/L_{bol}, with stellar age. Using the isochrones-derived age of 9.77 Gyr yields an estimate of $L_X/L_{bol} = 1.0 \times 10^{-5}$ at the current epoch. This corresponds to an X-ray luminosity $L_X = 6 \times 10^{27}\,erg\,s^{-1}$, or a flux at Earth of $5 \times 10^{-16}\,erg\,s^{-1}\,cm^{-2}$. Such a flux would require a very deep observation with current generation X-ray telescopes in order to detect the star. Using the energy-limited method of estimating atmospheric mass loss (Watson et al. 1981; Erkaev et al. 2007), our estimate of L_X yields a mass loss rate of $1 \times 10^{11}\,g\,s^{-1}$. By integrating the mass loss rate across the lifetime of the star (following the X-ray evolution described by Jackson et al. 2012) we estimate a total mass loss of

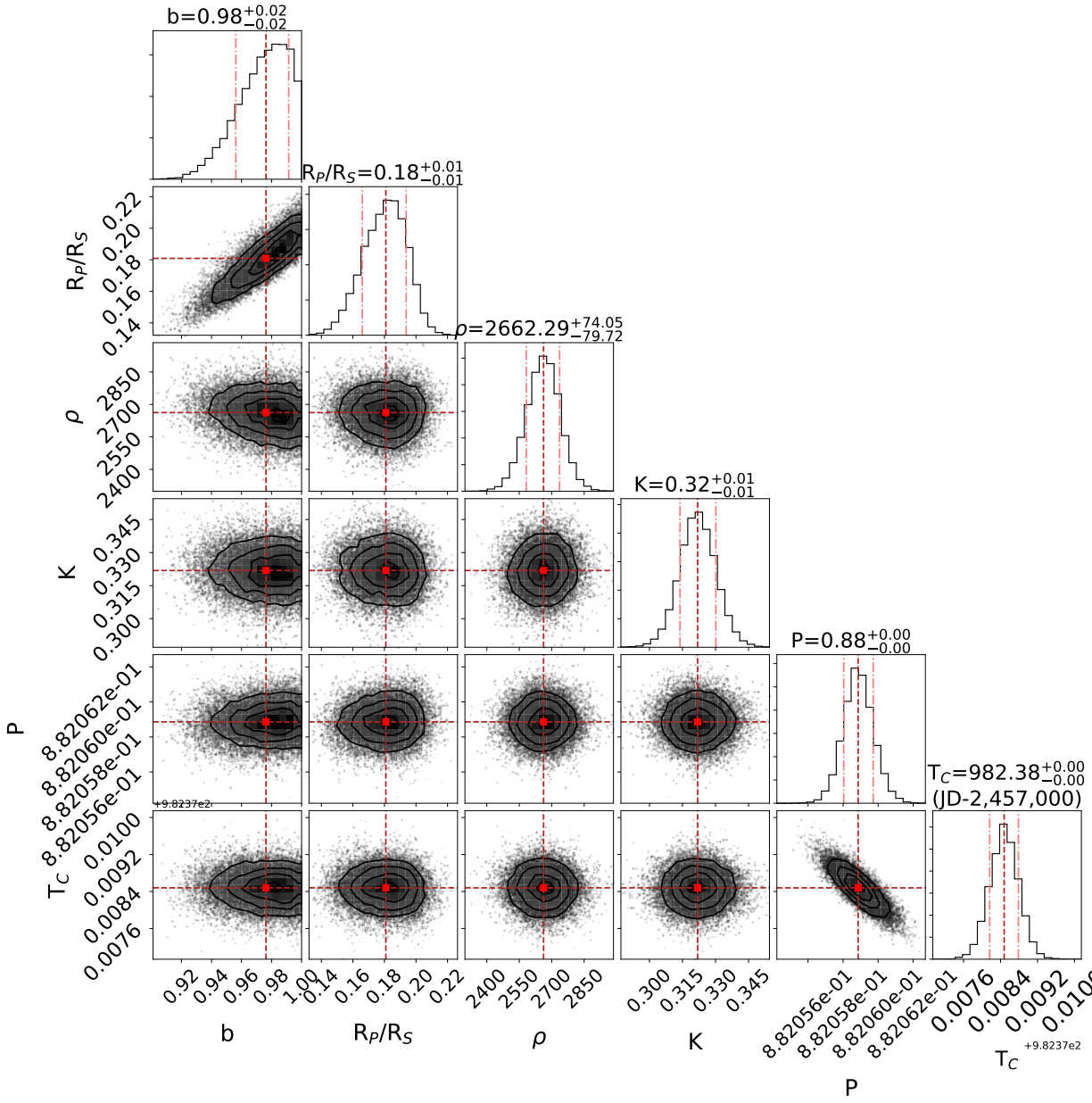

Figure 2.8: Juliet posterior distributions for the main planetary parameters. The red dashed lines are the median of each distribution and the dash-dot lines represent the 1σ confidence interval. A correlation between the impact parameter and the planet to star radius is expected due to the grazing nature of the system.

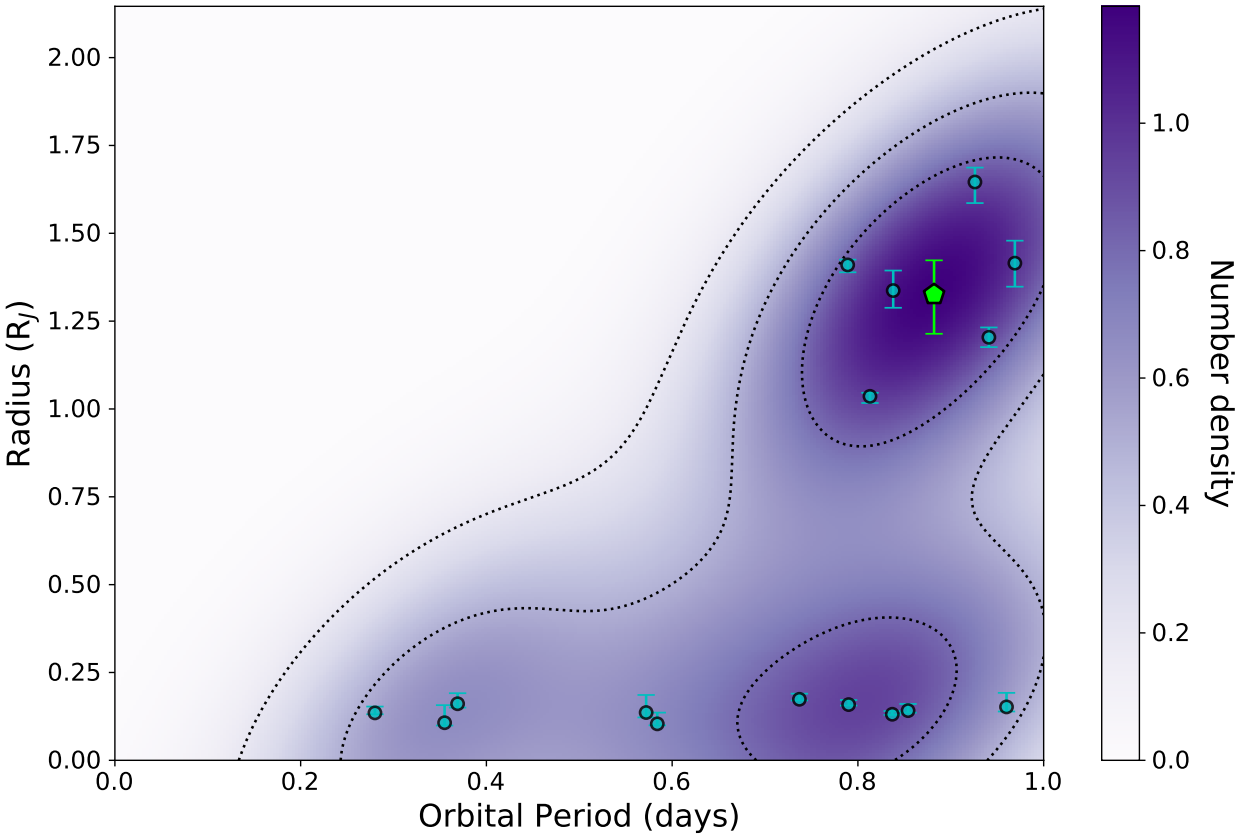

Figure 2.9: Planetary radius against orbital period. Plotted are all USP planets and UHJs from the well-studied transiting planets catalog that have both measured mass and radius. The dark contours and purple shading highlight the planet number density of the sample. The green pentagon shows the position of NGTS-6b

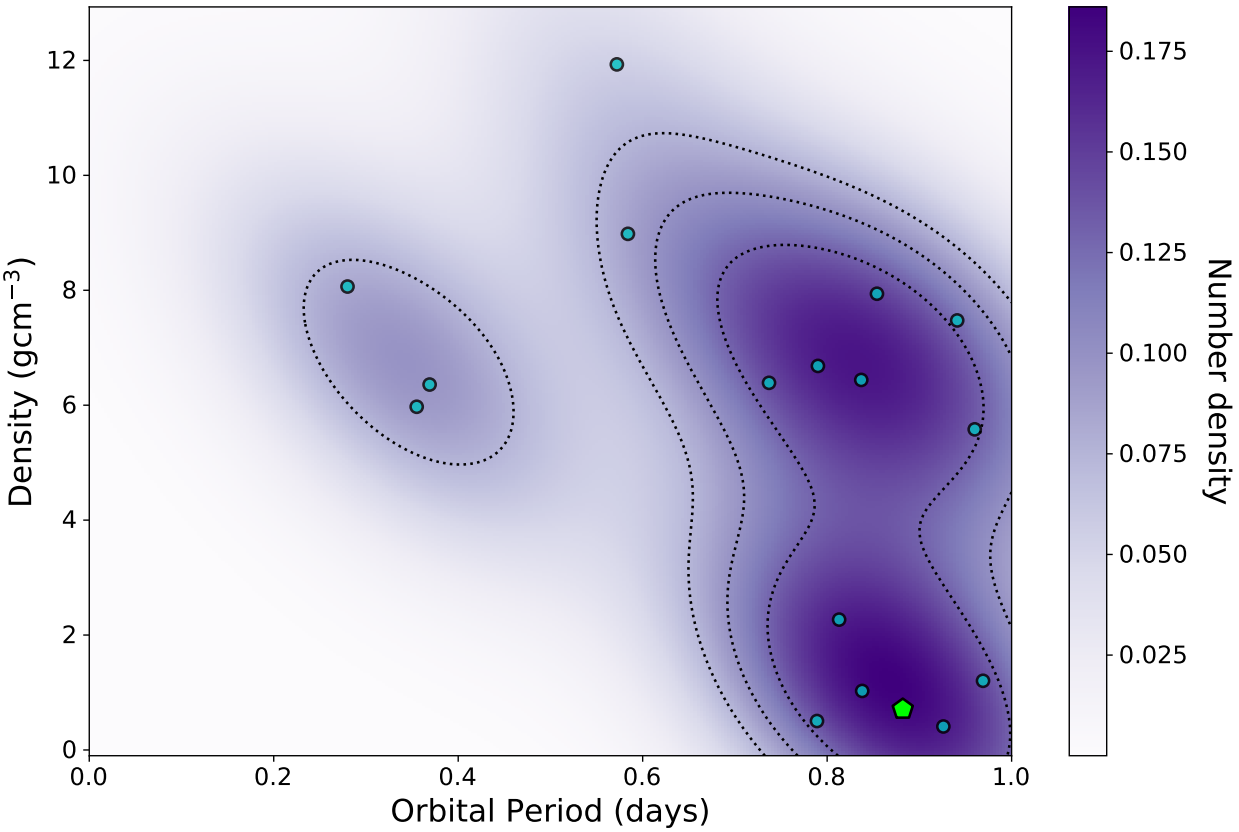

Figure 2.10: Similar to Figure 2.9 except we show the planet bulk density against orbital period.

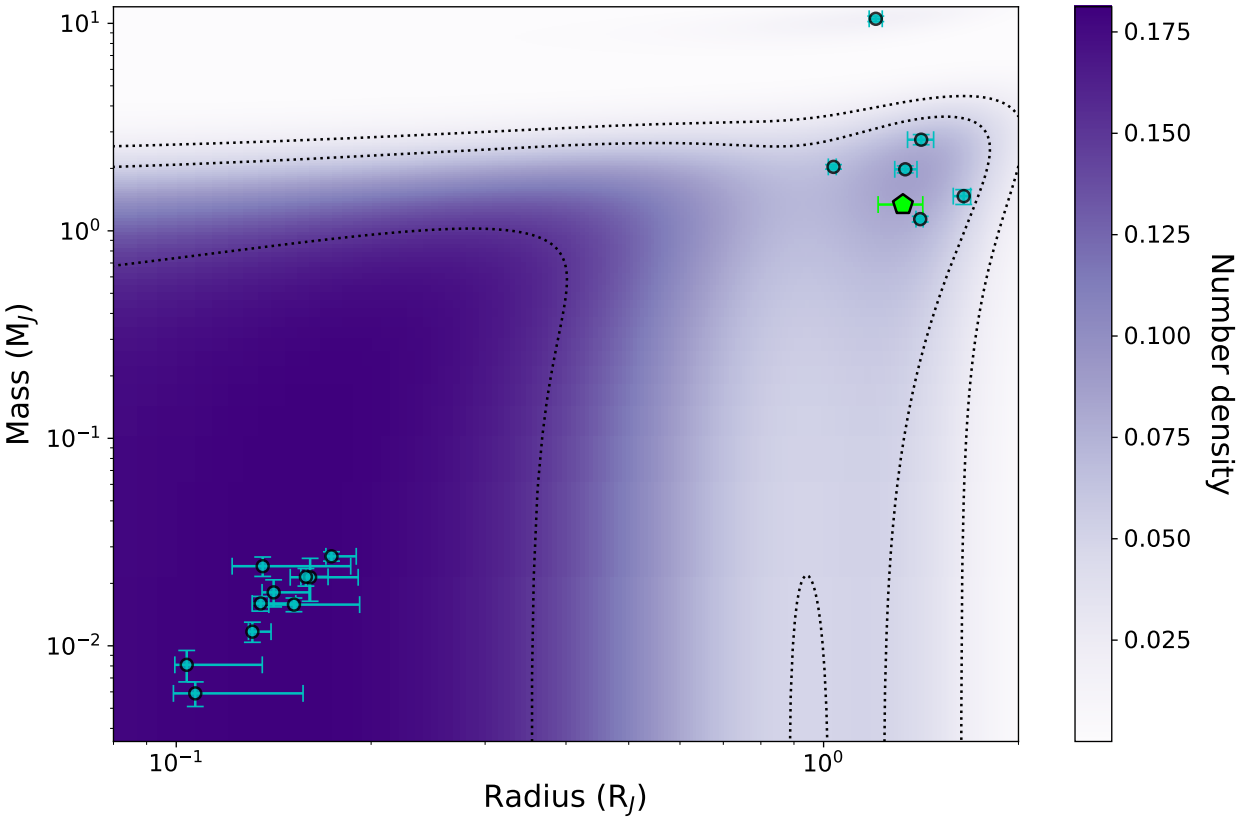

Figure 2.11: Similar to Figures 2.9 and 2.10 except here we show the planet mass against planet radius.

about 5 per cent. This is not enough to have significantly evolved the planet, in line with theoretical studies of HJs (e.g. Murray-Clay et al. 2009; Owen & Jackson 2012).

We found the host star is likely metal-rich, with a value for the iron abundance [Fe/H] of +0.11±0.09 dex. It is well established that gas giant planets favour metal-rich stars (Gonzalez 1997; Santos et al. 2002; Fischer & Valenti 2005; Wang & Fischer 2015), and also short period gas giants, including the HJ population, also appear even more metal-enhanced when compared to their longer period cousins (Jenkins et al. 2017; Maldonado et al. 2018). This trend appears to continue into the USP planet population also (Winn et al. 2017). Approximately 50% of the USP HJ planets host stars are found to have super-solar metallicities ([Fe/H]≥ +0.1 dex), whereas for the smaller super-Earth population, only 30% orbit such stars. Since the USP HJ sample is still significantly smaller than the super-Earth sample, NGTS-6b adds statistical weight to this finding, and the conclusion that this points towards is that both these populations form through core accretion processes, which has a metallicity condition and produce planets with masses lower than 6 M_J, while disc instability models form massive planets (>2 M_J; Matsuo et al. 2007), with the HJ sample forming at relatively large separations from their host stars, and later migrating inwards either through disk driven migration (Mandell et al. 2007; Terquem 2014) or high-eccentricity processes like planet-planet scattering (Rasio & Ford 1996; Ford et al. 2001; Papaloizou & Terquem 2001; Ford & Rasio 2008).

In Mazeh et al. (2016) they defined the upper and lower boundaries of the so called "Neptune desert" region, where it was earlier found that there exists a lack of intermediate mass planets (see Szabó & Kiss 2011; Lundkvist et al. 2016). Since photoevaporation does not appear to have affected the evolution of NGTS-6b significantly, in line with studies of other HJs that define the upper boundary of this desert (Demangeon et al. 2018), the planet may have arrived at its current location through high-eccentricity evolution and was not formed in its current orbital separation. Owen & Lai (2018) suggest that a combination of tidal driven migration to short period orbits through dynamical interactions with other planetary-mass bodies in the system, coupled with photoevaporation of planetary atmospheres can readily describe this sub-Jovian boundary.

The likelihood of a planet-planet scattering evolutionary scenario for NGTS-6b may also be bolstered if the star is indeed metal-rich. We can envisage that the planetary core quickly grew to a size that crossed the critical core mass limit (Mizuno 1980), which is easier to accomplish in metal-rich disks, allowing significant accretion of the surrounding gas. Yet with a metal-rich proto-planetary disk there would be a high fraction of solids remaining for further planetesimals to form close enough to the young NGTS-6b that they could interact and be scattered to wider orbits, or ejected completely from the system (Petrovich et al. 2018). Most USP planets are associated with longer period companions (Sanchis-Ojeda et al. 2014; Adams et al. 2017; Winn et al. 2018), where 52% ± 5% of HJs have additional, longer period companions (Bryan et al. 2016). A concerted effort to search for additional planets further out in the system, whilst constraining better the orbit of NGTS-6b, may shed some light on these scenarios.

Chapter 3

ARIADNE: Measuring accurate and precise stellar parameters through SED fitting

Based on the results published in Vines, J. I., & Jenkins, J. S., *ARIADNE: Measuring accurate and precise stellar parameters through SED fitting*, 2022, MNRAS, 513, 2719.

In this chapter, we describe ARIADNE, a new algorithm for automatically modeling the spectral energy distribution of a star under a Bayesian framework. This is motivated by the fact that there is a small amount of public user-friendly tools for this task and that those tools are subject to model-specific biases (Lebzelter et al. 2012). To combat this, ARIADNE fits archival photometry to several model atmosphere grids and later computes the Bayesian Model Average (BMA) using the Bayesian evidence as model probabilities, creating posterior distribution for stellar bulk parameters (such as effective temperature, log g, metallicity, and radius), which take into account the different physics and geometries assumed in the different models and thus approaching a model-agnostic procedure. This is key for determining planetary bulk parameters, as these are defined in terms of the host star properties.

3.1 SED Modelling with ARIADNE

ARIADNE is designed to automatically fit the SEDs of stars using up to six different atmospheric model grids, in order to obtain effective temperature, surface gravity, metallicity, distance, radius and V-band extinction. We also provide computed parameters such as stellar luminosity and gravitational mass, and isochrone interpolated age and mass. The only required inputs for ARIADNE are the coordinates of the object and optionally, the Gaia DR2 id.

To create the model grids we convolved PHOENIX v2 (Husser et al. 2013), BT-Settl (Allard et al. 2012), BT-NextGen (Hauschildt et al. 1999; Allard et al. 2012), BT-Cond (Allard et al. 2012), Castelli & Kurucz (Castelli & Kurucz 2003), and Kurucz (Kurucz 1993) stellar atmosphere models with commonly available broadband photometry bandpasses:

- Johnson UBV
- Tycho-2 BtVt

- Cousins RI
- 2MASS JHK$_s$
- SDSS *ugriz*
- ALL-WISE W1 and W2
- Gaia DR2v2 G, RP and BP
- Pan-STARRS1 *griwyz*
- GALEX NUV and FUV
- Spitzer/IRAC 3.6μm and 4.5μm
- Strömgren uvby
- TESS
- Kepler
- NGTS

Each SED is modeled with $6 + n$ parameters, highlighted in Equation 3.1, written in standard statistical notation, where n is the number of available photometry measurements. S is the model grid which we interpolate in $T_{\rm eff}$ – log g – [Fe/H] space, and $\varepsilon_{\rm i}$ is the noise model of each photometry measurement that accounts for possible photometric uncertainty underestimations (due to variability, for example), which we expand in Equation 3.2, where $\sigma_{m,{\rm i}}$ is the measurement error of the ith photometry observation, and $\sigma_{{\rm e,i}}$ is the excess noise of the corresponding observation. The fluxes in each grid are given in FLAM units (erg cm^{-2} s^{-2} μm^{-1}) at the surface of the star, so to obtain observed fluxes the SED is multiplied by a normalization factor given by $(R/D)^2$ where R is the radius of the star and D is the distance to the star. We also offer the possibility of fitting for the normalization factor directly instead of radius and distance, and calculate the radius afterwards using the parallax if available. We also model the interstellar extinction A_V by offering four different extinction laws: Cardelli et al. (1989); O'Donnell (1994); Calzetti (2001); Fitzpatrick (1999) provided by the extinction package[1], all of them with fixed ratio of total to selective absorption $R_V = 3.1$. We chose to fix the extinction factor due to it's negligible effect in the overall shape of the SED, though we leave open the possibility of inclusion as an extra parameter in future versions.

$$SF = 10^{-0.4{\rm A_i}} \cdot S(T_{\rm eff}, \log {\rm g}, [{\rm Fe/H}]) \cdot \left(\frac{R}{D}\right)^2 + \varepsilon_{\rm i} \tag{3.1}$$

$$\varepsilon_{\rm i}^2 = \sigma_{m,{\rm i}}^2 + \sigma_{{\rm e,i}}^2 \tag{3.2}$$

Table 3.1 shows the limits in $T_{\rm eff}$, log g and [Fe/H] for each model. Even though we have constrained the upper limit for $T_{\rm eff}$ for all models to a value of 12,000 K for homogeneity, BT-models and the Kurucz models could be extended to higher temperatures in a future update.

[1]https://extinction.readthedocs.io/en/latest/

Table 3.1: SED model limits.

Model	T_{eff}	log g	[Fe/H]
Phoenix v2	[2300, 12000]	[0.0, 6.0]	[-2.0, 1.0]
BT-Settl	[2300, 12000]	[-0.5, 6.0]	[-1.0, 0.5]
BT-NextGen	[2300, 12000]	[-0.5, 6.0]	[-1.0, 0.5]
BT-Cond	[2300, 12000]	[-0.5, 6.0]	[-2.5, 0.5]
Castelli & Kurucz	[3500, 12000]	[0.0, 5.0]	[-2.5, 0.5]
Kurucz	[3500, 12000]	[0.0, 5.0]	[-1.0, 1.0]

3.1.1 Automatic photometry retrieval

The code searches automatically for available photometry using `astroquery`[2] to access the Gaia DR2 (Gaia Collaboration et al. 2016, 2018) archive (for parallax, T_{eff}, and radius when available), MAST and VizieR [3] to query catalogs APASS DR9 (Henden & Munari 2014), ASCC (Kharchenko 2001), ALL-WISE (Wright et al. 2010), 2MASS (Skrutskie et al. 2006), SDSS DR12 (Alam et al. 2015), Pan-STARRS1 (Chambers et al. 2016b), GALEX (Bianchi et al. 2011a), Strömgren Photometric Catalog (Paunzen 2015), GLIMPSE (Spitzer Science 2009), Tycho-2 (Høg et al. 2000) and Gaia DR2 for the magnitudes detailed in Section 3.1. In addition to recovering the magnitudes, we also perform a quality check and reject sources flagged as extended or bad quality by the quality filters of their respective catalogs. In the case where there are magnitudes with no reported uncertainty, we assume they are highly uncertain and calculate their flux uncertainty as $\delta F_i = 1.1 F_i \max(\delta F/F)$, where F_i is the ith flux and F refers to all of the fluxes in the data set. To ensure that we are recovering the correct photometry for the star, we turn to several catalogs that we crossmatch with Gaia, including APASS, ASCC, ALL-WISE, 2MASS, SDSS and Pan-STARRS1. The ASCC crossmatch provides a Tycho-2 identifier which is used in its homonym's and Strömgren catalogs, the GLIMPSE catalog can be searched with the 2MASS identifier recovered from the Gaia-2MASS crossmatch catalog, and finally in the case of GALEX, we do the crossmatch with Gaia using the xMatch query module found in `astroquery`, which serves as an API for the CDS X-Match service.

3.1.2 Prior selection

`ARIADNE` offers flexibility to the user to choose priors for each parameter, but also provides default priors. For the effective temperature, log g, and [Fe/H] we use empirical priors derived from their respective distributions observed by the fifth RAVE survey data release (Kunder et al. 2017). In the case of the log g the possibility of estimating the value using MESA Isochrones & Stellar Tracks isochrones with the `isochrones`[4] package (MIST; Morton 2015; Dotter 2016) exists, where here `ARIADNE` makes use of the Gaia estimates for effective temperature, luminosity and parallax when available, and a subset of the photometry to carry out the interpolations. For the distance we use the Gaia distance derived by Bailer-Jones et al. (2018) (hereafter BJ18) to constrain a normally distributed prior using five times the largest uncertainty as the standard deviation in order to account for offsets in the distance, to avoid reaching machine precision and thus obtaining unrealistically precise posteriors, and for the radius we employ an uninformative flat prior ranging from 0.05 to 100 $R_\odot$. The extinction is limited to the maximum line-of-sight extinction from the updated SFD galactic dust map (Schlegel et al. 1998; Schlafly & Finkbeiner 2011) through the `dustmaps` python

[2]https://astroquery.readthedocs.io/en/latest/
[3]http://vizier.u-strasbg.fr/
[4]https://isochrones.readthedocs.io/en/latest/

Table 3.2: `ARIADNE` default priors

Parameter	Prior
$T_{\rm eff}^{\dagger}$	RAVE
log g	$\mathcal{N}(g, g_{\rm e}^2)$
[Fe/H]	$\mathcal{N}(-0.125, 0.234^2)$
D	$\mathcal{N}(D, (5D_{\rm e})^2)$
R_*	$\mathcal{U}(0.05, 100)$
A_V	$\mathcal{U}(0, av)$

Where g, $g_{\rm e}$ is the MIST log g estimate and its uncertainty, D, $D_{\rm e}$ is the BJ18 distance estimate with the largest errorbar, and av is the largest line-of-sight extinction in the SFD galactic dust map. For details see the text.
† The effective temperature prior is drawn from the empirical temperature distribution from the fifth RAVE data release.

package (M. Green 2018). The excess noise terms have zero mean gaussian priors, with three times the squared uncertainty set as the variance, and finally the normalization factor has an uninformative prior. We show a quick summary of the priors in Table 3.2.

Though we offer up to six atmospheric model grids, there are restrictions on which ones can be used. Kurucz (1993) and Castelli & Kurucz (2003) models are known to be unreliable with low temperature stars, thus they can't be chosen as models for stars with temperatures below 4000 K. On the other hand, the BT-suite of models does not show significant variation for temperatures above 4000 K (Figures 3 and 4 from Allard et al. 2012), meaning that applying the three models on stars in this temperature regime can induce bias in the final stellar parameter uncertainties, which led to our decision of limiting the BT-suite of models to only BT-Settl for these types of stars.

3.1.3 Bayesian Model Averaging

BMA is an extension to the usual Bayesian inference framework, where one does not only fit a single model to obtain parameters and uncertainties (and sometimes the so-called model evidence), but one also fits different models and can potentially account for model-specific systematic biases, allowing for model selection, prediction and combined estimation; the latter being the focus in this paper (Fragoso et al. 2018). Firstly, recall Bayes' theorem:

$$P\left(\hat{\theta}|X, M\right) = \frac{P\left(X|\hat{\theta}, M\right) P\left(\hat{\theta}|M\right)}{P(X|M)} \tag{3.3}$$

Where X is the observed data, $\hat{\theta}$ is the parameter vector corresponding to model M, $P\left(X|\hat{\theta}, M\right)$ is the likelihood function, $P\left(\hat{\theta}|M\right)$ is the prior function, and the denominator $P(X|M) = \int P\left(X|\hat{\theta}, M\right) P\left(\hat{\theta}|M\right) \mathrm{d}\hat{\theta}$ is the marginalized likelihood of model M with parameters $\hat{\theta}$, which is also referred to as the model evidence or Bayesian evidence; this quantity lies at the heart of BMA. It is possible to derive posterior probabilities for different models M_j by applying Bayes' theorem as shown in Equation 3.4. The combined distribution for the jth parameter, $\bar{\theta}_j$, is then given by the weighted average of the N considered models, where the weight of the nth model is its posterior probability, as shown in Equation 3.5. In this work we assume that all models are equally probable, a priori, so Equation 3.4 reduces to normalizing the evidence of each model by the sum

of all the available evidences.

$$P(M_j|X) = \frac{P(X|M_j)P(M_j)}{\sum_{n=1}^{N} P(X|M_n)P(M_n)} \tag{3.4}$$

$$P(\bar{\theta}) = \sum_{n=1}^{N} P(\hat{\theta}_n|X, M_n)P(M_n|X) \tag{3.5}$$

For `ARIADNE`, the likelihood function is gaussian, as defined in Equation 3.6, where f_i is the ith measured flux, $\mathrm{SF}_{\mathrm{i,M}}$ is the ith synthetic flux produced by model M, and ε_i is the excess noise term explained in Equation 3.2.

$$\mathcal{L} = \prod_{\mathrm{i}=1}^{N} \frac{1}{\sqrt{2\pi\varepsilon_\mathrm{i}^2}} \exp\left(-\frac{1}{2}\left(\frac{f_\mathrm{i} - \mathrm{SF}_{\mathrm{i,M}}}{\varepsilon_\mathrm{i}}\right)^2\right) \tag{3.6}$$

In this work, we implement BMA in two different ways to combine the posterior distribution of up to six different atmospheric models to account for possible systematic biases in the physics inputs for different models, approaching a model agnostic solution.

The first implementation, which we will refer to as averaging, consists of taking the posterior samples of each model and performing a weighted average using each model's relative probability, (computed from their evidences), as weights. The second method, which we will refer to as sampling, consists of creating a master posterior from each model's posterior samples and then re-sampling from that master posterior in order to obtain the final distributions for each parameter. This is equivalent to estimating the probability density function (PDF) of each distribution, and then performing a weighted average over them using the same methodology for the weights as previously described. These two methods use Equations 3.4 and 3.5 as a basis, and throughout the paper it is explicitly stated which of the two methods has been employed.

The difference between averaging and sampling is twofold: the first is the width of the credibility intervals of each parameter, with the averaging producing more precise values and the sampling generating wider intervals in general. The second difference is important in the cases where the models themselves are in disagreement, since here the sampling will produce an estimated value drawn from the model with the highest relative probability, while the averaging produces a value that lies somewhere between the models (see Sec. 3.3.1 for an example).

3.1.4 Parameter estimation

To estimate the best-fitting parameters we turn to nested sampling algorithms (Skilling 2004, 2006), which are designed to estimate the Bayesian evidence (marginal likelihood) of a given model, and as a by-product, the posterior distribution. These types of algorithms offer some advantages over typical Bayesian inference tools, such as MCMC algorithms (Robert & Casella 2011 and references therein). For example, they estimate the aforementioned Bayesian evidence, they employ a well-defined stopping criterion, and provide an overall better performance in multi-modal or degenerate posterior spaces.

The evidence of a model is an essential quantity that is usually hard to calculate or estimate through either

analytical or numerical methods. In problems with high dimensionality, or multimodal posteriors, there is seldom a closed analytical expression for the evidence, and it plays an important role in model selection, along with BMA (as detailed in Section 3.1.3)

In order to calculate the Bayesian evidence and estimate the parameter posterior distribution with `ARIADNE` we used `MultiNest` (Feroz et al. 2009) through `PyMultiNest` (Buchner et al. 2014) for (importance) nested sampling and `dynesty` (Speagle 2019) for (dynamic) nested sampling (Higson et al. 2019). The main difference between regular, or 'static' nested sampling and 'dynamic' nested sampling is the ability of the latter to prioritize parameter estimation over evidence calculation. For a more in depth discussion on the differences between both methods the reader is referred to Buchner (2016).

3.1.5 General algorithm

Here we describe the main `ARIADNE` algorithm:

1. If no Gaia DR2 id is provided, `ARIADNE` searches for one with the provided RA and DEC.
2. With the Gaia DR2 id, an estimate for the $T_{\rm eff}$ is queried from the Gaia DR2 catalogue. This temperature is used to select the models to fit for.
3. A query is done to the Gaia DR2 crossmatch catalogs to see if the star is available in any of them, and if so, their respective ids are retrieved
4. Each catalog is queried for the corresponding ids from the previous item in order to retrieve the photometry and associated uncertainties. At the moment of retrieval, a quality control check is performed, checking each catalog's quality control flags, if any are available.
5. If requested, a log g estimate is calculated using MIST isochrones.
6. The main fitting routine is executed, which consists of fitting individually and independently each selected atmospheric model.
7. The original posterior samples are re-sampled randomly with n samples, (indicated by the user), and those re-sampled posterior samples are then averaged following Sect. 3.1.3.
8. The best fitting parameters are calculated using a kernel density estimation of the marginalized posterior samples, and the uncertainties are computed from the minimum highest density region at a 68% significance level (Hyndman 1996).
9. Age and mass are interpolated from MIST isochrones, with the best fit parameters and photometry used as input.

It is possible to fit single models as well, without doing BMA. In this case, however, ages and masses are not interpolated from the isochrones and only the gravitational mass is available. For more information on the gravitational mass and its comparison with the isochrone interpolated mass, the reader is referred to Section 3.3.5. `ARIADNE` can also be run in parallel with both `MultiNest` and `dynesty` through OpenMPI and native python parallelization, respectively.

We have tested `ARIADNE` on a Macbook Pro with an Intel(R) Core(TM) i7-7820HQ CPU @ 2.90GHz with 4 cores and 8 threads. Fitting individual models using `dynesty` with 500 live points and a stopping threshold of dlog z < 0.01, parallelized to 8 threads, takes on average five minutes; the whole BMA procedure using all

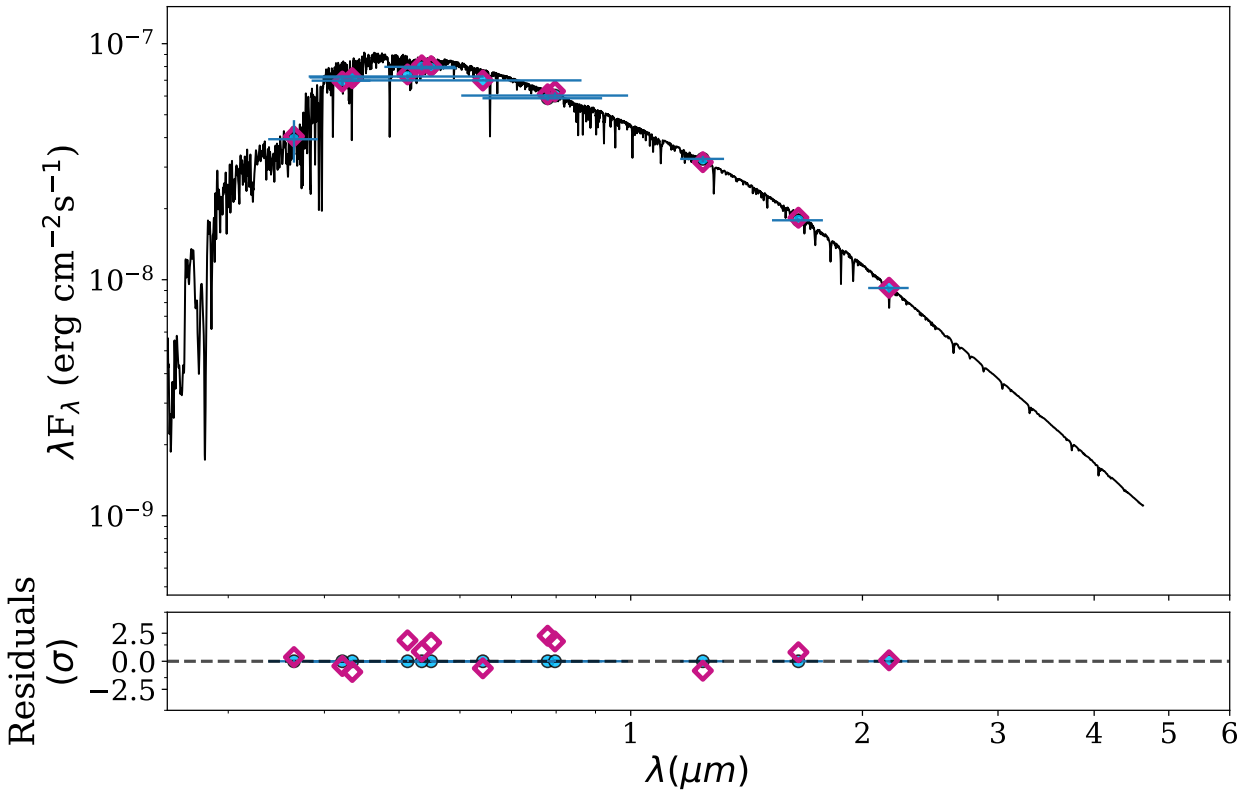

Figure 3.1: Top: HD 113337 BT-Settl SED plot. The blue circles are the retrieved photometry and their horizontal errorbars show the width of the filter bandpass. The magenta diamonds are the synthetic photometry. Bottom: Residuals of the fit, normalized to the photometry errors.

six available models takes from 20 to 45 minutes depending on the star. An important note is that M dwarfs take a significant longer time to fit, meaning the BMA procedure can take up to an hour and a half with the previous settings.

As standard output `ARIADNE` provides a text file containing the best fitting parameters with their associated uncertainties and their 3-σ confidence intervals, another text file showing the photometry that was used, a third text file hosting the relative probabilities of each model, a plot of the best fitting SED model with the recovered photometry (see Sect.3.1.1) and synthetic photometry, a corner plot (Foreman-Mackey 2016) of the fitted parameters, a Hertzsprung-Russell (HR) diagram drawn from the MIST isochrones, and finally histograms showing the parameter distribution for each model. For examples of these outputs see Figures 3.1, 3.2, 3.3 and 3.5 respectively.

3.2 Benchmark stars

To test the accuracy of `ARIADNE` we compiled a list of interferometrically observed stars, as these can provide direct measurements of the radius through the limb-darkened angular diameter and parallax distance. The selected stars cover the spectral range from A to M dwarfs, with a sub-sample of evolved stars allowing us to probe larger radii and masses, and lower log g values. In addition to compiling interferometric radii and effective temperatures, we also searched the literature for log g and metallicity values to compare against our outputs. In total we compiled 135 stars with radii and effective temperatures ranging from 0.15 to 16.57 $R_\odot$ and 2940 to 9377 K respectively. We list the selected stars with their respective references in Table 3.3, along

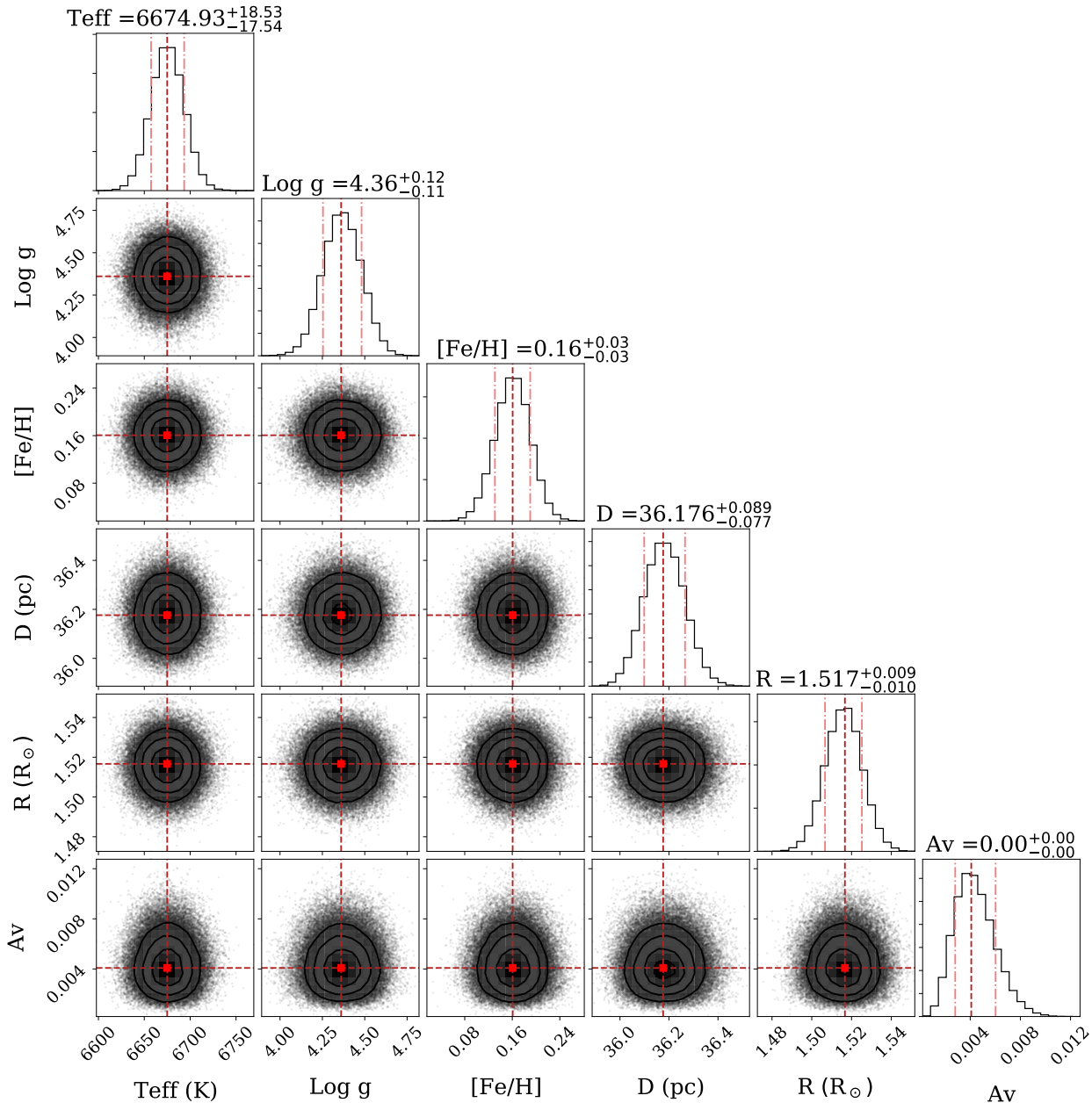

Figure 3.2: HD 113337 cornerplot showing the averaged distributions obtained through the averaging method.

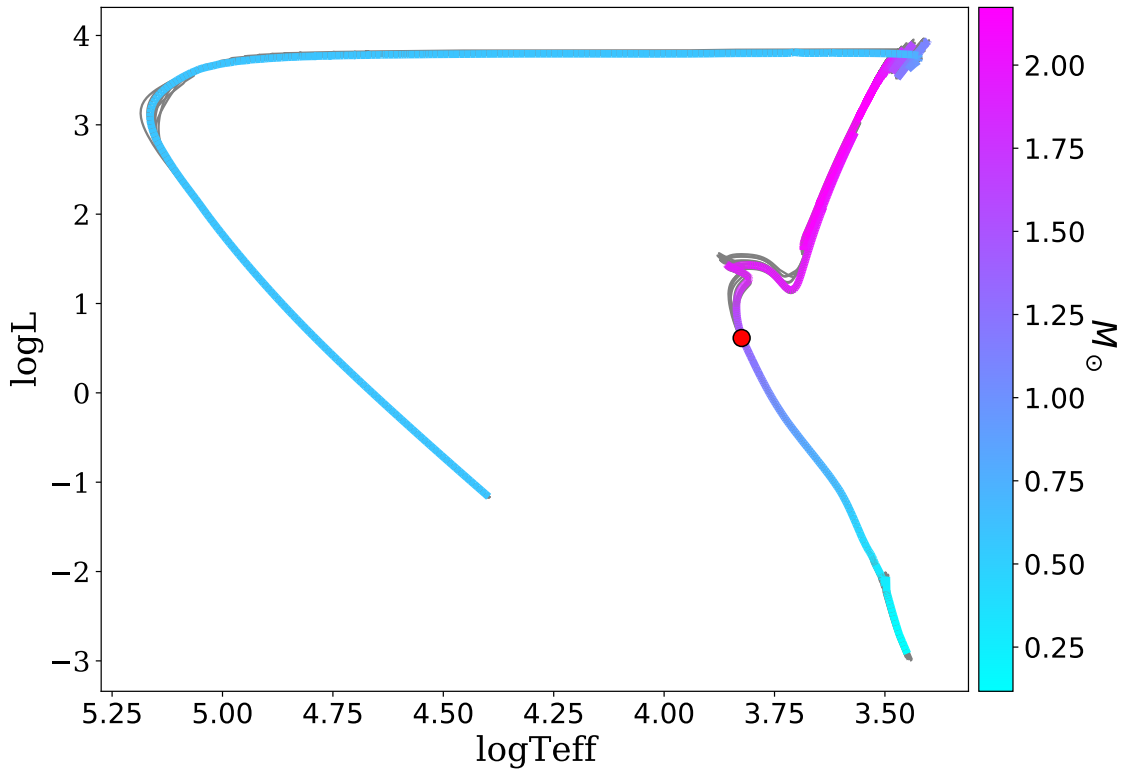

Figure 3.3: HD 113337 HR diagram drawn from interpolating the MIST isochrone grid to the best fitting stellar parameters. The errorbars are smaller than the symbol. The gray lines are drawn randomly from the fitted parameter samples.

with their associated magnitudes in Table 3.4. For each one of the benchmark stars, we ran `ARIADNE` with the default priors, except for metallicity (see Sec. 3.3.4), and using the Fitzpatrick (1999) extinction law (testing the effects of using different extinction laws is beyond the scope of this work). We also refer the reader to other published works that have made use of `ARIADNE` to calculate stellar parameters for stars up to 3 kpc away (e.g. see Díaz et al. 2020a; Jenkins et al. 2020b; Acton et al. 2020; Tilbrook et al. 2021; Smith et al. 2021).

Table 3.3: Benchmark stars used to test `ARIADNE`. A full version is available as supplementary material in machine-readable format. The first rows are provided for guidance

Star Name	T_{eff} K	log g dex	[Fe/H] dex	θ_{LD} mas	Radius $R_\odot$	log R_{HK} dex	Refs
HD166	5327 ± 39	4.58 ± 0.11	0.08 ± 0.11	0.624 ± 0.009	0.917 ± 0.009	-4.36	27,19
HD48737	6480 ± 39	3.61 ± 0.10	-0.09	1.401 ± 0.009	2.710 ± 0.021	-4.03	20,21
⋮	⋮	⋮	⋮	⋮	⋮	⋮	⋮

Notes. log R_{HK}. values from Boro Saikia et al. (2018)
Assumed 10% uncertainties on values where there are none reported.
References. (1) Rains et al. (2020); (2) Delgado Mena et al. (2017); (3) Jenkins et al. (2011); (4) Blackwell & Lynas-Gray (1998)
(5) Erspamer & North (2003); (6) Royer et al. (2007); (7) Martínez-Arnáiz et al. (2010); (8) Ramírez et al. (2013); (9) Massarotti et al. (2008)
(10) Allende Prieto et al. (2008); (11) Alves et al. (2015); (12) Liu et al. (2007); (13) Hekker & Meléndez (2007); (14) Torres et al. (2006)
(15) Boyajian et al. (2012); (16) Fischer & Valenti (2005); (17) Casagrande et al. (2011); (18) Mallik et al. (2003); (19) Soubiran et al. (2016)
(20) Boyajian et al. (2012); (21) Gray et al. (2003); (22) Anderson & Francis (2012a); (23) von Braun et al. (2014); (24) Rojas-Ayala et al. (2012)
(25) Torres et al. (2008); (26) Boyajian et al. (2015); (27) Boyajian et al. (2013); (28) Borgniet et al. (2019)
(29) Ligi et al. (2019); (30) Brewer et al. (2016); (31) Mortier et al. (2013); (32) White et al. (2018)
(33) Tanner et al. (2015); (34) Lachaume et al. (2019); (35) Houdebine et al. (2019); (36) Stokholm et al. (2019)
(37) Johnson et al. (2014); (38) Ligi et al. (2016); (39) Berger et al. (2006); (40) Huber et al. (2016)
(41) Ammons et al. (2006); (42) Bourges et al. (2017); (43) Bigot et al. (2011); (44) von Braun et al. (2011)
(45) Santos et al. (2004); (46) Baines et al. (2008); (47) Mozurkewich et al. (2003); (48) Huber et al. (2012)
(49) Crepp et al. (2012); (50) Nordgren et al. (1999); (51) van Belle & von Braun (2009); (52) Baines et al. (2012)

Table 3.4: Magnitudes of the benchmark stars used to test ARIADNE. A full version is available as supplementary material in machine-readable format. The first rows and columns are provided for guidance

Star Name	2MASS_H	2MASS_H_e	2MASS_J	2MASS_J_e	2MASS_Ks	2MASS_Ks_e	...
GJ1139	6.707	0.020	7.315	0.021	6.594	0.021	...
GJ1189	6.841	0.020	7.385	0.027	6.742	0.029	...
GJ15A	4.476	0.200	5.252	0.264	-	-	...
GJ166A	2.594	0.198	3.013	0.238	2.498	0.236	...
⋮	⋮	⋮	⋮	⋮	⋮	⋮	...

3.3 Results

In the following section we discuss the results obtained when running ARIADNE on the benchmark stars, investigating the precision of the code for the main atmospheric parameters: $T_{\rm eff}$, $\log g$, [Fe/H], radius, and mass. We have compiled all of ARIADNE's outputs in Table 3.5.

Table 3.5: ARIADNE outputs for the benchmark stars with their 1-σ errorbars. A full version is available as supplementary material in machine-readable format. The first rows are provided for guidance.

Star Name	T_{eff} K	log g dex	[Fe/H] dex	Radius $R_\odot$	$Mass_{grav}$ $M_\odot$	$Mass_{iso}$ $M_\odot$	θ_{LD} mas	A_V mag
HD 209458	5994^{+13}_{-7}	$4.38^{+0.03}_{-0.07}$	$0.19^{+0.02}_{-0.01}$	$1.213^{+0.009}_{-0.007}$	$1.28^{+0.09}_{-0.22}$	$1.15^{+0.01}_{-0.01}$	$0.2328^{+0.0018}_{-0.0020}$	$0.005^{+0.001}_{-0.003}$
HD 189733	5049^{+19}_{-16}	$4.51^{+0.09}_{-0.10}$	$-0.03^{+0.03}_{-0.04}$	$0.765^{+0.007}_{-0.006}$	$0.66^{+0.10}_{-0.21}$	$0.81^{+0.01}_{-0.01}$	$0.3593^{+0.0025}_{-0.0038}$	$0.002^{+0.000}_{-0.005}$
HD 113337	6675^{+18}_{-19}	$4.36^{+0.11}_{-0.12}$	$0.16^{+0.03}_{-0.03}$	$1.517^{+0.010}_{-0.009}$	$1.79^{+0.29}_{-0.75}$	$1.40^{+0.01}_{-0.02}$	$0.3898^{0.0026}_{-0.0025}$	$0.004^{+0.001}_{-0.002}$
⋮	⋮	⋮	⋮	⋮	⋮	⋮	⋮	

3.3.1 Radius accuracy

Due to the nature of the model, the radius correlates directly with the distance through the normalization factor defined in Section 3.1. The distance is tightly constrained by the BJ18 derived distances, thus giving highly constrained values for $R_\star$, even when using uninformative priors. To highlight this effect, we ran `ARIADNE` on the planet hosting star HD 113337 using both the BJ18 distance and Hipparcos parallax as priors for the distance to the system. We found radii of 1.52 ± 0.01 $R_\odot$ and $1.58^{+0.05}_{-0.04}$ $R_\odot$ for the BJ18 distance and Hipparcos' distance, respectively, revealing an offset at a level higher than 1-σ from the BJ18 value, as well as uncertainties three to five times larger. Since most of the stars listed in Table 3.3 had their radii calculated using the parallax from Hipparcos (van Leeuwen 2007), which are significantly less well constrained than Gaia, and in most cases have an offset, we re-calculated the radii of the stars using the BJ18 distance and compared those values to `ARIADNE`'s output. In Figure 3.4a, we highlight that the interferometrically observed radii and our measured values follow a 1:1 relation, with fractional RMS values of 0.001 ± 0.070 and 0.000 ± 0.069, and mean precisions of 2.1% and 4.3% for the averaging and sampling methods, respectively. While the expected scatter derived from interferometrically observed stars ranges from 1.5% for A, F and G stars to 5% for K and M stars, we chose the more conservative value of 5% for comparison (Stassun et al. 2017), and find that the intrinsic scatter computed from `ARIADNE` lies well within the interferometric scatter. We find an increasing trend for the smallest stars, those with $R_\star \lesssim 0.4 - 0.5 R_\odot$, (the M dwarfs), and therefore it appears more work is necessary to properly model these objects, both in the community and within ARIADNE itself. However, we also note that the slope does not cross the blue interferometric scatter region, showing that the effect is small in reality.

For comparisons sake, we also compute angular diameters for the benchmark stars from `ARIADNE` derived $R_\star$ and distance outputs (recall the angular diameter definition: $\Theta \equiv 2R_\star/\mathrm{d}$) and compared them to the interferometrically observed angular diameters. Our results show that the angular diameters derived from the SED fit correlates well with the observational counterpart, as shown in Figure 3.4b.

To show the effect BMA and proper weighting has on the precision of the stellar parameters, in particular for radii, we provide histograms showing the distribution of each model, alongside the probability associated with them, and the distribution of the averaged posterior samples, all part of the `ARIADNE` standard output. An example of these histograms are shown in Figure 3.5. In addition, Figure 3.6 shows the effect averaging has on the final radius value in the sample. We note that there are four main behaviors for the radii posteriors. The best case scenario is that all of the model posteriors agree within 1-σ, case highlighted in Figure 3.5a. Figure 3.5b shows the case where there are two distinct groups (separated by more than 2-σ) where the posteriors are clustered. The third case, shown in Figure 3.5c, is where the models are separated across a wide area of the parameter space, with no dominant single model. The second and third cases are where BMA has the largest impact, (although in the first case, where all models agree within 1-σ, BMA further constrains the final posterior distribution giving a more precise value), unifying the conflicting models by weighting them by their probabilities. Figure 3.5d is the fourth scenario where a single model dominates over the rest, and in this case BMA is performing model selection.

3.3.2 Teff accuracy

The effective temperature of a star is a key parameter, as it is one of the main determinants in the overall shape of the SED and thus can be precisely determined from SED fits alone, mostly with uncertainties smaller than ± 100 K. Effective temperature also helps to further constrain the radius. We found that `ARIADNE` reproduces the $T_{\rm eff}$ literature values accurately. We show this comparison in Figure 3.7. We also tested varying the priors for the temperature between 2-10 times the error reported and adding ± 100 K to the value reported

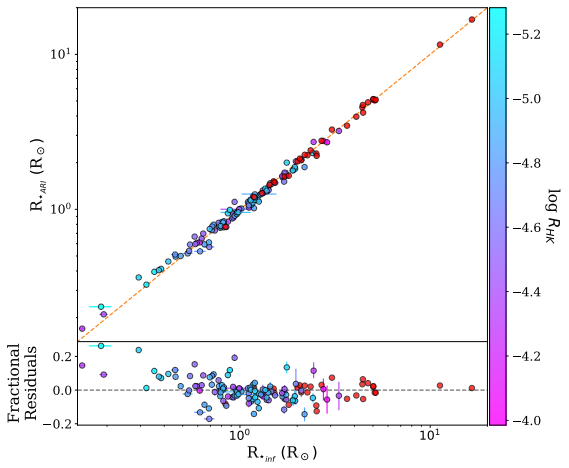

(a) The ARIADNE $R_\star$ from the averaging method compared to computed interferometric radii from angular diameters and BJ18 distances, color coded with log R_{HK}. The red dots are stars without a log R_{HK} measurement. The dashed orange line represents the 1:1 relation. The lower panel shows the fractional residuals which indicate a rising trend for the smallest stars.

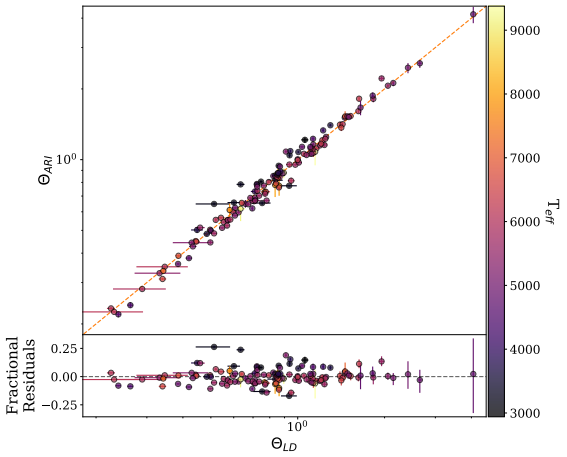

(b) Computed angular diameters from the ARIADNE $R_\star$ computed with the averaging method shown in (a) and the distance outputs compared to interferometric observations of angular diameters from the benchmark stars. The dashed orange line represents the 1:1 relation. The lower panel shows the fractional residuals, which, as opposed to the radius plot, does not show significant behavior with varying angular diameter.

Figure 3.4: Comparison between literature radii and angular diameters vs our outputs.

by the literature to test the effect that wider priors have on the precision of the fit. In these cases, we found that there is a slight decrease in precision of around ±10 K when using an extremely wide prior, such as the RAVE prior (see Sect. 3.1.2), otherwise ARIADNE is insensitive to T_{eff} prior choice. We also note that using a wider prior for the temperature decreases the radius precision by around a factor of two.

3.3.3 log g accuracy

The surface gravity is hard to capture from SEDs alone, and using a global prior drawn from RAVE tends to consistently underestimate the log g. Therefore, we recommend drawing a prior from an independent method, such as spectral analysis. There is an important reservation regarding using evolutionary codes, such as MIST, for the estimation of the log g, since they could possibly use, or incorporate, archival photometry, which could have the knock-on effect of arriving in a position where data has been used twice when running the analysis with ARIADNE. For the analysis done on the benchmark stars, the log g prior was taken from the literature values, and whenever the log g was missing, a Uniform prior between 3.5 and 6.0 was used instead. Figure 3.8 shows the comparison with the literature values excluding those stars where no literature log g could be found.

3.3.4 Metallicity

The metallicity cannot be consistently constrained through our SED fitting procedure when using an unconstrained prior such as the one drawn from RAVE (see Sect. 3.1.2). This is mainly because the metallicity has a negligible effect on the overall shape of the SED and instead affects narrow absorption lines, something that is not effectively captured by broadband photometry. We also tested including narrow-band photometric

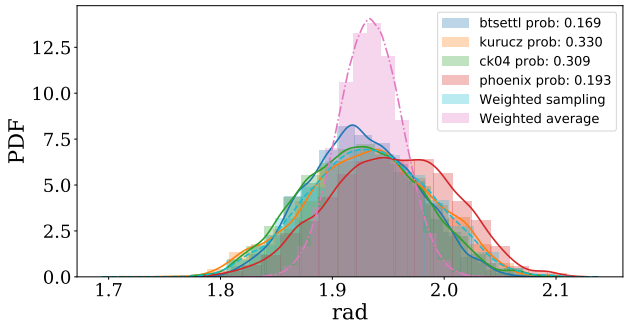

(a) HD 222603. Best case scenario where all models agree and the probabilities are approximately equally distributed. The dot-dashed line represents the averaged distributions while the dashed line shows the distribution drawn from the weighted sampling. This applies for all panels in this Figure.

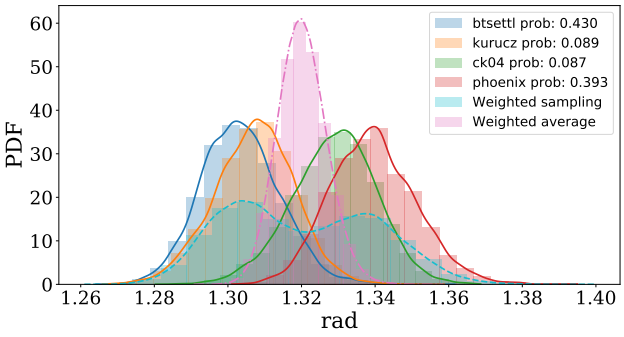

(b) HD 143761. There are two groups of posteriors, one with the PHOENIX v2 and Castelli & Kurucz, and another with BT-Settl and Kurucz models.

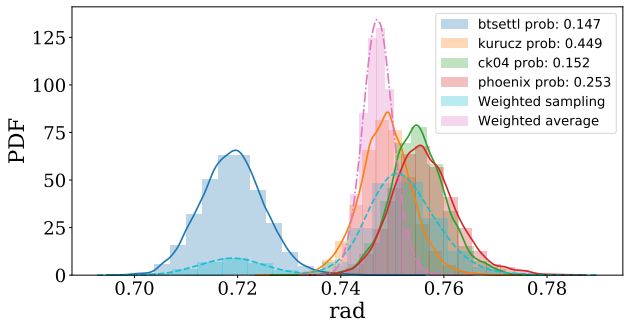

(c) GJ 33. The posterior samples are, in general, separated and each model has a similar probability.

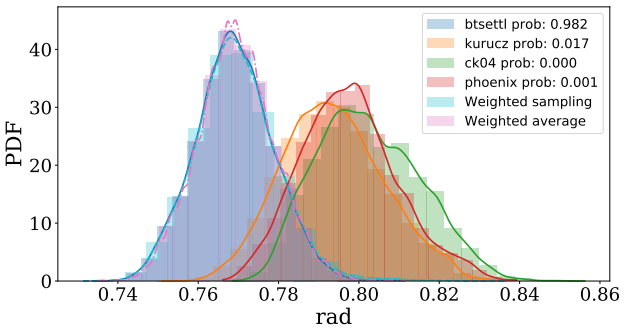

(d) HD 170493. There is a single dominant model. Note that in this case the model averaging reduces to model selection and thus the averaged histogram is nearly identical to the dominant model.

Figure 3.5: Radius posterior samples for different stars with each model's probability and the averaged posterior highlighting various possible scenarios when modeling stars with `ARIADNE`. There is no immediate correlation between these scenarios and the properties of the stars, except for the M dwarfs, where we have observed case (d) to be the most frequent.

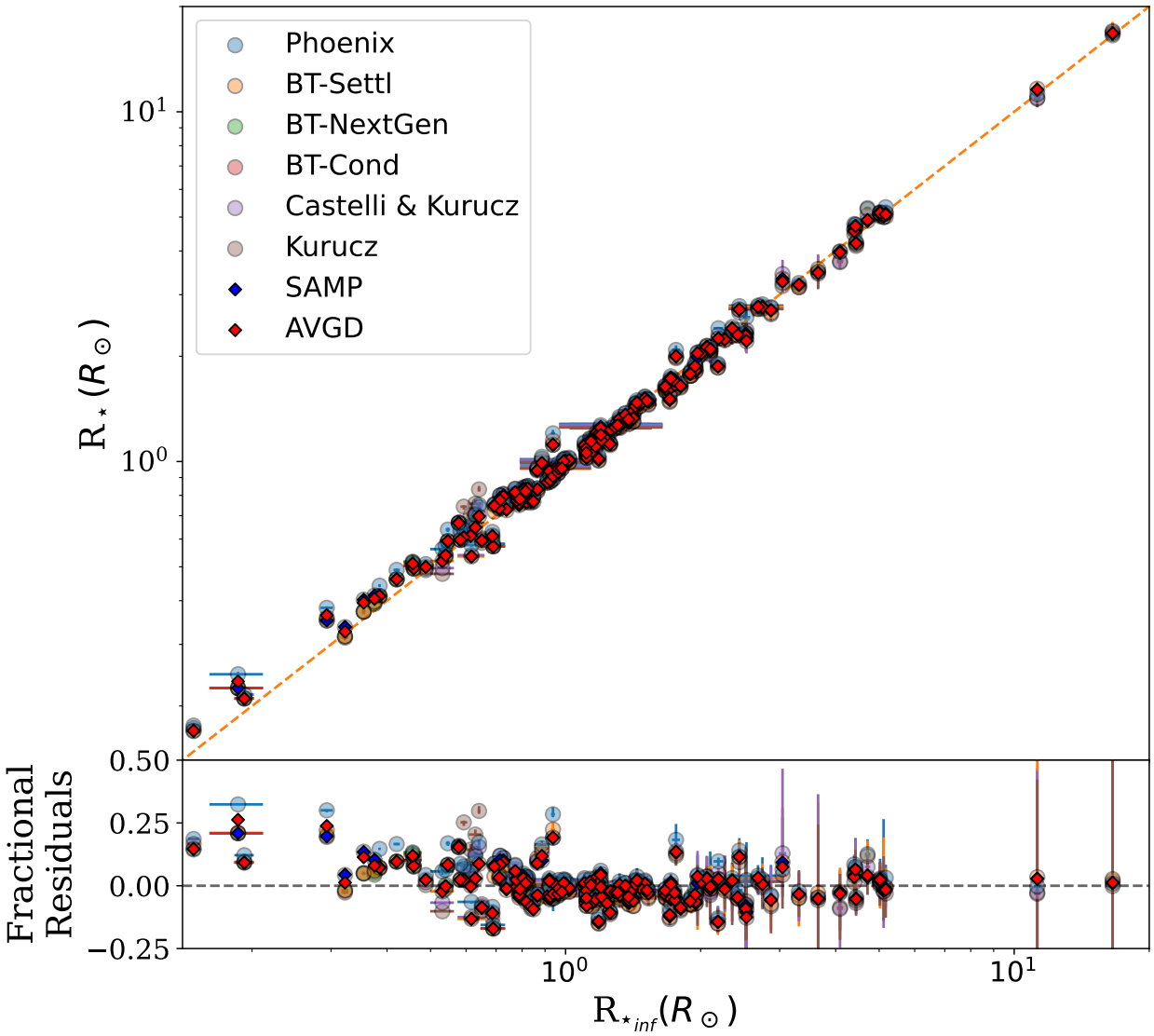

Figure 3.6: Radii calculated with `ARIADNE` compared against the interferometric values. Individual model estimates are shown, along with the averaging values in red diamonds and the sampling values in blue diamonds. It can be seen that in most cases the averaged values are more accurate than the individual models. The lower panel shows the fractional residuals where it can be seen that the most accurate values lie in the 0.75-1.50 $R_\odot$ range, and the rising trend for the smallest stars ($R_\star$ <~0.4-0.5 $R_\odot$) is also apparent.

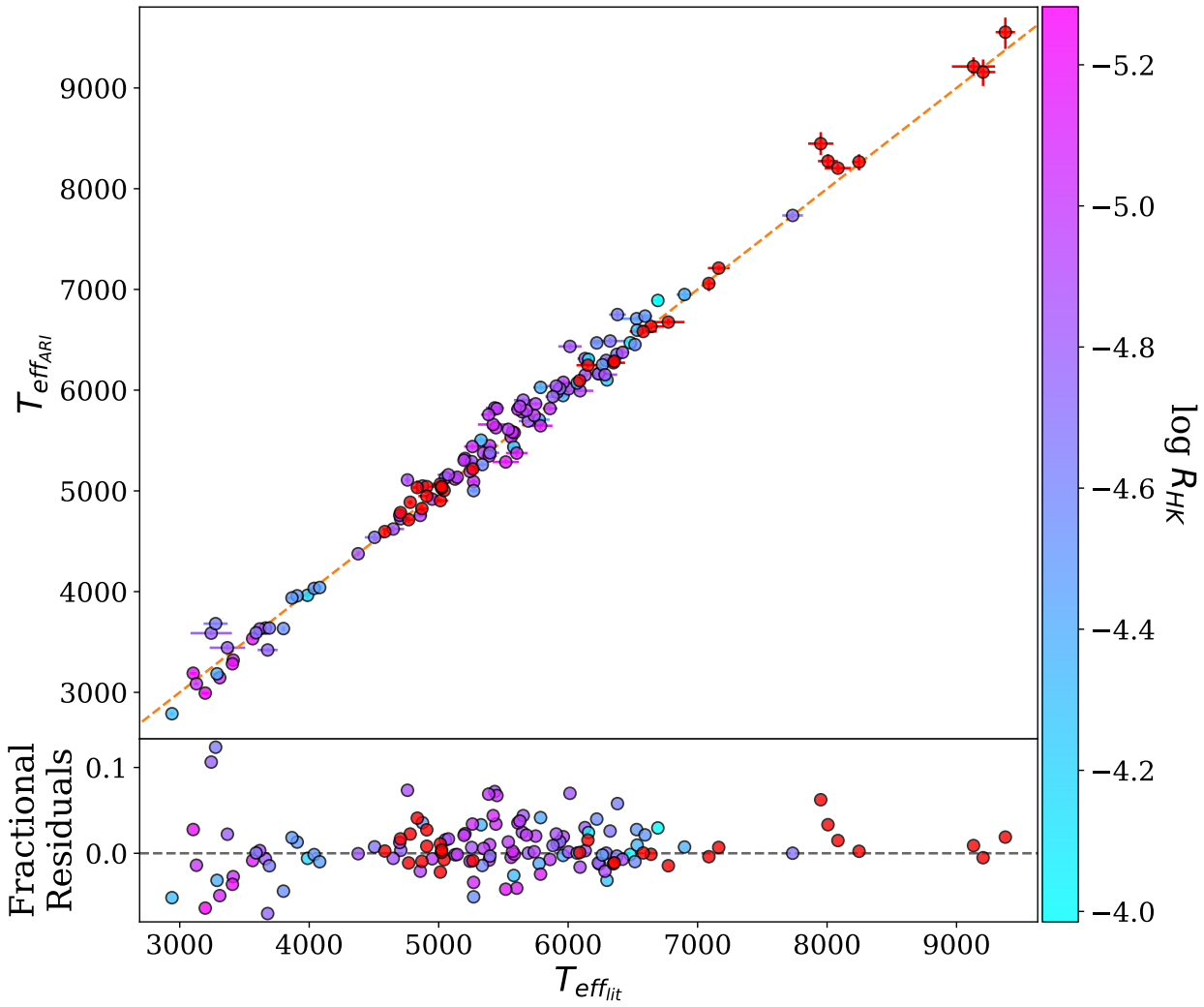

Figure 3.7: ARIADNE T_{eff} from the averaging method output compared against literature values for the benchmark stars. The dashed blue line represents the 1:1 relation. The lower panel shows the residuals.

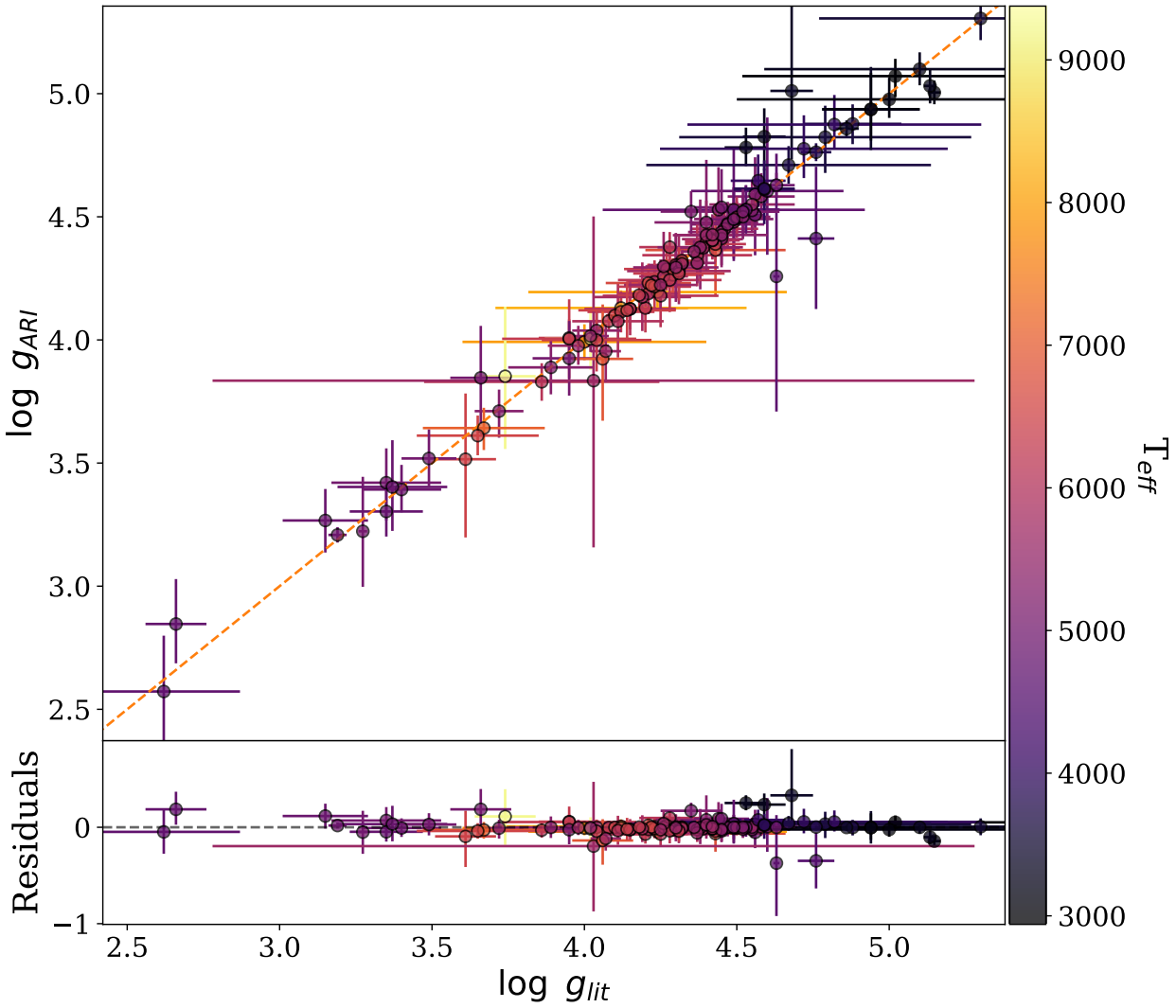

Figure 3.8: `ARIADNE` log g from the averaging method output compared against literature values for the benchmark stars. The dashed orange line represents the 1:1 relation. The lower panel shows the residuals.

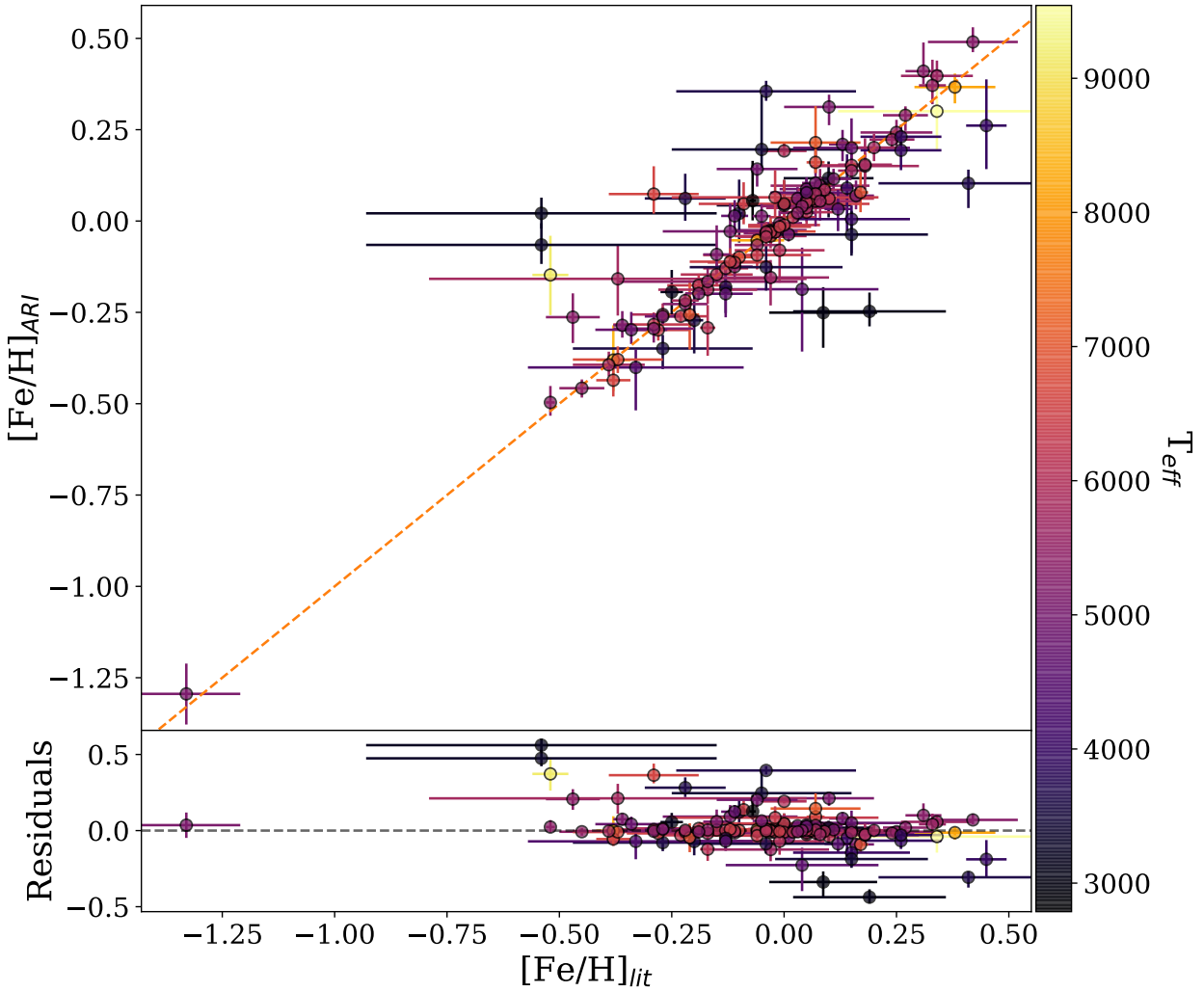

Figure 3.9: `ARIADNE`'s [Fe/H] from the averaging method output compared against literature values for the benchmark stars. Each star is color coded by it's effective temperature, taken from the literature. The dashed orange line represents the 1:1 relation. The lower panel shows the residuals.

measurements in the fitting procedure, in particular the Strömgren filters that were designed to measure metallicities of stars, however these also proved ineffective in increasing the accuracy of our metallicity measurements. Including spectroscopically derived priors drastically improves the accuracy for the metallicity, so we drew priors from the PASTEL catalog (Soubiran et al. 2016) when available. Figure 3.9 shows our metallicity results using this prior.

3.3.5 Mass calculation

We offer two methods of calculating stellar masses with `ARIADNE`. The first is the so-called gravitational mass, M in units of the Solar mass, which is calculated directly from the star's log g and R in units of Solar radius, using equation 3.7

$$g = g_\odot \frac{M}{R^2} \tag{3.7}$$

which after taking the logarithm becomes

$$\log g = \log M - 2 \log R + 4.437 \tag{3.8}$$

The second method involves interpolating MIST isochrones to the previously fitted stellar parameters and broadband photometry, however this option is only available when doing the BMA procedure and not for individual model fitting.

3.4 What makes ARIADNE unique?

As mentioned in the introduction, a number of algorithms and methodologies have been developed to measure stellar bulk properties, however only one employs Bayesian statistics (Gillen et al. 2017), and they only apply the analysis to an individual model set. VOSA on the other hand, is a public web-tool designed to build SEDs and obtain different properties from Virtual Observatory catalogs, by modeling SEDs with synthetic photometry using a χ^2 minimization grid (Bayo et al. 2008). Given that VOSA has been updated to include a "Bayes analysis", which consists of doing the χ^2 minimization routine and then assigning relative probabilities to each model, finally normalizing them, we may ask the question, why is `ARIADNE` necessary? Does VOSA not accomplish the same outcomes as `ARIADNE`?

The VOSA procedure produces relative probabilities of each point in the selected model grids, but does not include priors for the analysis, which prove to be even more fundamental in SED analyses since the shape of the SED is not enough to constrain some of the parameters (e.g. log g and [Fe/H]). Another important difference is that VOSA evaluates the χ^2 only on the model grid points, while `ARIADNE` interpolates between those points to take full advantage of the exploratory nature of the nested sampling algorithm. Therefore, and most crucially, VOSA can not make use of the power of BMA when determining the stellar parameters, and indeed BMA is not an option within the VOSA package, nor any other current package that performs these types of analyses.

3.5 Model offsets and discussion

An important aspect of this work is highlighting the systematic offsets of the different models used, and to uncover possible biases present in them. To this end we studied the fractional residual distributions for the radius and temperature, and the residual distributions for the log g and [Fe/H]. Ideally the residuals should have a normal distribution with a mean of zero, however, we show in Figure 3.10 that the residual distributions are slightly asymmetrical and skewed, likely highlighting biases in the models, but without a significant offset. From Table 3.6 we see that none of the parameters show a significant offset in their residuals for both the full and truncated sample, but some of the individual models can over or underestimate measurements by as much as 32% for radius and 12% for temperature which translates to ~ 0.6 $R_\odot$ and 542 K, 0.54 dex and 0.8 dex for log g and [Fe/H] respectively.

The biases highlighted in Figure 3.10 arise from the different input physics and geometrical assumptions of each model, and while the BT-models have similar inputs and solar abundances, these subtle differences are particularly sensitive to cool, low-mass stars, likely a consequence of the grand differences between their internal structures when compared to that of the Sun[5]. A thorough review on current topics and shortcomings

[5]Many models are benchmarked against the Sun due to the deep understanding we have of the Solar structure.

Table 3.6: Individual model offsets for the sample of stars.

Model	mean	spread	-3σ	+3σ	max
			Radius		
Phoenix v2	-0.02	0.08	0.32	0.15	0.32
BT-Settl	0.01	0.07	0.22	0.17	0.22
BT-NextGen	-0.07	0.09	0.21	0.17	0.21
BT-Cond	-0.07	0.09	0.21	0.17	0.21
Castelli & Kurucz	0.00	0.06	0.19	0.14	0.19
Kurucz	0.01	0.07	0.29	0.15	0.30
			Temperature		
Phoenix v2	0.00	0.03	0.11	0.08	0.12
BT-Settl	-0.01	0.03	0.12	0.05	0.12
BT-NextGen	0.00	0.04	0.12	0.05	0.12
BT-Cond	0.00	0.04	0.12	0.05	0.12
Castelli & Kurucz	-0.00	0.03	0.08	0.05	0.08
Kurucz	-0.01	0.03	0.08	0.07	0.08
			log g		
Phoenix v2	0.01	0.09	0.34	0.49	0.54
BT-Settl	-0.01	0.09	0.38	0.31	0.39
BT-NextGen	-0.00	0.10	0.15	0.25	0.26
BT-Cond	-0.01	0.09	0.15	0.22	0.23
Castelli & Kurucz	0.00	0.10	0.48	0.32	0.49
Kurucz	-0.00	0.10	0.43	0.30	0.44
			[Fe/H]		
Phoenix v2	0.04	0.14	0.36	0.48	0.49
BT-Settl	0.01	0.15	0.50	0.79	0.80
BT-NextGen	0.06	0.35	0.51	0.77	0.77
BT-Cond	0.07	0.35	0.54	0.77	0.77
Castelli & Kurucz	0.03	0.12	0.47	0.38	0.49
Kurucz	0.01	0.15	0.61	0.62	0.67

in stellar modeling can be found in Section 6.3 of Torres et al. (2010) and the discussions found in Jofré et al. (2014, 2015); Heiter et al. (2015); Jofré et al. (2017).

The lack of a significant offset in the averaged residual distribution is evidence of the accuracy ARIADNE achieves with the radius, temperature and log g. The small spread found in the averaged residual distributions show the precision attainable by this method. Indeed, some of the posterior widths our code attains is at the level of, or better than, those directly measured from interferometry. Therefore, the widespread use of ARIADNE for obtaining stellar parameters will allow us to calculate more accurate and precise planetary masses and radii, further constraining planetary formation, evolution and composition models.

In Tayar et al. (2020), while not studying stellar atmosphere grids directly, they investigate the uncertainties of stellar fundamental properties for FGK stars. They advocate for additional uncertainties added in quadrature to the formal uncertainties for stars, due in some part to model uncertainties. ARIADNE circumvents part of this problem, since we include this error as part of the modeling procedure within the BMA. What Tayar et al. did not consider, is the constraints from the data themselves, since the precision clearly allows models to be favored over other models, in many cases. Therefore, by properly weighting each model given the constraints from the data, this systematic variability can be partially overcome. We note, however, that due to the inherent complexity of stellar atmosphere modeling, quantifying how much of this systematic variability is overcome is a difficult task.

3.6 Conclusions

We present ARIADNE, a public and open-source Python package to perform automatic stellar SED fitting using Bayesian Model Averaging to calculate stellar parameters with precision and accuracy comparable to interferometric observations. We find a fractional RMS of 0.001 ± 0.070 and a mean precision of 2.1% for the averaging method and 0.000 ± 0.069 and 4.3% for the sampling method when comparing the results of our set of 135 stars to those measured by interferometry. Considering an expected scatter in interferometric precision of 5% (Stassun et al. 2017), we conclude that the scatter found when comparing ARIADNE with interferometric measurements can be mostly explained by the intrinsic noise within these measurements. The code is particularly useful for calculating stellar radius, effective temperature with uncertainties lower than $\pm$100 K, and log g, which can then be used to calculate mass either through Equation 3.8 or using isochrone interpolation. Accurate metallicity values can be attained when using priors drawn from other methods, such as EW calculations or spectral synthesis, though these values might not be as precise as when using these other methods. These are all key parameters for characterizing planetary bulk parameters in the age of high precision and short-cadence ground- and space-based photometry.

We highlighted systematic differences between the employed models, and found that while the different assumed input physics and geometries give rise to non-negligible biases, these biases are mostly overcome when properly averaging the models with their respective Bayesian evidences. This does not apply to the isochrone masses ARIADNE provides, but the same methodology can be applied to different isochrone models to increase the precision of estimated masses and ages. The M dwarfs seem to pose something of a problem also, showing a rising trend in radii when compared to interferometrically measured values, but the effect is small, well within the 5% interferometric scatter. We finally encourage the use of ARIADNE to calculate stellar bulk properties, along with continued development of the methodologies presented here within the framework of stellar and exoplanetary science.

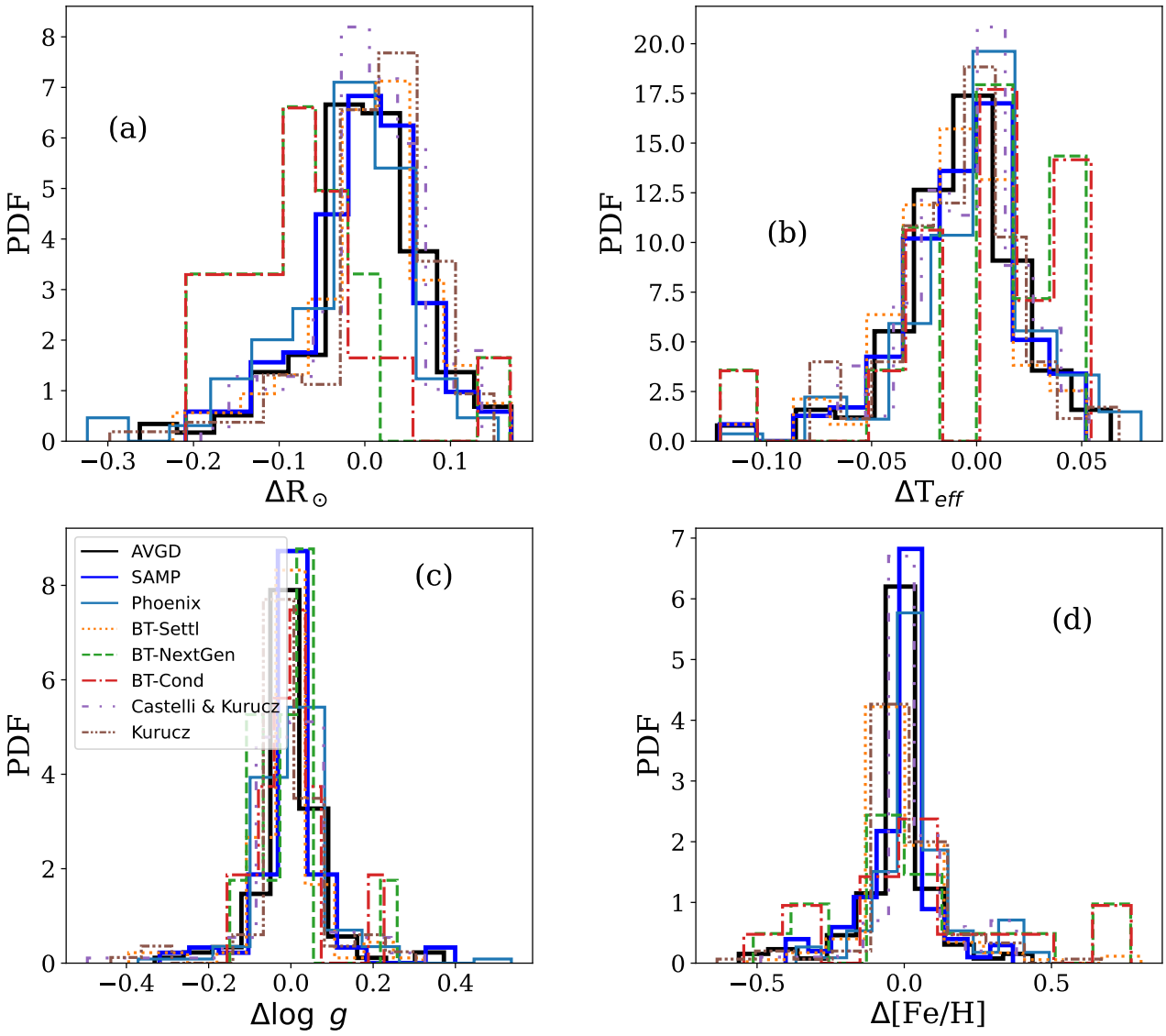

Figure 3.10: Offset distributions for each model for (a) stellar radius, (b) effective temperature, (c) log g and (d) [Fe/H]. The averaged distribution is plotted to show how it decreases individual model biases, except in the case of giant stars where the models consistently overestimate radius and temperature.

Chapter 4

A dense mini-Neptune orbiting the bright young star HD 18599

Based on the results published in Vines, J. I., et al., *A dense mini-Neptune orbiting the bright young star HD 18599*, 2023, MNRAS, 518, 2627.

Very little is known about the young planet population because the detection of small planets orbiting young stars is obscured by the effects of stellar activity and fast rotation which mask planets within radial velocity and transit data sets. The few planets that have been discovered in young clusters generally orbit stars too faint for any detailed follow-up analysis. Here we present the characterization of a new mini-Neptune planet orbiting the bright (V=9) and nearby K2 dwarf HD 18599. The planet candidate was originally detected in *TESS* light curves from Sectors 2, 3, 29, and 30, with an orbital period of 4.138 days. We then used HARPS and FEROS radial velocities, to find the companion mass to be 25.5±4.6 $M_{\oplus}$. When we combine this with the measured radius from *TESS* of 2.70±0.05 $R_{\oplus}$, we find a high planetary density of 7.1±1.4 g cm^{-3}. The planet exists on the edge of the Neptune Desert and is the first young planet (300 Myr) of its type to inhabit this region. Structure models argue for a bulk composition to consist of 23% H_2O and 77% Rock and Iron. Future follow-up with large ground- and space-based telescopes can enable us to begin to understand in detail the characteristics of young Neptunes in the galaxy.

4.1 Observations

This candidate was first detected through the observation of 16 transit events by the *TESS* mission, yielding a period of 4.137 days from an `EXOFASTv2` (Eastman et al. 2019) analysis listed on the Exoplanet Follow-up Observing Program (ExoFOP)[1]. After scrutinizing the processed light curve publicly available at MAST[2], and given that the star is bright, we selected this candidate as a high-priority target to be observed in a HARPS campaign starting in 2018. Upon examination of archival data, we found the star was already observed with sparse sampling between 2014 and 2017. Later, additional observations with FEROS were planned to help constrain the orbital and physical parameters of the planet. Finally, Minerva-Australis observations to help validate the candidate were also acquired. The following sections describe the observations and data acquisition of HD 18599 in detail.

[1]https://exofop.ipac.caltech.edu/tess/target.php?id=207141131
[2]https://mast.stsci.edu/portal/Mashup/Clients/Mast/Portal.html

Table 4.1: Detrended *TESS* photometry for HD 18599. The full table is available in a machine-readable format from the online journal. A portion is shown here for guidance.

Time (BJD-2450000)	Flux (normalised)	Flux error
8354.11157	0.9989	0.0004
8354.11296	0.9992	0.0004
8354.11574	0.9993	0.0004
8354.11712	0.9994	0.0004
8354.11851	0.9994	0.0004
8354.11990	0.9999	0.0004
8354.12129	0.9990	0.0004
8354.12268	0.9993	0.0004
8354.12407	0.9993	0.0004
8354.12546	0.9995	0.0004
⋮	⋮	⋮

4.1.1 Photometry

WASP Photometry

WASP-South, an array of 8 wide-field cameras, was the Southern station of the WASP transit-search project (Pollacco et al. 2006b). It observed the field of HD 18599 in 2010 and 2011, when equipped with 200-mm, f/1.8 lenses, and then in 2012, 2013, and 2014, equipped with 85-mm, f/1.2 lenses. Observations were made on each clear night over an observing season of 175 nights per year, accumulating 86 000 photometric data points with a typical 15-minute cadence. At V = 9, HD 18599 is by far the brightest star in the 48-arcsec extraction aperture of the 200-mm data. A V = 10.9 star, 88 arcsecs away, is, however, within the 113-arcsec extraction aperture of the 85-mm data, and will cause a $\sim$ 10% dilution. We studied the periodogram of the WASP light curves in Section 4.2.2 to find the rotation period of HD 18599 in order to properly detrend the *TESS* data.

TESS Photometry

HD 18599 was observed by *TESS* in Sectors 2, 3, 29, and 30 with Camera 3 in short-cadence mode (2 minutes), starting from the 22nd of August 2018 to the 22nd of September 2020, producing a total time baseline of 2 years, during which 21 transit features were observed. Observations were analyzed and processed with the Science Processing Operations Center (SPOC, Jenkins et al. 2016a) by NASA Ames Research Center, after which it was promoted to TOI-179.

We extracted the Simple Aperture Photometry (SAP) and the Presearch Data Conditioning (PDC, Jenkins et al. 2016a) light curves that were produced by the SPOC pipeline, removed data points flagged as low quality, and finally, we normalized the light curve. We note that even after this procedure, stellar variability still remains in the light curve and must be taken care of to determine the most optimal companion parameters. In the end, the SAP and PDCSAP light curves look almost identical, but we use the latter throughout the paper in any case.

Finally, we applied Gaussian Processes (GP) to detrend and remove the stellar variability signal in the light curve (see Section 4.2.3 and Figure 4.4). The detrended light curve can be found in Table 4.1.

4.1.2 Radial Velocities

We observed HD 18599 with three fiber-fed high precision échelle spectrographs: High-Accuray Radial velocity Planet Searcher (HARPS, Pepe et al. 2002), FEROS, and Minerva-Australis to obtain high-precision radial velocities (RVs) and constrain the planetary mass.

HARPS

HARPS is mounted on the ESO 3.6-m Telescope at the La Silla observatory in Northern Chile, and has a spectral resolution of R = 120 000. Observations include data acquired prior to the fibre updates we refer to as "pre" (PI: Lagrange). Data acquired after the fiber updates in 2015 (PI: Lagrange, Díaz, Berdiñas, Jordán, Brahm, and Benatti)[3] is labeled as "post". In total we obtained 103 observations from HARPS. HARPS observations are processed on site using the standard ESO Data Reduction Software (DRS). The DRS pipeline data products were then reprocessed independently using the HARPS-TERRA code (Anglada-Escudé & Butler 2012). HARPS-TERRA creates a high signal-to-noise template from the individual observations. Then, each observation is matched using a χ^2 process relative to this template producing an RV for each observed spectrum. The code also computes stellar activity indices for the Calcium II H & K lines (λ_H = 3933.664 Å, λ_K = 3968.470 Å), which are not available from the DRS-reduced spectra. For the derivation of S-indices the code integrates the flux in these lines and compares with the flux on adjacent chunks in the continuum, following the procedure described in Lovis et al. (2011). S-indices from HARPS-TERRA are calibrated to the Mt. Wilson system (S_{MW}) and they can be used as a direct proxy to monitor the chromospheric activity of the star. Additional activity indices such as the full-width at half-maximum of the cross-correlation function (CCF FWHM) and the bisector inverse slope (BIS) are taken directly from the fits headers of the DRS-reduced data products. Uncertainties in BIS are taken as twice the RV errors and the CCF FWHM uncertainties are 2.35 times the RV errors (Zechmeister et al. 2018).

FEROS

The FEROS spectrograph is mounted on the 2.2-m MPG/ESO telescope also at La Silla observatory and has a spectral resolution of R=48 000 (Kaufer et al. 1999). Nine observations were made during September 10 and 19 under program 0103.A-9004(A) (PI: Vines) which were reduced with the `CERES` pipeline (Brahm et al. 2017). After the reduction, `CERES` calculates RVs through the CCF method. We used a binary K5 mask for each epoch and fit a double Gaussian to the CCF in order to find the RV. A double Gaussian was used in order to account for scattered moonlight contamination. In addition to the RVs, `CERES` also provides the CCF FWHM and the BIS as activity indices. The uncertainties in BIS are calculated internally by `CERES` while the uncertainties of the CCF FWHM are calculated by dividing the standard deviation of the Gaussian fitted to the CCF, and dividing by the S/N at 5130 Å, a procedure analogous to the RV uncertainty calculation done by `CERES`. S-indices index are computed from each 1D spectra after correcting to rest-frame following the procedure outlined by Jenkins et al. (2008) using the `Ceres-plusplus`[4] code.

Minerva-Australis

Minerva-Australis is an array of four PlaneWave CDK700 telescopes located in Queensland, Australia, fully dedicated to the precise RV follow-up of *TESS* candidates (e.g. Jordán et al. 2020b; Addison et al. 2021a,b). The four telescopes can be simultaneously fiber-fed to a single KiwiSpec R4-100 high-resolution (R=80,000) spectrograph (Barnes et al. 2012; Addison et al. 2019).

[3]ESO programs 192.C-0224, 0102.C-0525, 0102.D-0483, 0101.C-0510, 0102.C-0451, 0103.C-0759
[4]https://github.com/jvines/Ceres-plusplus

HD 18599 was monitored by Minerva-Australis in its early commissioning period, with a single telescope between 2019 Jan 6 and 2019 Jan 29. Exposure times were 30 minutes, with some nights receiving two or three consecutive exposures. We obtained a total of 31 observations, with a mean S/N of 23±5 per pixel. RVs are derived for each telescope by cross-correlation, where the template being matched is the mean spectrum of each telescope. The instrumental variations are corrected by using simultaneous Thorium-Argon arc lamp observations.

We show the RVs with the activity indicators in Table 4.2.

Table 4.2: RVs and Activity Indices for HD 18599

BJD (-2450000)	RV ($m\,s^{-1}$)	RV err ($m\,s^{-1}$)	BIS ($m\,s^{-1}$)	BIS err ($m\,s^{-1}$)	S_{MW} (dex)	S_{MW} err (dex)	FWHM ($km\,s^{-1}$)	FWHM err ($km\,s^{-1}$)	instrument
6980.6959	12.7646	1.2472	5.2533	0.8099	-0.0053	0.0028	-0.0356	0.0029	HARPS_pre
6980.7020	11.4832	1.2733	5.8890	0.8002	-0.0034	0.0028	-0.0337	0.0010	HARPS_pre
6982.6788	16.0365	1.3771	8.2058	1.0231	0.0031	0.0033	0.0113	0.0032	HARPS_pre
6982.6849	14.4035	1.9666	10.6088	1.0709	0.0214	0.0034	0.0067	0.0046	HARPS_pre
6987.6309	-18.5854	1.9749	55.0689	1.1134	-0.0055	0.0035	0.0504	0.0046	HARPS_pre
6987.6371	-16.9837	1.8491	52.7322	1.1613	0.0077	0.0036	0.0564	0.0043	HARPS_pre
6988.6928	-19.1186	1.2100	44.4527	0.8029	-0.0180	0.0026	-0.0556	0.0028	HARPS_pre
⋮	⋮	⋮	⋮	⋮	⋮	⋮	⋮	⋮	⋮

4.2 Analysis

4.2.1 Stellar Properties

SPECIES

We analysed the 1D stacked HARPS spectra using SPECIES (Soto & Jenkins 2018; Soto et al. 2021). SPECIES is an automated code to derive stellar parameters for large samples of stars, using high resolution echelle spectra. It makes use of equivalent widths from a number of neutral and ionized iron lines (measured with EWComputation, Soto et al. 2021) to derive the atmospheric parameters (temperature, metallicity, surface gravity, and microturbulence). Together with ATLAS9 model atmospheres (Castelli & Kurucz 2003), it solves the radiative transfer and hydrostatic equilibrium equations using MOOG (Sneden 1973), imposing local thermodynamic equilibrium (LTE) conditions, as well as excitation and ionization equilibrium. The correct atmospheric parameters are found when the abundance for ionized and neutral iron are the same, the obtained iron abundance is the same as the one used to create the model atmosphere, and there is no correlation between the neutral iron abundances with the excitation potential, and with the reduced equivalent widths (W/λ). Finally, rotational and macro turbulent velocities were derived using spectral line fitting and analytic relations, respectively. SPECIES finds an effective temperature of 5109±50 K, a log g of 4.41±0.07 dex, a [Fe/H] of -0.01±0.05 dex and a vsini of 5.2±0.2 km s^{-1}.

ARIADNE

We used the temperature, log g and [Fe/H] found by SPECIES as Gaussian priors on a Spectral Energy Distribution (SED) analysis performed with ARIADNE[5] (Vines & Jenkins 2022) to find the final set of bulk stellar parameters. ARIADNE is a publicly available python tool designed to fit catalog photometry to different stellar atmosphere models grids, Phoenix V2 (Husser et al. 2013); BT-Settl, BT-Cond, BT-NextGen (Hauschildt et al. 1999; Allard et al. 2012), Castelli & Kurucz (2003) and Kurucz (1993); which have been convolved with the following filter response functions:

- Johnson UBV
- Tycho-2 BtVt
- 2MASS JHK_s
- SDSS *ugriz*
- Gaia DR2v2 G, RP and BP
- GALEX NUV and FUV
- TESS

The SEDs are modeled by interpolating the model grids in T_{eff}-log g-[Fe/H] space, scaling the synthetic flux by $(R/D)^2$ and accounting for interstellar extinction through the extinction in the V band, A_V. Additionally, we include an excess noise parameter for every photometric observation in order to account for underestimated uncertainties. ARIADNE samples the posterior space using the dynesty (Speagle 2020) implementation of (dynamic) nested sampling (Higson et al. 2019). Nested Sampling (Skilling 2004, 2006) algorithms are designed to estimate the Bayesian evidence of a model producing posterior distributions as a by-product.

[5]https://github.com/jvines/astroARIADNE

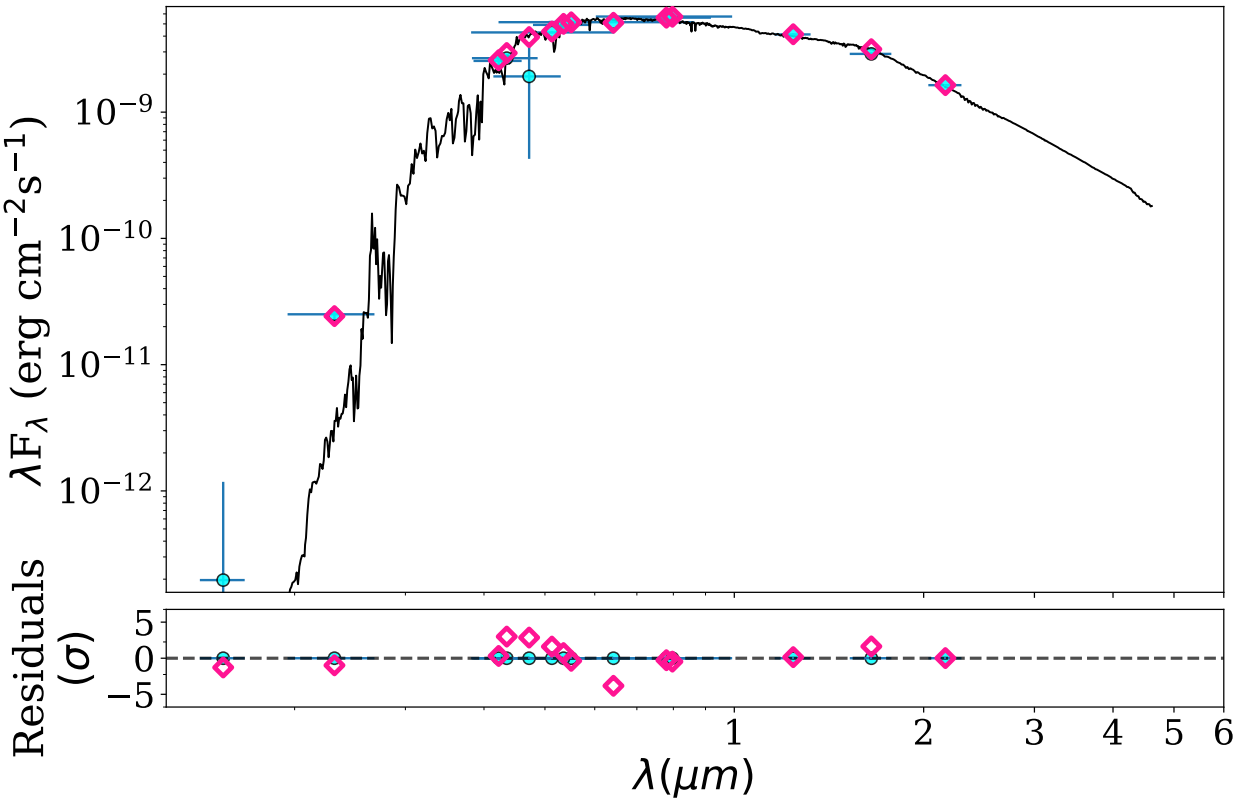

Figure 4.1: The best fitting Castelli & Kurucz SED (black line) for HD 18599 based on the photometric data (cyan points) presented in Table 4.3 is shown in the top panel. Horizontal errorbars show the bandpass width. The pink diamonds show the synthetic magnitudes at the wavelengths of the photometric data. The lower panel shows the residuals to the best fit model.

We modeled the SED with four models, Phoenix V2, BT-Settl, Castelli & Kurucz (2003) and Kurucz (1993), and finally averaged the posterior parameters from each model, weighting them by their respective relative probability that was computed from their Bayesian evidence estimates, resulting in precise parameters that take into account the different micro-physics and geometry of the different models.

Additional priors for distance, radius, and A_v were drawn from the Bailer-Jones distance estimate from Gaia DR2 (Bailer-Jones et al. 2018), a uniform prior from 0.5 to 20 $R_\odot$ and a uniform prior from 0 to 0.038, the maximum line-of-sight extinction from the re-calibrated SFD galactic dust map (Schlegel et al. 1998; Schlafly & Finkbeiner 2011).

In Figure 4.1 we show the SED for HD 18599 and in Table 4.3 we report the relevant observational properties with our derived properties, along with the method used.

HD 18599 is previously known to be a young field star based on previous studies (Grandjean et al. 2020, 2021). In a more recent study, de Leon et al. (submitted) employed various methods to estimate the age of HD 18599. In that paper, we measured an equivalent width (EW) of 42±2mÅ for Li I λ6708. This measurement generally agrees with those found in stars in Hyades and Praesepe corresponding to an age of ~800 Myr. We also estimated the stellar age by taking advantage of the observed chromospheric activity together with empirical age-activity-rotation relations. In particular, we used the chromospheric activity indicator, $\log R'_{HK} = -4.41 \pm 0.02$ from Boro Saikia et al. 2018 which predicts an age of 0.30 ± 0.05 Gyr. Whilst this star

is an X-ray source based on detection from ROSAT, the X-ray strength is weak ($\log Lx/Lbol = -4.64 \pm 0.25$) which corresponds to $1-\sigma$ age range from X-ray of 475^{+734}_{-305} Myr.

HD 18599 exhibits significant spot-modulated rotational signals in the four sectors of TESS observations. Using a periodogram analysis, we measured the rotation period of HD 18599 for each of these sectors of observations, finding that it has a mean rotation period of 8.71 ± 0.31 d. We compute a gyrochronological age estimates of 386 Myr, with $3-\sigma$ range of 261-589 Myr based on Mamajek & Hillenbrand 2008 model, whereas we compute an age of 247 Myr, with 3-σ range of 185-329 Myr based on Barnes 2007 model. We can further corroborate the activity-based age estimate by also using empirical relations to predict the stellar rotation period from the activity. For example, the empirical relation between R'_{HK} and rotation period from Mamajek & Hillenbrand 2008 predicts a rotation period for this star of 9.7 ± 1.3 d, which is compatible with the rotation periods above as well as with the rotation period of 8.69 d reported by KELT. For simplicity, we adopt a median age of 300 Myr throughout the rest of the paper.

An asteroseismology study of HD 18599 was also performed, finding that the active nature of the star produces photometric variability much larger than the amplitude of the expected oscillation modes, making the visual detection of the oscillations very tough. The details of the analysis and the results can be found in Samadi-Ghadim et al. (2022 in prep.).

4.2.2 Stellar Rotation

From *Kepler* data it has been shown that the analysis of photometric time series can yield good estimates of the stellar rotation period (see, e.g. McQuillan et al. 2013; Giles et al. 2017). Rotationally modulated spots on the stellar surface can produce a periodic signal that can be detected in the photometry since these spots are regions of diminished flux. Additionally, rotational modulations can be a source of false-positive exoplanets signatures, for which the *TESS* photometry, combined with ground-based data sources, can serve as a powerful diagnostic for assessing the properties of known exoplanets (Kane et al. 2021; Simpson et al. 2022).

We searched each season's WASP light curve for rotational modulations using the methods presented in Maxted et al. (2011). There is a clear and persistent modulation seen in 4 of the five seasons (Figure 4.2). The mean period is 8.74 ± 0.06 d, the amplitude ranges from 6 to 10 mmag, and the false-alarm likelihoods are less than 10^{-3}. In 2013 the modulation is marginally present but with a much lower amplitude of 1–2 mmag.

We also computed the Autocorrelation Function (ACF, McQuillan et al. 2013) for each *TESS* light curve, using the PCDSAP corrected data provided by the SPOC in order to find a possible value for the stellar rotation period. We follow the procedure described in Soto & Jenkins (2018), where we model the ACF as an underdamped Simple Harmonic Oscillator (uSHO) (López-Morales et al. 2016). We define

$$y(t) = \mathrm{e}^{-t/\tau_{\mathrm{AR}}} \left[A \cos\left(\frac{2\pi t}{P_{\mathrm{rot}}}\right) + B \cos\left(\frac{4\pi t}{P_{\mathrm{rot}}}\right) \right] + y_0 \tag{4.1}$$

Where τ_{AR} is the correlation time scale and P_{rot} is the rotation period.

We estimated P_{rot} using the Edelson & Krolik method (Edelson & Krolik 1988) implemented in `astroML` Python package via a least squares fitting process (VanderPlas 2018). Results are tabulated in Table 4.4.

Table 4.3: Stellar Properties for HD 18599

Property	Value	Source
Astrometric Properties		
R.A.	$02^h57^m02^s8835$	Gaia
Dec	$-56°11'30\farcs7297$	Gaia
2MASS I.D.	J02570294-5611314	2MASS
TIC	207141131	*TESS*
Gaia DR2 I.D.	4728513943538448512	Gaia
$\mu_{\rm R.A.}$ (mas y^{-1})	-36.676±0.042	Gaia
$\mu_{\rm Dec.}$ (mas y^{-1})	50.599±0.045	Gaia
ϖ (mas)	25.9011±0.0244	Gaia
Photometric Properties		
V (mag)	8.968±0.012	APASS
B (mag)	10.015±0.004	APASS
g (mag)	10.20±0.05	APASS
V_T (mag)	9.084±0.016	Tycho2
B_T (mag)	10.015±0.004	Tycho2
G (mag)	8.7312±0.0007	Gaia
RP (mag)	8.1384±0.0019	Gaia
BP (mag)	9.2113±0.0020	Gaia
TESS (mag)	8.1796±0.0060	*TESS*
J (mag)	7.428±0.018	2MASS
H (mag)	7.029±0.015	2MASS
Ks (mag)	6.883±0.020	2MASS
NUV (mag)	15.684±0.012	GALEX
FUV (mag)	21.389±0.264	GALEX
Derived Properties		
$T_{\rm eff}$ (K)	5083±23	`ARIADNE`
[Fe/H]	-0.05±0.04	`ARIADNE`
vsini (km s^{-1})	5.2±0.2	`SPECIES`
log g	4.40±0.07	`ARIADNE`
$M_s(M_\odot)$	$0.807^{+0.019}_{-0.007}$	`ARIADNE`
$R_s(R_\odot)$	$0.798^{+0.006}_{-0.007}$	`ARIADNE`
ρ (g cm^{-3})	$2.241^{+0.081}_{-0.077}$	This work
Age (Myr)	300	Gyrochronology
Distance (pc)	$38.585^{+0.110}_{-0.150}$	`ARIADNE`
Av (mag)	$0.030^{+0.002}_{-0.014}$	`ARIADNE`
$P_{\rm rot}$	8.74±0.05	This work

2MASS (Skrutskie et al. 2006); UCAC4 (Zacharias et al. 2013);
APASS (Henden & Munari 2014); WISE (Wright et al. 2010);
Gaia (Gaia Collaboration et al. 2016, 2018); GALEX (Bianchi et al. 2011b);
TESS (Stassun et al. 2018)
$q_{1,2}$ are the Kipping Limb Darkening parameters.

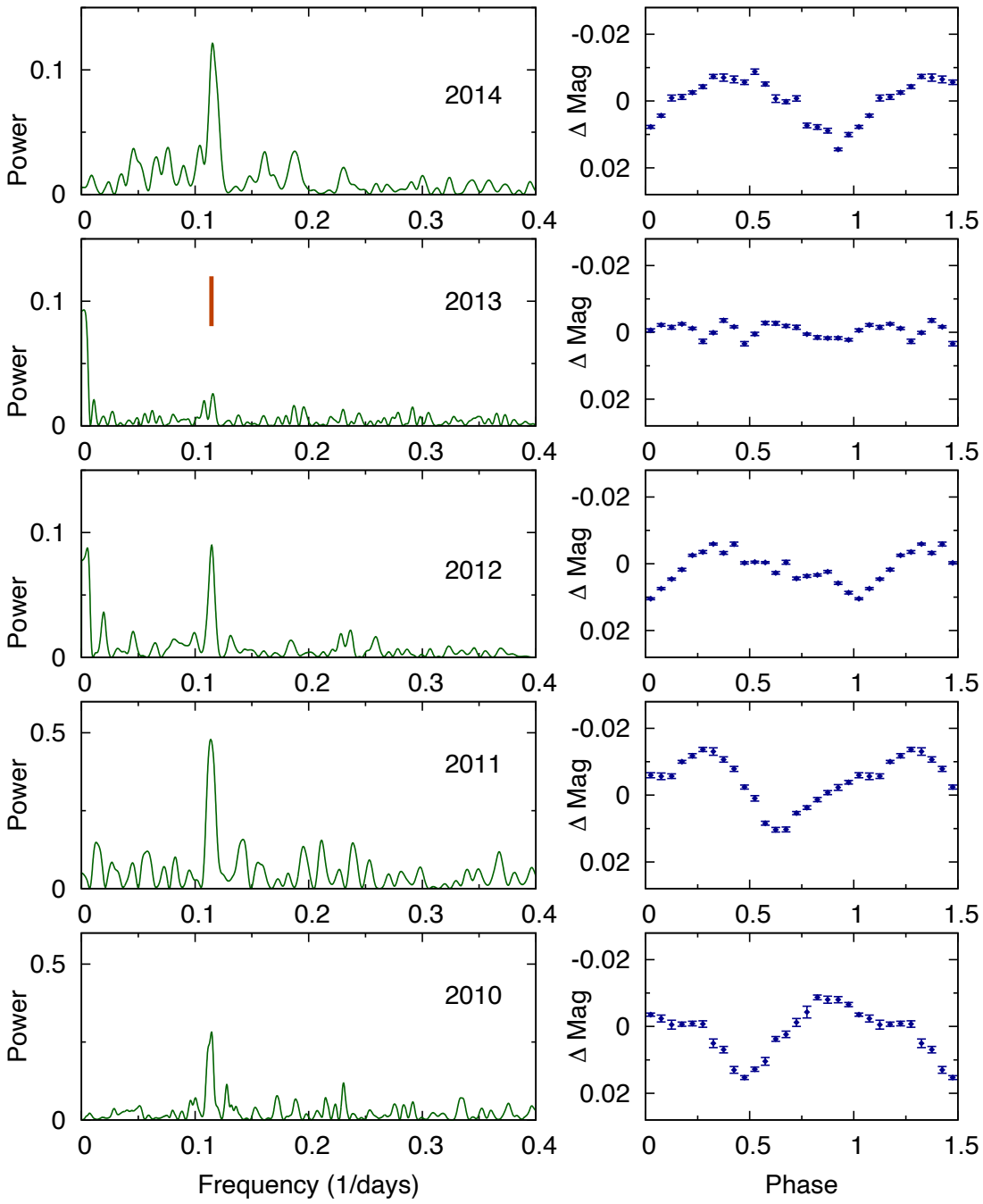

Figure 4.2: Periodograms of the WASP-South data for HD 18599 (left) along with the modulation profiles from folding the data (right). The red line is at a period of 8.74 days.

Table 4.4: ACF results from the *TESS* light curve.

Sector	$P_{\rm rot}$ (days)	$P_{\rm rot}$ err (days)
2	4.522	0.001
3	4.526	0.002
29	8.605	0.281
30	8.791	0.110

The rotation period from the first two sectors are consistent with each other and consistent with being an alias from the rotation period derived from WASP data. This is further confirmed with the estimated rotation period of the latter sectors being consistent with the one derived by WASP as well.

We ran the Generalized Lomb-Scargle periodogram (GLS, Zechmeister & Kürster 2009) in a grid of 50,000 trial frequencies ranging from one day to two years in period space on the *TESS* data to find the possible sinusoidal signals. We show these in Figure 4.3 where the dashed line represent the 0.1, 5, and 10% false-alarm probabilities (FAP), but they happen to coincide due to the amplitude of the oscillations. The top panel of Figure 4.3 shows the GLS periodogram of sectors 2 and 3, where the two most strong signals correspond to 4.41 and 8.78 days. The middle panel shows the periodogram of sectors 29 and 30 where the most dominant signal is 8.76 days, the second most strong signal is 22.89 days. We show a third signal, which while not as significant, corresponds to the same period as the most strong signal found in sectors 2 and 3, 4.40 days. The bottom panel shows the periodogram of the combined three sectors where the most dominant signal is the 8.77 day one and the 4.40 day signal is the second most significant one.

Using `Juliet`[6] (Espinoza et al. 2019) and `MultiNest` via the Python wrapper `pyMultinest` (Feroz et al. 2009; Buchner et al. 2014), we fit a Gaussian Process (GP) using a Simple Harmonic Oscillator (SHO) kernel from *celerite* (Foreman-Mackey et al. 2017b) to the out-of-transit *TESS* light curve in order to remove the stellar activity signal present. We used the rotation period derived from WASP as a Gaussian prior for the characteristic frequency of the SHO. We found the best fitting parameters to be $S_0 = 0.0008 \pm 0.0001$, $Q = 0.11 \pm 0.01$ and $\omega_0 = 0.719 \pm 0.004$. A quality factor less than $1/2$ means the system is overdamped and thus there is no oscillation aside from the rotation of the star, which is captured by the GP as seen in the top panel of Figure 4.4. These parameters translate to a rotation period of 8.74 ± 0.05 days. The top panel of Figure 4.4 shows the raw light curve with the best fitting GP, and the bottom panel shows the detrended light curve, with the red vertical lines highlighting the transit features.

4.2.3 Activity Indices

We searched for correlations between the RVs and the activity indices: (BIS), CCF FWHM and S_{MW}, and we found a strong anticorrelation between the BIS and RVs, no correlation for the CCF FWHM, and a weak correlation for S_{MW}, quantified by the Pearson r correlation coefficients: -0.62, 0.05, and 0.49, respectively. We show our thresholds for correlation in Table 4.5.

In addition to the Pearson r coefficients, we fit a linear model to each of the correlations using Markov Chain Monte Carlo (MCMC) through `emcee` (Foreman-Mackey et al. 2013) to probe the posterior parameter space. We employed a gaussian likelihood that takes into account uncertainties in both axes. We show the best fitting model parameters in Table 4.6 and the correlations in Figure 4.5. Given that the slopes of the

[6]https://juliet.readthedocs.io/en/latest/

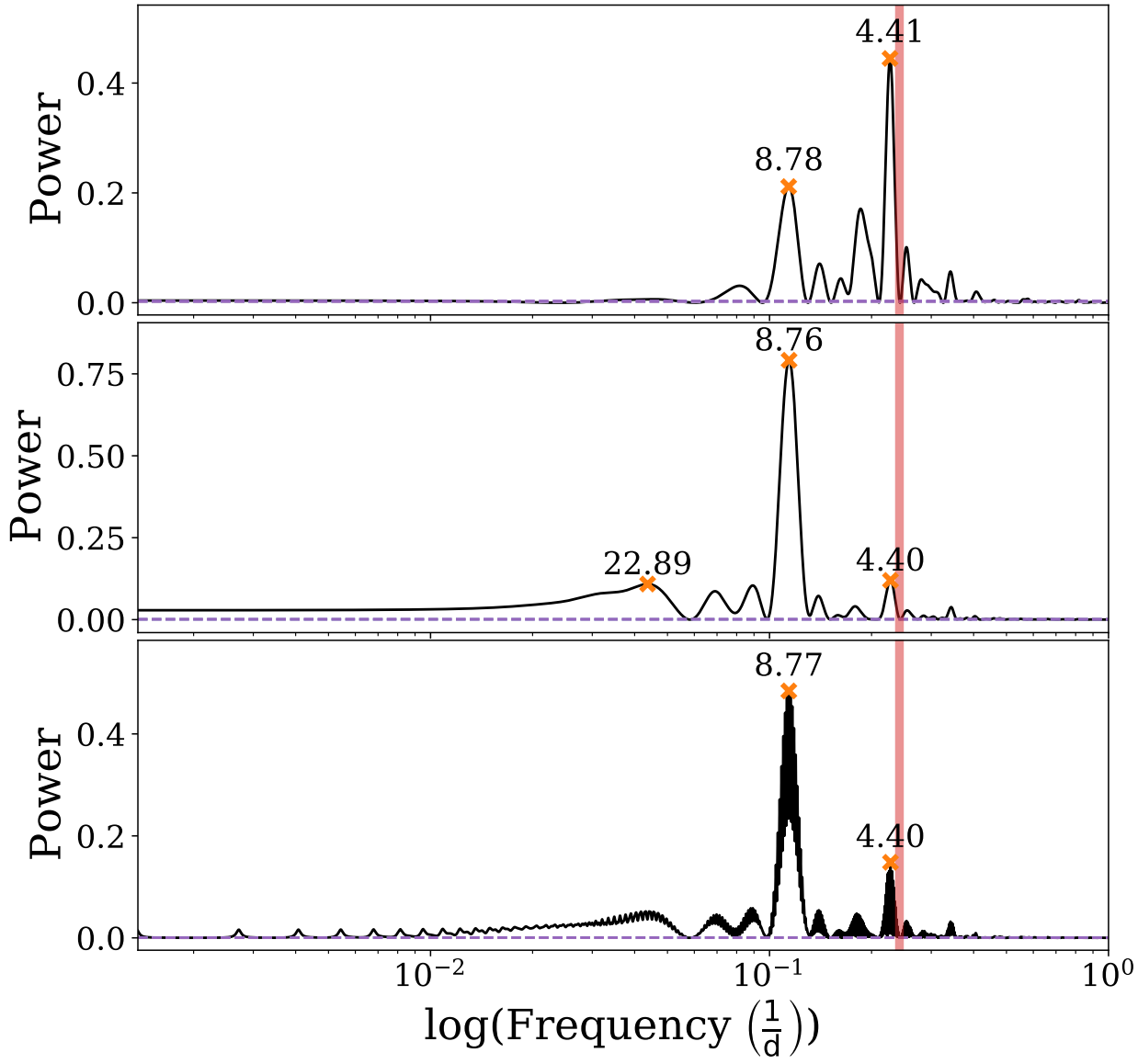

Figure 4.3: From top to bottom: the GLS periodogram for the *TESS* light curves from sectors 2 and 3 (top), sector 29 and 30 (middle), and the three sectors combined (bottom). The orange crosses show the most significant peaks with their respective periods labeled on top. The vertical red line marks the 4.1375-day planet candidate from the *TESS* data. The dashed horizontal line are the false alarm probabilities for 0.1, 5 and 10%, they turn out to be superimposed.

Table 4.5: Adopted thresholds for the Pearson r correlation coefficient. We only show the positive values, but the same thresholds apply for their negative counterparts.

r	Strength
0.00 to 0.19	Very weak
0.20 to 0.39	Weak
0.40 to 0.59	Moderate
0.60 to 0.79	Strong
0.80 to 1.00	Very strong

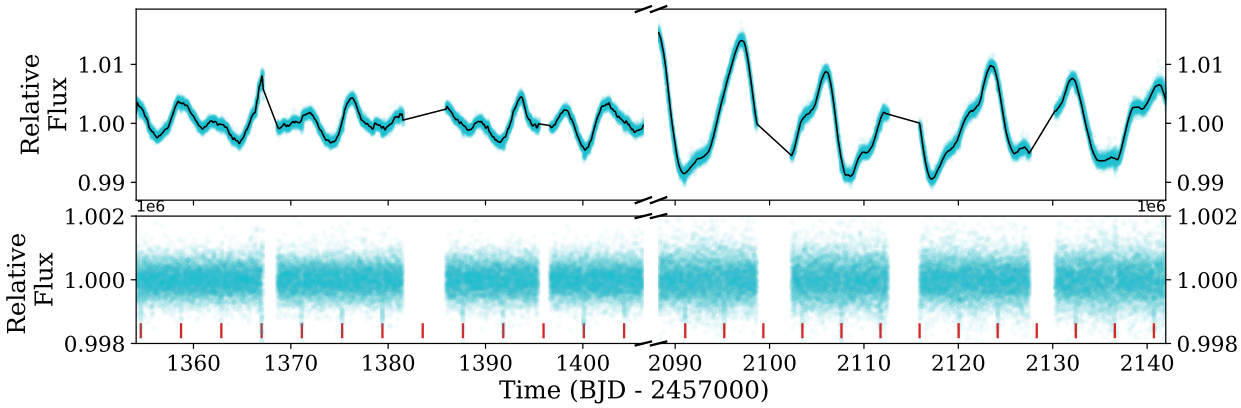

Figure 4.4: The normalized *TESS* light curve including data from the three sectors, with the best fitting SHO kernel GP (black line). The bottom panel shows the detrended light curve in ppm. The vertical red lines show the transit features.

Table 4.6: Intercept and slopes of the best fitting linear models of each correlation.

Correlation	Slope	Intercept
BIS	$-0.836^{+0.088}_{-0.096}$	$17.302^{+2.222}_{-2.254}$
CCF FWHM	$0.000^{+0.005}_{-0.005}$	$-0.032^{+0.161}_{-0.162}$
S_{MW}	$0.001^{+0.005}_{-0.005}$	$-0.001^{+0.162}_{-0.162}$

CCF FWHM and S_{MW} are statistically consistent with zero, we conclude that the only significant correlation is the BIS.

Using the GLS periodogram we searched for periodicities in the RVs, BIS, S_{MW} indices, and CCF FWHM. Signals at 1, 0.5, and 0.3 days arise from the window function, as well as a broad signal around 800 to 1000 days which reappears in the RVs, S_{MW}, and the FWHM. The BIS shows a peak at 4.40 days which coincides with the Prot alias from *TESS* and WASP. Given that the period candidate is very close to the rotation period alias tracked by the BIS, a straightforward decorrelation is not possible since it would also inadvertently remove the candidate signal from the data, therefore, we chose to model the raw RVs but with the incorporation of different noise and activity models.

4.2.4 Global Modeling

We jointly modeled the detrended *TESS* data with the HARPS and FEROS RVs, in order to obtain the mass, radius, and orbital parameters of TOI-179 b, with `EMPEROR.T`, an upgraded version of `EMPEROR` (Pena & Jenkins in prep) that handles both RVs and light curves.

`EMPEROR` models transits with the transit light curve calculation code `PyTransit` (Parviainen 2015) using the quadratic limb darkening law from Mandel & Agol (2002), along with the triangular limb-darkening parametrization proposed by Kipping (2016). The transit model also includes an offset and white noise term, as well as a dilution factor (Espinoza et al. 2019), which we fixed to unity due to the expected dilution being $< 1\%$ (de Leon et al. 2022, in prep.). RVs are modeled with the Keplerian model including a velocity offset γ and an instrumental white noise parameter σ for each instrument and a first order acceleration term. `EMPEROR` implements instrumental q order autoregressive and p order moving average models (AR(q)MA(p);

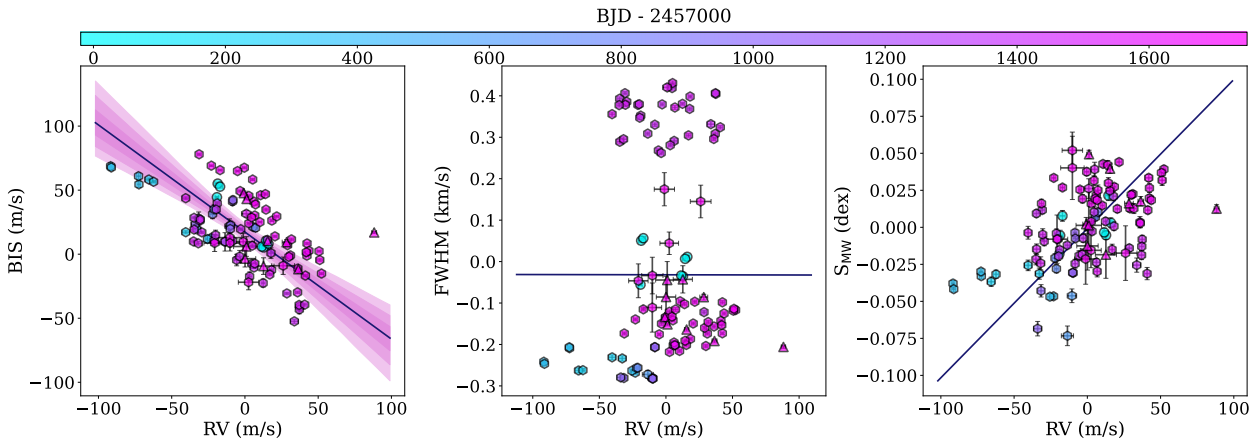

Figure 4.5: From left to right: The bisector velocity span with 1, 2, and 3 sigma confidence regions, FWHM, and S-index correlation with the RVs after subtracting their respective mean values. HARPS_pre, HARPS_post, and FEROS are denoted by circles, hexagons, and triangles respectively. Each observation is color-coded by its BJD timestamp. In all cases, the blue line corresponds to the best-fitting linear model. Confidence regions were not added for the FWHM and S index panels due to them being unconstrained.

Tuomi et al. 2013b) as a correlated noise model that deals with noise from, for example, stellar variability. Additionally, `EMPEROR` has incorporated a linear stellar activity correlation model following the description in Anglada-Escudé et al. (2016). `EMPEROR` also allows for the modeling of the stellar density, which has been shown to improve parameter estimation as it deals with the degeneracy between the radius ratio and the impact parameter (Sandford et al. 2019; Vines et al. 2019). The algorithm assumes a Gaussian generative model and thus both the RV jitter and photometric white noise are added in quadrature to their respective observational uncertainties. The described model is given by

$$f_{rv,\mathrm{i,ins}} = k(t_\mathrm{i}) + a_{\mathrm{i,ins}}(q) + m_{\mathrm{i,ins}}(p) + A_{\mathrm{i,ins}} + \gamma_\mathrm{ins} + \dot{\gamma}_\mathrm{ins} + \sigma_{\mathrm{i,ins}} \tag{4.2}$$

$$ar_{\mathrm{i,ins}}(q) = \sum_{j=1}^{q} \phi_{j,\mathrm{ins}} \exp\left(\frac{t_{\mathrm{i}-j} - t_\mathrm{i}}{\alpha_{j,\mathrm{ins}}}\right) rv_{\mathrm{i}-j,\mathrm{ins}} \tag{4.3}$$

$$ma_{\mathrm{i,ins}}(p) = \sum_{j=1}^{q} \omega_{j,\mathrm{ins}} \exp\left(\frac{t_{\mathrm{i}-j} - t_\mathrm{i}}{\beta_{j,\mathrm{ins}}}\right) \varepsilon_{\mathrm{i}-j,\mathrm{ins}} \tag{4.4}$$

$$A_{\mathrm{i,ins}} = \sum_{\xi} C_{\xi,\mathrm{ins}} \xi_{\mathrm{i,ins}} \tag{4.5}$$

Where $k(t_\mathrm{i})$ is the Keplerian model evaluated at time t_i, $\dot{\gamma}_\mathrm{ins}$ is an acceleration term for each instrument, γ_ins is the velocity offset of instrument ins, $a_{\mathrm{i,ins}}(q)$ and $m_{\mathrm{i,ins}}(p)$ are the qth and pth order autoregression and moving average respectively, with ϕ and ω being the strength of the correlated noise, α and β are the characteristic time associated to the correlated noise, and $\varepsilon_{\mathrm{i}-j,\mathrm{ins}}$ are the residuals of the model so far. $A_{\mathrm{i,ins}}$ is the linear activity indices correlation model where ξ denotes the activity indices for each instrument and

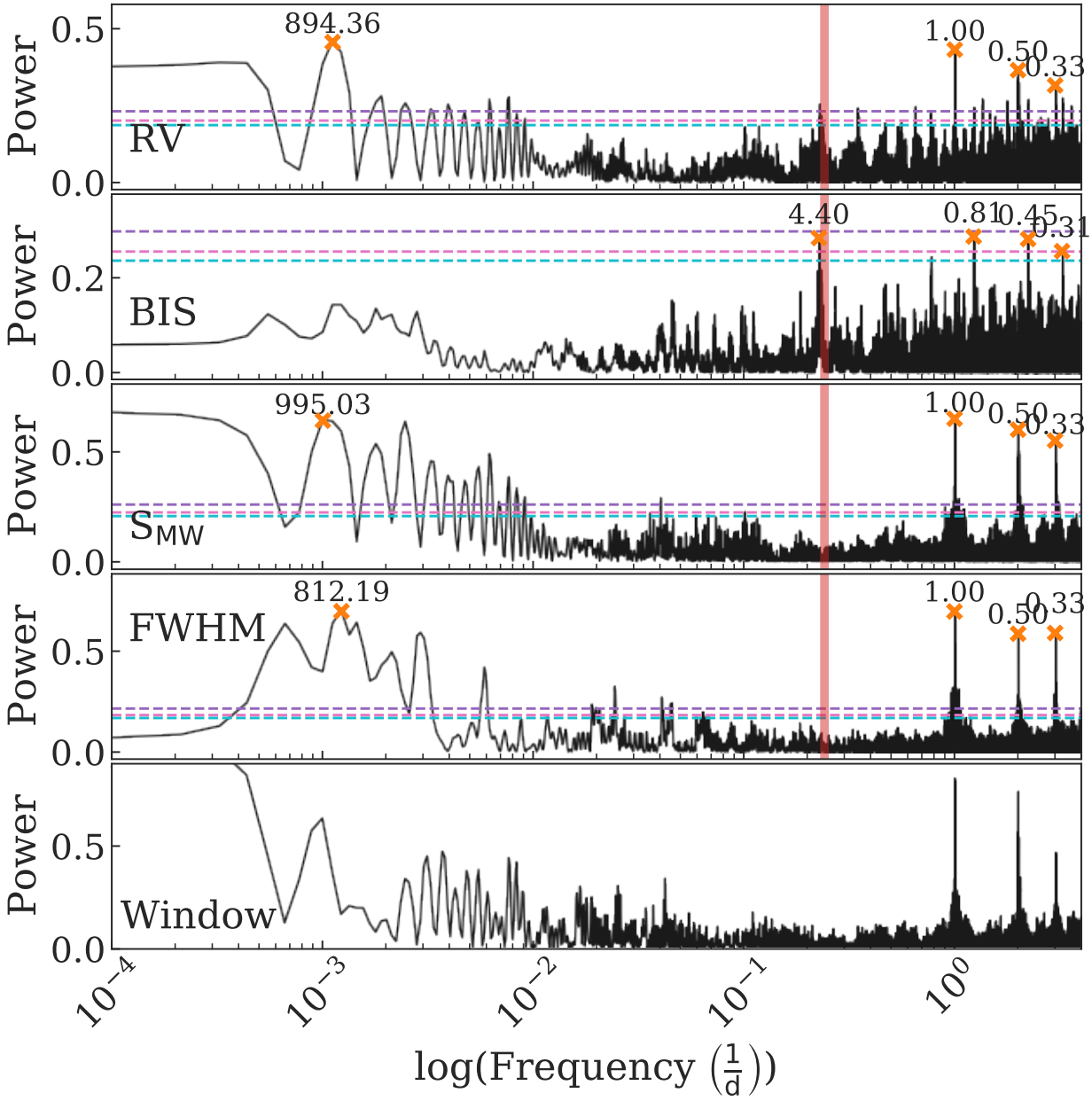

Figure 4.6: From top to bottom: the GLS periodogram for the RVs and activity indices from HARPS and FEROS: BIS, S-index, and CCF FWHM. The bottom panel shows the window function. Horizontal lines from top to bottom are the 0.1, 5 and 10% false alarm probabilities. The vertical red line marks the 4.1375-day planet candidate signal from the *TESS* data. The orange crosses show the most relevant peaks with their values in period written above them.

$C_{\xi,\mathrm{ins}}$ are the activity coefficients. Finally $\sigma_{\mathrm{i,ins}}$ is the white noise term added for each instrument.

Sampling is carried out through `emcee` version 2.2.1 and its Parallel Tempering MCMC (PTMCMC) module, which is capable of sampling multimodal phase spaces without getting stuck in local maxima. This is achieved by modifying the posterior space as shown in Equation 4.6, where $\beta = 1/T$ with T a temperature, $\mathcal{L}$ the original likelihood, and Π is the prior density. This effectively flattens the posterior space with increasing temperature, allowing high-temperature chains to sample the posterior more easily.

$$\mathcal{L}_\beta(x) = \mathcal{L}^\beta(x)\Pi(x) \tag{4.6}$$

Given the active nature of TOI-179 and the significant amount of scatter in the data, we decided to test six different configurations for modeling the system: an AR(1)MA(1) model; activity correlations with the BIS; AR(1)MA(1) plus activities; AR(1)MA(0) model; AR(0)MA(1) model; and a pure keplerian model, hereafter we will refer to those as runs 1, 2, 3, 4, 5, and 6. Additionally, we ran a noise model with activity correlations as a baseline for the model comparison. For the sampling we used 5 temperatures, 1500 walkers, and 6000 steps, with a burn-in period of half the number of steps, totaling 45 million samples for the search phase, and 1500 walkers with 6000 steps for the sampling stage, ending the fitting process with 9 million samples for parameter inference. We chose the temperature ladder to decrease as $1/\sqrt{5}^{\mathrm{i}}$ where i = 0, 1, 2, ...T and T the number of temperatures minus one. $\sqrt{5}$ was chosen by eye to produce chains with high temperatures while retaining some lower temperature chains. We used the same configuration for the walkers, temperatures, and priors for all configurations mentioned previously.

Prior Selection

We chose the period prior to be a Jeffreys prior due to it being uninformative in period space, and we chose the bounds to be from 0.1 to 6 days in order to avoid possible aliases at 8 days. We applied the transformation $s = \sqrt{\mathrm{e}}\sin(\omega)$, $c = \sqrt{\mathrm{e}}\cos(\omega)$, both bounded from -1 and 1 to fit for the eccentricity, e, and argument of periastron, ω. At each step of the MCMC sampling `EMPEROR` makes sure e and ω are physically plausible, i.e. $0 \leq \mathrm{e} < 1$ and $0 \leq \omega \leq 2\pi$. Additionally, an external prior is applied to the eccentricity in order to penalize high values while still allowing them if the data argues for it. The rest of the planetary parameters have uninformative, flat priors. For the stellar density, we chose a prior drawn from the mass and radius estimate derived with `ARIADNE` using the symmetrized 3σ credible interval values as the standard deviation to allow for a more conservative prior. We chose uninformative priors for the instrumental parameters as well, with the exception of the RV jitter, where a Normal prior was chosen in order to penalize high values, and the photometric offset, which also has a Normal prior centered around zero since there is no significant offset in the detrended light curve. We summarise the priors in Table 4.7.

4.2.5 Model Selection

We use the log posterior probability, Bayes Information Criterion (BIC) and Akaike Information Criterion (AIC), defined in Equations 4.7 and 4.8 respectively, where n is the number of data points, k the number of parameters, and $\mathcal{L}$ the maximum likelihood of the model, to do model comparison, using the log posterior to select the final model. The most probable model is Run 2, followed by Run 4, which suggests that the data is dominated by white noise instead of correlated noise. The semiamplitude of all runs is consistent, with the exception of Run 1, which produces a smaller semiamplitude by a factor of two, but still within the 3σ credibility intervals of the other runs.

Table 4.7: Prior choices used in this work

Parameter	Prior
Orbital Parameters	
P [days]	$\ln \mathcal{U}(0.1, 6)$
K [ms^{-1}]	$\mathcal{U}(0, 50)$
T$_c$ [JD]	$\mathcal{U}(min(t^{\dagger}), max(t))$
$\sqrt{\mathrm{e}}\sin(\omega)$	$\mathcal{U}(-1, 1)$
$\sqrt{\mathrm{e}}\cos(\omega)$	$\mathcal{U}(-1, 1)$
ω [rads]	$\mathcal{U}(0, 2\pi)$
e	$\mathcal{N}(0, 0.3^2)$
R_p/R_*	$\mathcal{U}(0.01, 0.5)$
b	$\mathcal{U}(0, 1)$
Stellar Parameters	
ρ_* [gcm^{-3}]	$\mathcal{N}(2.241, 0.479^2)$
$C_{\xi}^{\ddagger}$	$\mathcal{U}(-max(C_{\xi}), max(C_{\upsilon}))$
q_1^*	$\mathcal{U}(0, 1)$
q_2^*	$\mathcal{U}(0, 1)$
RV Noise Parameters	
γ [ms^{-1}]	$\mathcal{U}(0, 3max(\lvert rv \rvert))$
σ [ms^{-1}]	$\mathcal{N}(5, 5^2)$
MA Coefficient ω	$\mathcal{U}(-1, 1)$
MA Timescale β [days]	$\mathcal{U}(0, 10)$
AR Coefficient ϕ	$\mathcal{U}(-1, 1)$
AR Timescale α [days]	$\mathcal{U}(0, 10)$
Transit Noise Parameters	
offset [ppm]	$\mathcal{N}(0, 0.1^2)$
jitter [ppm]	$\ln \mathcal{U}(0.1, 10000)$
dilution	fixed (1)
Acceleration Parameter	
$\dot{\gamma}$ [ms^{-1}/yr]	$\mathcal{U}(-1, 1)$

$^{\dagger}t$ =Time baseline of *TESS* data.

‡ Activity indices were mean subtracted and normalized to their RMS.

* Kipping LD parameters.

Table 4.8: Model statistics for each run, compared against the baseline run. The row in boldface indicates the adopted run. The baseline run is a linear fit to the data.

run	Posterior	BIC	AIC
Run 1	25.89	100.38	9.79
Run 2	**35.48**	**-13.86**	**-22.92**
Run 3	27.45	128.78	11.01
Run 4	28.25	32.93	-3.30
Run 5	25.35	-197.23	219.49
Run 6	23.45	38.21	1.98
baseline	0	0	0

$$\mathrm{BIC} = k\ln(n) - 2\ln(\mathcal{L}) \tag{4.7}$$

$$\mathrm{AIC} = 2k - 2\ln(\mathcal{L}) \tag{4.8}$$

We also did a seventh run which consists of the most probable configuration but with the eccentricity fixed to zero. This run had a resulting log posterior probability of 16.91, significantly lower than the 35.48 from Run 2. It is well known that planets in such close orbits tend to show low eccentricity orbits or even circular orbits, but since this signal is buried deep within the noise, it is not possible to fully constrain the orbital eccentricity, resulting in an eccentric orbit.

As an additional check we ran the same configurations including the Minerva data and found that in all three runs, while the signal is still recovered, significant noise is added to the fit, resulting in lower posterior probabilities. Thus we choose to exclude the Minerva RVs from the final analysis. Table 4.8 shows the aforementioned indicators for each run.

HD 18599 b

The modeling results show a radius ratio of $R_\mathrm{p}/R_* = 0.0311 \pm 0.0008$, resulting in a radius of 2.70±0.05 $R_\oplus$, making HD 18599 b a sub-Neptune planet, while the semi-amplitude, K, of 11±3 m s^{-1}, resulting in a derived mass of $\mathrm{M_p} = 25.5 \pm 4.6\ M_\oplus$, meaning HD 18599 b has a density of $\rho_\mathrm{p} = 7.1 \pm 1.4$ g cm^{-3}. Such a density, therefore, is consistent with the planet maintaining an atmosphere that has a 24% H_2O composition (see Section 4.3). We summarize the model parameters in Table 4.9 and show the phase folded RVs with the best fitting model and 1-3σ credible intervals in Figure 4.7.

We searched for additional signals in the RV residuals, but nothing significant was found. More sophisticated activity models are needed to further disentangle Keplerian signals from activity-induced ones in noisy RV data.

TTV search

The Kepler mission was responsible for the detection of a few thousand exoplanets, from which a handful of multi-planet systems were validated through the transit timing variation (TTV) technique (Holczer et al. 2016). Since the majority of Kepler stars were too faint for precise RV measurements, TTVs became key to deriving planetary masses in many cases, thus validating the planetary systems (Lithwick et al. 2012).

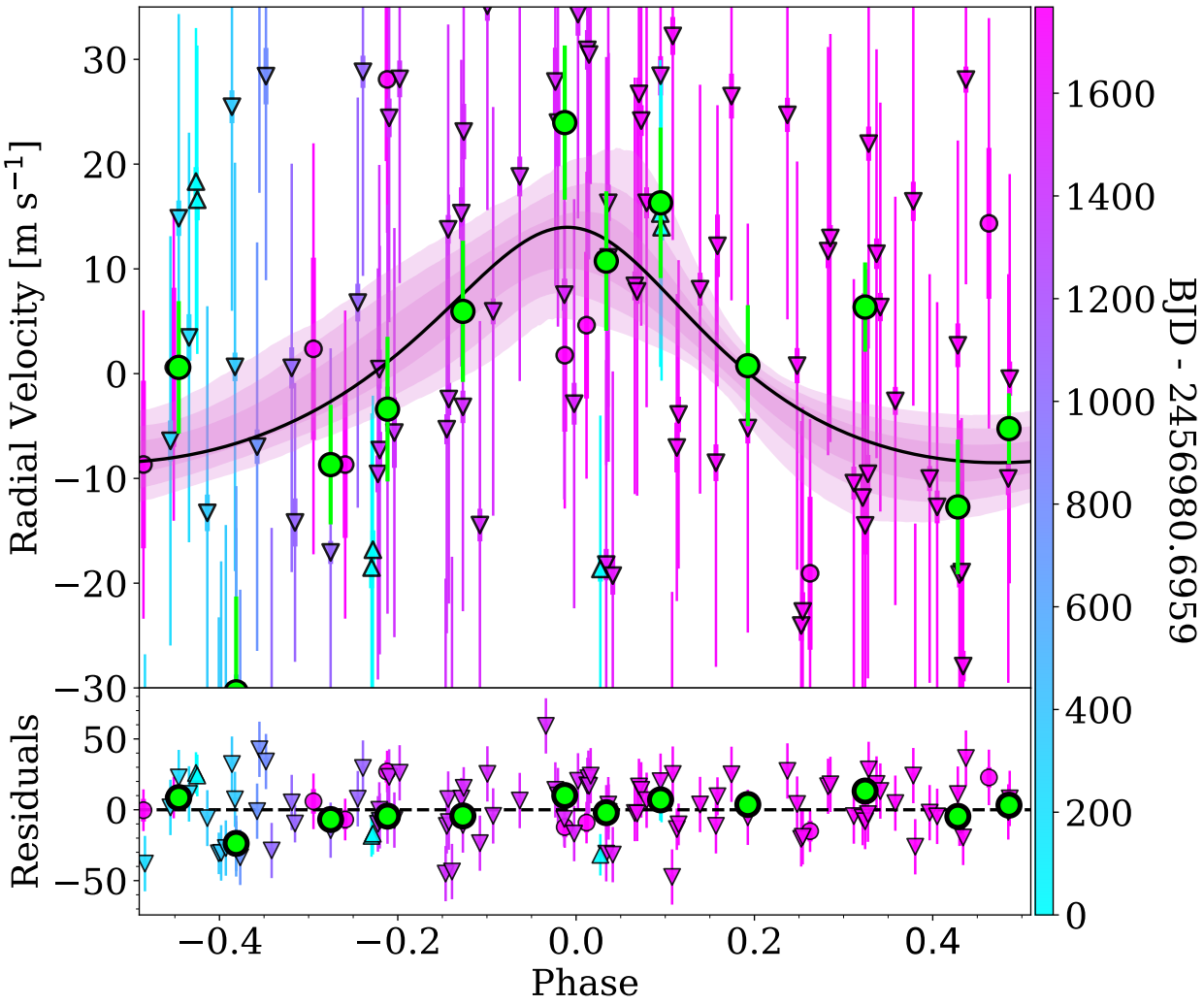

Figure 4.7: HD 18599 RVs folded at 4.137437 days. The black line represents the best fitting model while the purple shaded regions show the 1, 2, and 3σ confidence regions of the model. The lower panel shows the residuals of the fit. Circles are HARPS_pre data, upside-down triangles show HARPS_post data and upright triangles show the FEROS data. Green points show the data binned to 10 points in phase space. The color bar encodes the observing time of each observation.

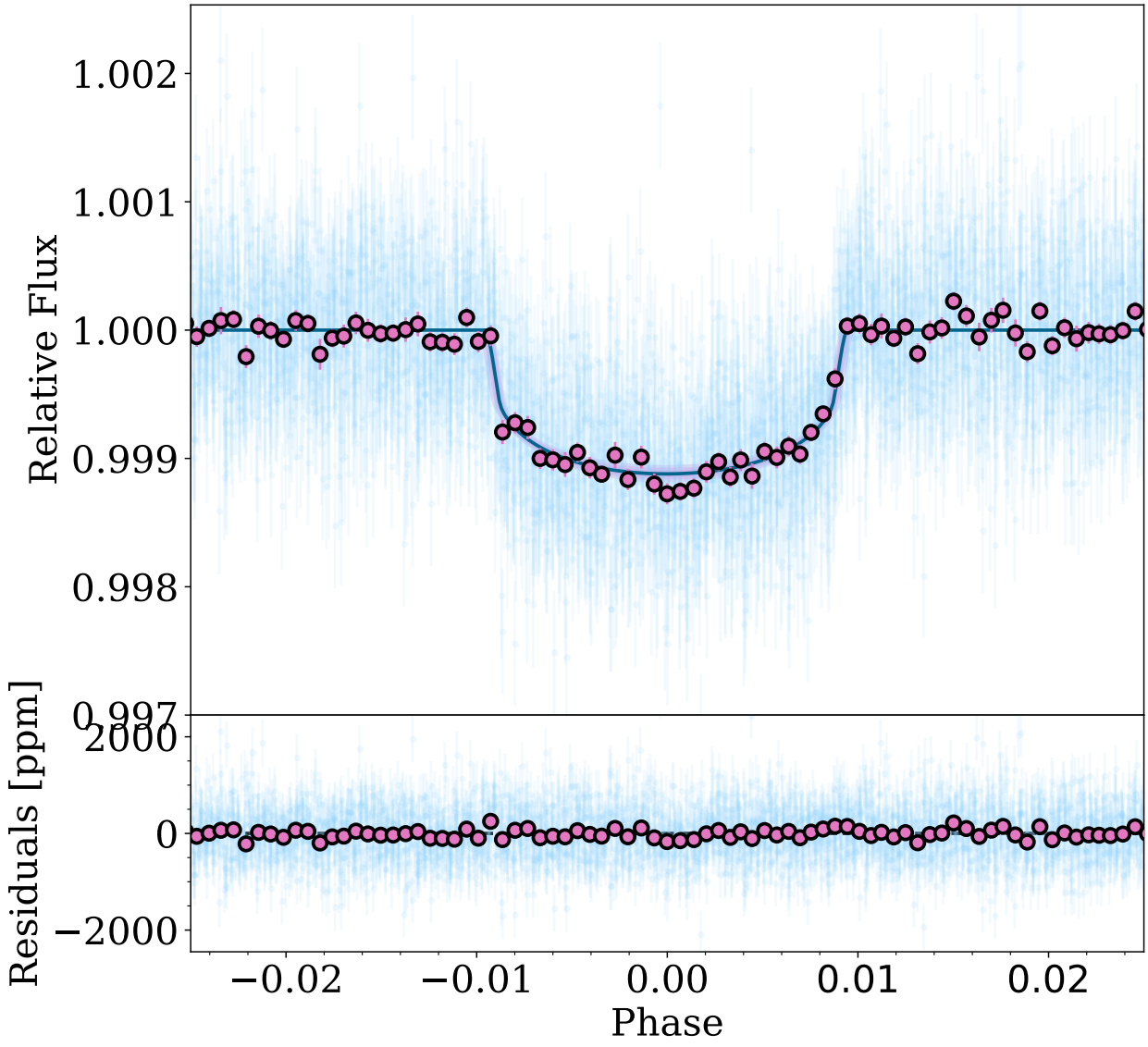

Figure 4.8: *TESS* light curve folded at 4.137437 days in light blue points with pink points showing the light curved binned to 50 points in phase space. The dark blue line represents the best-fitting model and the pink shaded regions show the 1, 2, and 3σ confidence regions of the model. The lower panel shows the residuals of the fit in ppm.

Moreover, this technique supported the idea that hot Jupiters are not part of multi-planet systems (Steffen et al. 2012), therefore setting major constraints on planetary migration models of giant planets. The TTV method (Agol et al. 2005) relies on the comparison between the measured and expected central transit times (T_c) from a linear model given by $T_n = T_0 + n \times P$, where T_n, P and n are the central transits, period, and transit number ($n = 1, 2, 3, ...$) respectively. Therefore, a deviation from the linear model may indicate the occurrence of dynamical interactions, where the most frequent cases are mean motion resonance planet-planet interaction and planet-star interaction leading to orbital tidal decays (Yee et al. 2019).

The TTV analysis was performed using `allesfitter`[7] (Günther & Daylan 2021b) on the detrended light curve. Stellar and planetary parameters were fixed to the median posteriors from Tables 4.3 and 4.9 respectively, except for T_n which used $\mathcal{U}(T_n - 0.05, T_n + 0.05)$ for each nth transit. The O-C transit timing plot (Figure 4.9) agrees with the linear model thus indicating no dynamical interaction with a second body.

[7]https://www.allesfitter.com/

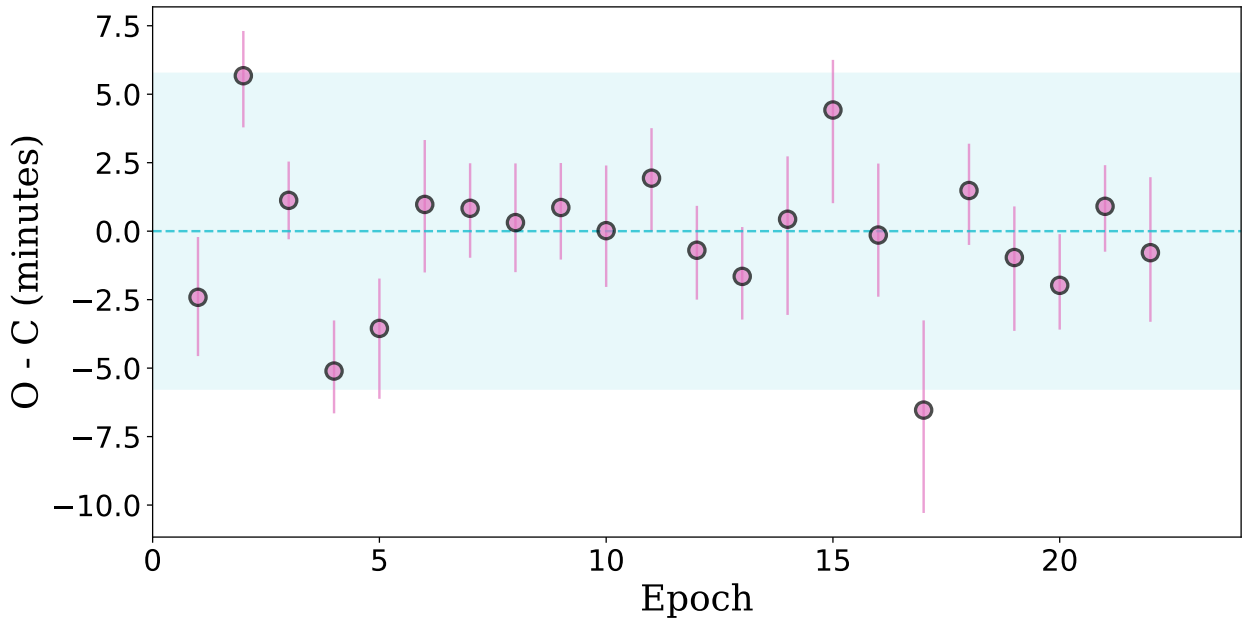

Figure 4.9: Observed minus computed mid-transit times for HD 18599b. The residuals (TTV) are shown considering the proposed ephemerides. The dashed cyan line shows zero variation and the shaded cyan region shows the 1σ uncertainties on the linear ephemeris from `EMPEROR`. The plot shows no significant variation as all observations are within 1σ of the best fitting ephemerides.

Table 4.9: Fitted and Derived Parameters

Parameter	Prior
Orbital Parameters	
Fitted	
P [days]	4.137437±0.000004
K [ms^{-1}]	11±2
T_c [JD]	2458726.9576±0.0004
$\sqrt{e}\sin(\omega)$	-0.1±0.3
$\sqrt{e}\cos(\omega)$	$0.5^{+0.1}_{-0.3}$
R_p/R_*	0.0311±0.0008
b	0.58±0.11
Derived	
ω [rads]	$0.2^{+0.6}_{-0.2}$
e	$0.2^{+0.1}_{-0.2}$
i [deg]	$87.7^{+0.5}_{-0.7}$
$M_p[M_\oplus]$	25.5±4.6
$R_p[R_\oplus]$	2.70±0.05
ρ_p [g cm^{-3}]	7.1±1.4
T_p [JD]	$2458726.41^{+0.27}_{-0.23}$
a/R_*	$13.78^{+0.96}_{-1.08}$
a [AU]	0.05±0.02

T_{eq} [K]	863^{+21}_{-18}
Insolation [$S_\oplus$]	145^{+16}_{-12}
Stellar Parameters	
ρ_* [g cm^{-3}]	$2.87^{+0.62}_{-0.66}$
$C_{\rm FEROS}$	0.2±0.8
$C_{\rm HARPS\_pre}$	$1.0^{+0.3}_{-0.8}$
$C_{\rm HARPS\_post}$	$-2.1^{+0.7}_{-0.0}$
q_1	0.68±0.17
q_2	0.32±0.07
RV Noise Parameters	
$\gamma_{\rm FEROS}$ [m s^{-1}]	$-86.3^{+16.3}_{-14.5}$
$\sigma_{\rm FEROS}$ [m s^{-1}]	$10.2^{+5.0}_{-4.4}$
$\gamma_{\rm HARPS\_pre}$ [m s^{-1}]	$-2.7^{+9.8}_{-9.6}$
$\sigma_{\rm HARPS\_pre}$ [m s^{-1}]	$15.4^{+4.5}_{-3.6}$
$\gamma_{\rm HARPS\_post}$ [m s^{-1}]	$-68.9^{+11.2}_{-11.7}$
MA Coefficient ω	–
MA Timescale β [days]	–
AR Coefficient ϕ	–
AR Timescale α [days]	–
Transit Noise Parameters	
offset [ppm]	-0.000009±0.000003
jitter [ppm]	291±4
dilution	1 (fixed)
Acceleration Parameter	
$\dot{\gamma}$ [ms^{-1}/yr]	17±3

The ARMA correlated noise model was not included in the selected model as described in the text.

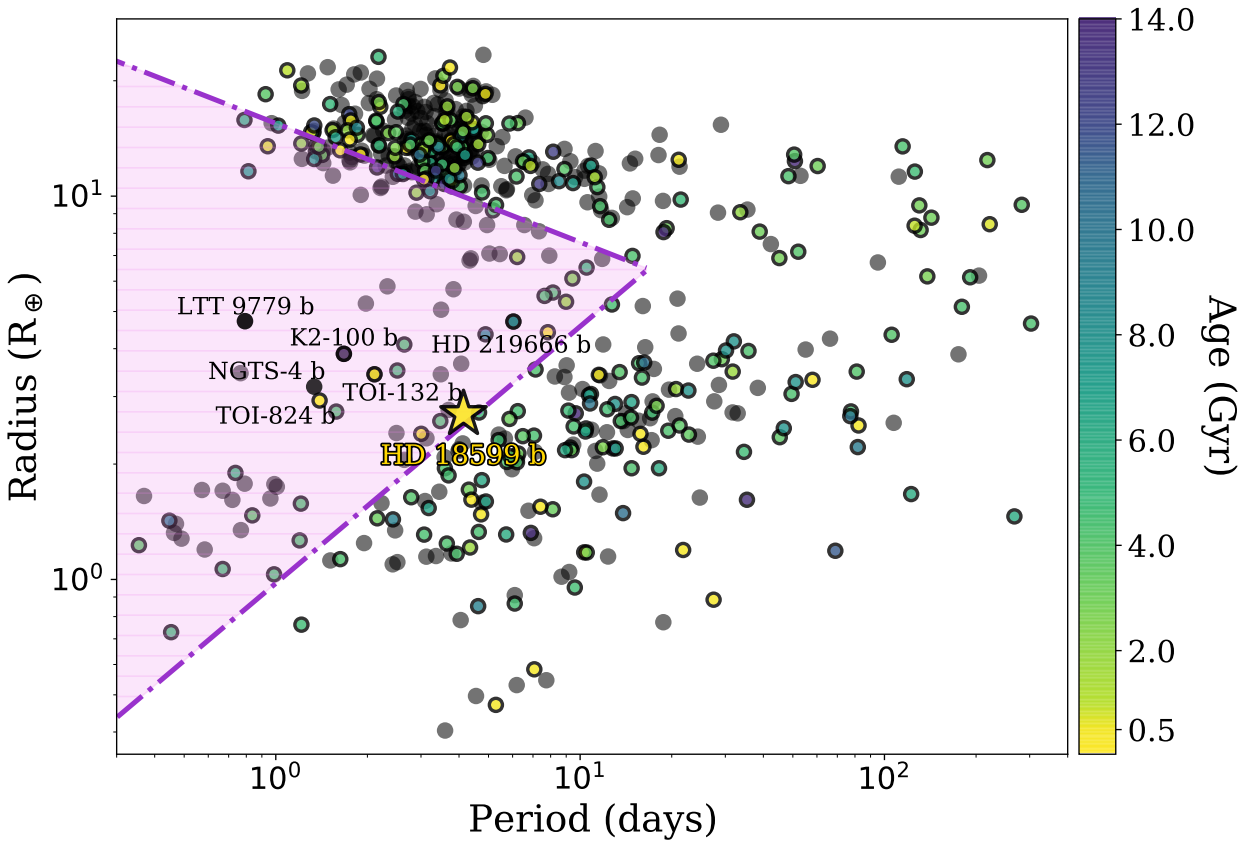

Figure 4.10: Period-radius diagram for planets with radii measured to a precision better than 5%. Relevant discoveries are named, and HD 18599 is shown with a big yellow star at the edge of the desert. The pink shaded area shows the Neptune desert, with the edges defined by Mazeh et al. (2016). The colors show the ages of the systems and black shows systems without an estimated age. We note that ages have not all been measured in a uniform way.

4.3 Discussion

We have confirmed the transit parameters found by de Leon et al. (2023) and have characterized the orbit of the planet. Figure 4.10 places HD 18599 b in the period-radius diagram, where we find it at the edge of the Neptune desert. While the edge of the desert is fairly populated, the Figure shows that HD 18599 b is the youngest mini-Neptune discovered to date within this region, making this planet a key addition to the population.

4.3.1 Possible Compositions

We measured the density of HD 18599 b to be 7.1 ± 1.4 g cm^{-3}, and therefore we can compare this value to other known planets with similar masses and radii by placing it on a mass-radius diagram (Figure 4.11). HD 18599 b is shown by the red star, and it is placed against several two-layer composition models from Zeng et al. (2016) and five two-layer envelope models from Zeng et al. (2019). Its position in the mass-radius diagram suggests the planet can be composed of 23% H_2O, and 77% rock ($MgSiO_3$) and iron core, while the 1σ uncertainties allow the composition to vary from 10 to 41% H_2O.

Due to the inherent degeneracies in three-layer bulk composition models with H/He envelopes on the

sub-Neptune regime ($2 \leq R \leq 4\ R_\oplus$; Lopez & Fortney 2014), we chose to further investigate the internal composition of HD 18599 b using the public tool `smint`[8] (Structure Model INTerpolator) and its interpolation and envelope mass fraction fitting package, first introduced by Piaulet et al. (2021). This code uses models from Lopez & Fortney (2014), Zeng et al. (2016), and Aguichine et al. (2021), along with `emcee` to perform a MCMC fit of the H_2O or H/He mass fraction based on the planetary mass, radius, age and insolation flux. We set up the MCMC with 100 walkers and 10000 steps for all of the analyses. First we studied the H_2O mass fraction (WMF) using the Aguichine et al. (2021) irradiated ocean worlds mass-radius relationships, where we found a WMF of 0.3 ± 0.1. The iron core mass fraction remains widely unconstrained with a value of 0.4 ± 0.3. The gas-to-core mass ratio analysis show that HD 18599 b has a 1^{+14}_{-1}% mass fraction in H/He. The lack of an H/He envelope and the amount of water in the bulk composition argues for a steam atmosphere surrounding the planet.

The high mass regime in which HD 18599 b is found is poorly sampled, making the planet an ideal window into the physical and dynamical processes behind the evolution and formation of young Neptunes and their interactions with active stars. Further work to better characterize the atmosphere of the planet are warranted, which would allow a better understanding of the internal composition of the planet and the physics of young planetary atmospheres. Additional precision RV campaigns would also allow the possibility to discover additional companions in the system, in particular since it is known that small planet systems commonly harbor more than one planet (for example Vach et al. 2021; Scarsdale et al. 2021).

4.3.2 HD 18599 as a Stellar Activity Model Testbed

We tested different correlated noise models in order to account for the stellar activity signals appearing in the RV measurements. These models included AR, MA, linear activity correlations, and a combination of all of these. We found that in this case, linear activity correlations gave rise to a higher posterior probability model, while ARMA models fell short of explaining the correlated noise, likely mainly due to the low observational cadence, since these models perform best under high cadence conditions. HD 18599 is an excellent testbed to apply more sophisticated activity models, also further encouraging more RV follow up work to be pursued.

4.4 Conclusions

Using *TESS* photometry and RVs from HARPS and FEROS we were able to characterize a dense planet orbiting the young star HD 18599. The world is found to have an orbital period of 4.137437±0.000004 days, radius of 2.70±0.05 $R_\oplus$, (making it a mini-Neptune planet in size), and unusually high mass of 25.5±4.6 $M_\oplus$resulting in a planet with a density of 7.1±1.4 g cm^{-3}. The mass-radius diagram and bulk composition models suggests an ice rich core with a range of 10-41% H_2O contribution, and a 1^{+13}_{-1}% H/He envelope mass fraction. Further analysis shows a WMF of 33 ± 10% and an unconstrained iron core mass fraction ranging from 10 to 70%. HD 18599 b is the first mini-Neptune to orbit such a young (< 300 Myr) and bright (V~8.9) star, making it an ideal system to dive deep into evolutionary studies and atmospheric characterization.

[8]https://github.com/cpiaulet/smint

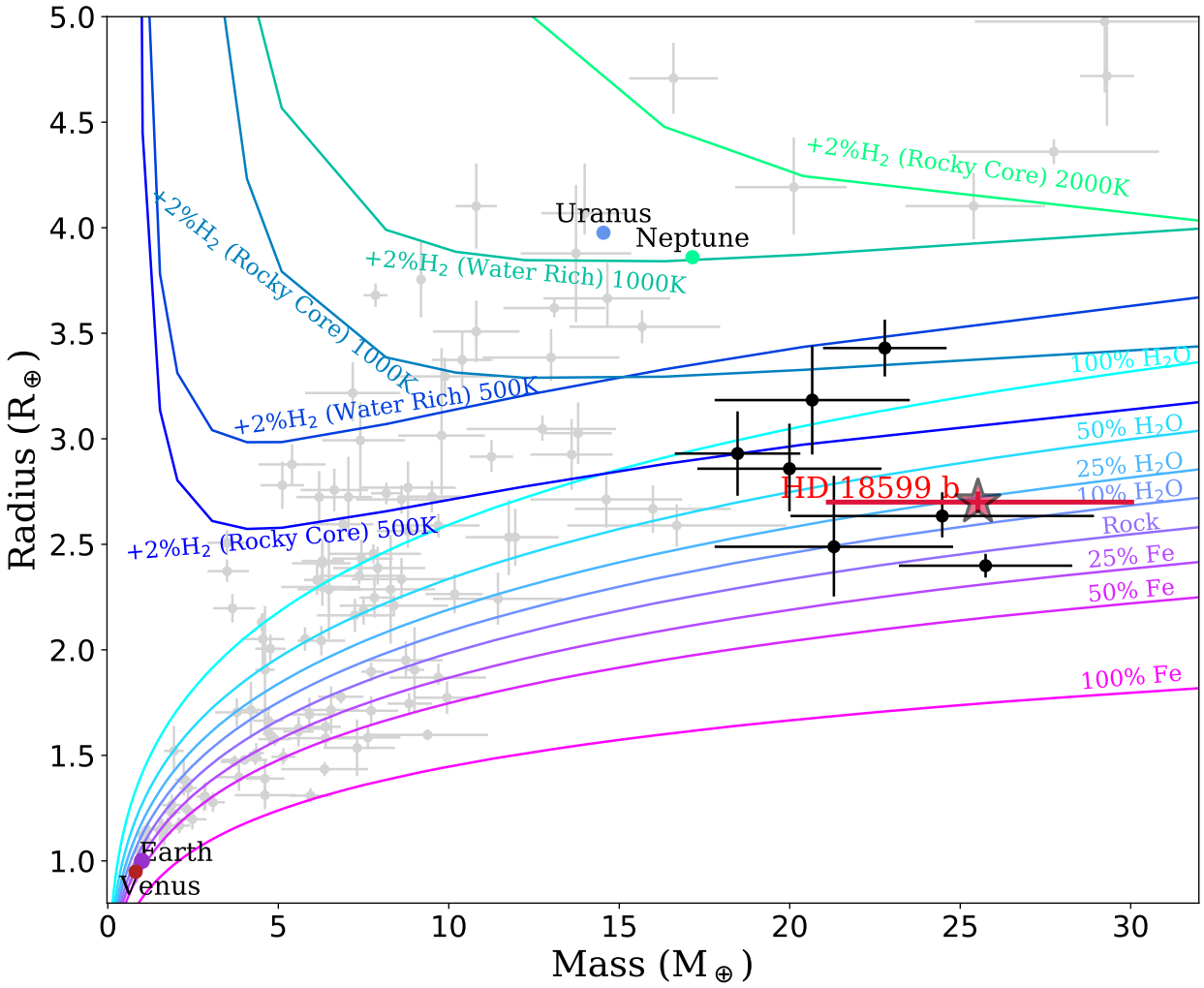

Figure 4.11: Mass-radius diagram for planets with masses and radii measured with a precision better than 20% (gray circles) in the range $R_p < 5\,R_\oplus$ and $M_p < 30\,M_\oplus$, retrieved from the transiting exoplanets catalog `TEPCat` (Southworth 2011). Black points show relevant discoveries. HD 18599 b is shown with a red star. Solid, colored lines show different bi-layer composition models from Zeng et al. (2016), ranging from 100% iron core planet to 100% H_2O planet. Also five two-layer models from Zeng et al. (2019) are shown for 2% H_2 envelopes at different temperatures and core compositions.

Chapter 5

An inflated hot Jupiter orbiting a subgiant star

Based on a paper in preparation.

5.1 Observations

5.1.1 NGTS Photometry

NGTS-N was observed as part of the NGTS survey starting on 2019 Nov 2, up until 2020 Mar 22. A total of 163 962 images were obtained.

Aperture photometry extraction of NGTS observations was performed using the CASUTools[1] photometry package observations, after which they were detrended using an adapted version of the SysRem algorithm (Tamuz et al. 2005). Initial assessment of the light curves (LCs) was done using `ORION`, a modified box-fitting least squares (BLS) algorithm (Kovács et al. 2002; Collier Cameron et al. 2006). For NGTS-N, `ORION` identified a period of 4.16 days. In Table 5.1 we show the unbinned photometry data from NGTS.

[1] `http://casu.ast.cam.ac.uk/surveys-projects/software-release`

Table 5.1: NGTS photometry for NGTS-N The full table is available in a machine-readable format from the online journal. A portion is shown here for guidance.

Time (BJD-2450000)	Flux (normalized)	Flux error
8789.67778568	0.98734	0.01283
8789.67793615	0.98456	0.01283
8789.67808661	0.99887	0.01286
⋮	⋮	⋮

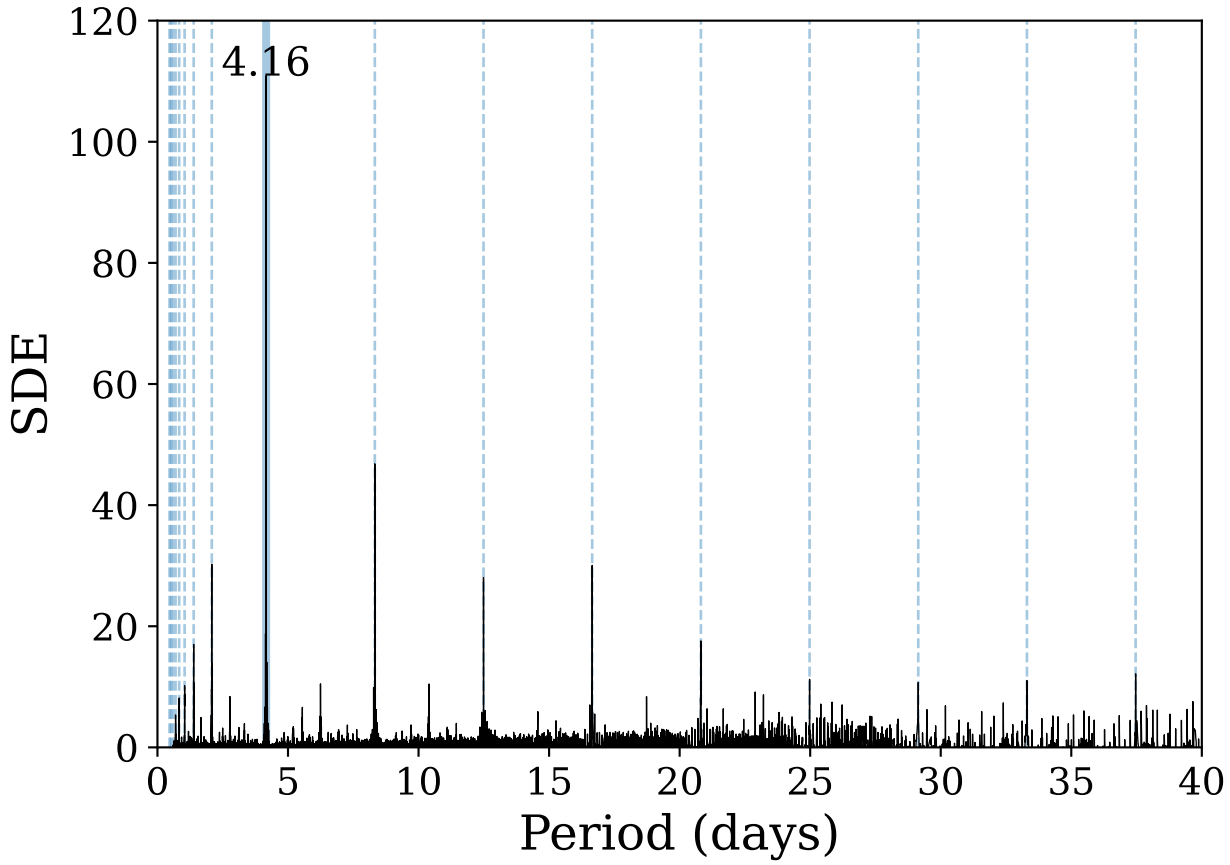

Figure 5.1: The TLS periodogram analysis of the NGTS-N *TESS* LC. Shown in a blue solid line is the detected transit period of 4.16 days and the dashed lines show the corresponding aliases.

5.1.2 *TESS* Photometry

NGTS-N was also observed by *TESS* in Sectors 5, 6, 32, and 33 obtaining 30 and 10-minute cadence Full Frame Images (FFIs) starting 2018 Nov 15, and finishing on 2021 Jan 13. The FFIs were processed with the Quick-Look Pipeline and made publicly available as a High-Level Science Product on MAST (Huang et al. 2020b). It was identified as a CTOI by Olmschenk et al. (2021), after which the star was promoted to TOI status as TOI-2721.

We independently searched the *TESS* LC for transits using the `Transit Least Squares`[2] (TLS) `Python` package by Hippke & Heller (2019), and found a period of 4.16 days, consistent with the period found by `ORION` using the NGTS data, with a signal detection efficiency (SDE; Pope et al. 2016) of 111 with no other significant signal detected. We show the TLS periodogram in Figure 5.1

Using Gaia DR3 (Gaia Collaboration et al. 2023), `eleanor`[3] (Feinstein et al. 2019) and `TESSCut` (Brasseur et al. 2019) we searched for possible contaminants that could fall inside the *TESS* aperture. In Figure 5.2 we show there are no contaminating stars in the *TESS* aperture and thus we expect to find no dilution in it.

[2] `https://github.com/hippke/tls`
[3] `https://adina.feinste.in/eleanor/`

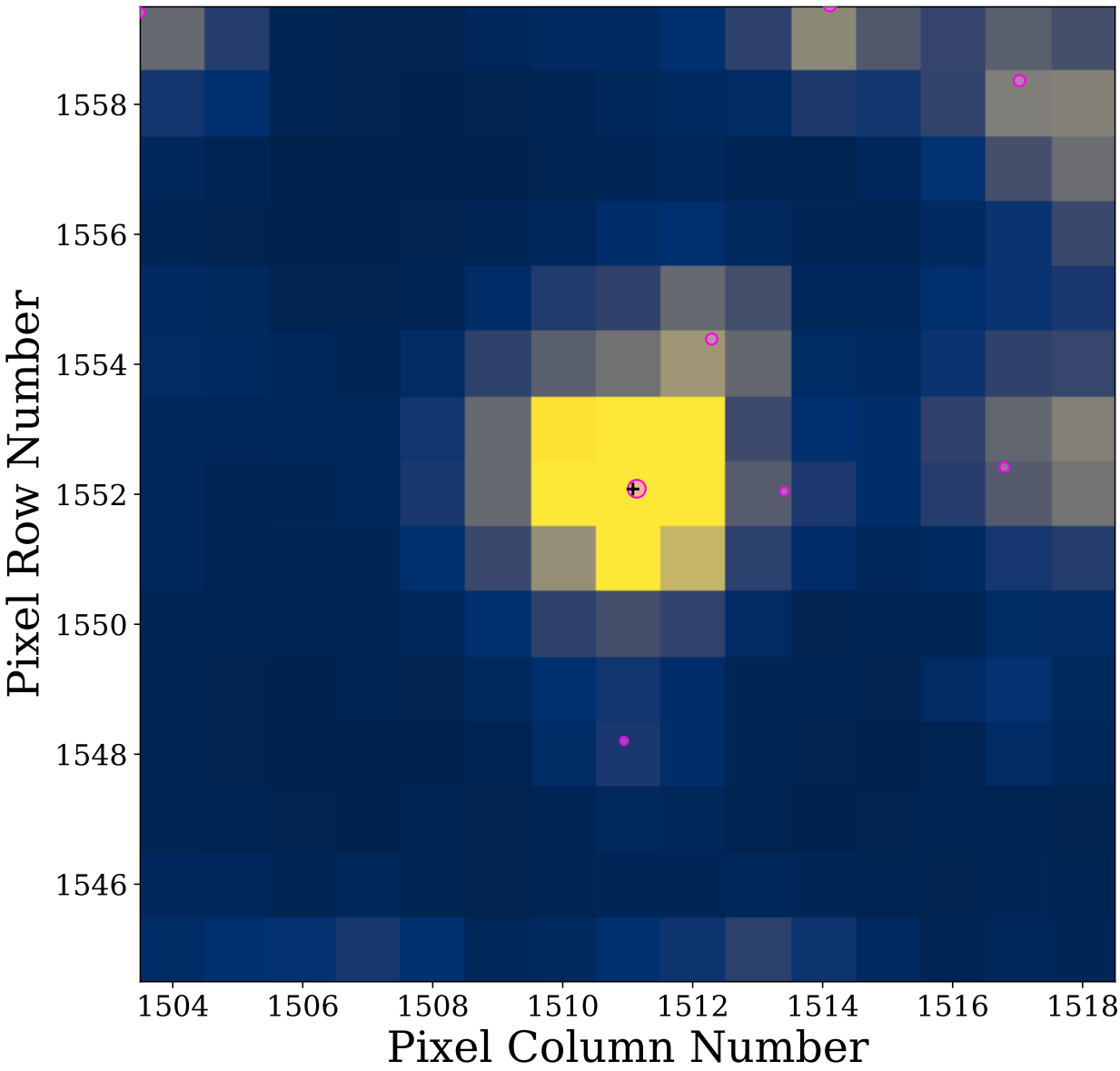

Figure 5.2: A cut of the FFI containing NGTS-N (in a pink circle with a black cross) and nearby Gaia sources in pink circles.

Table 5.2: Ground based photometric follow-up of NGTS-N. The full table is available in a machine-readable format from the online journal. A portion is shown here for guidance.

Instrument	BJD (-2450000)	Flux (normalized)	Flux err
MEarth	9513.5855	1.0112	0.0050
MEarth	9513.5856	1.0039	0.0047
⋮	⋮	⋮	⋮
PEST	9526.1290	1.0135	0.0065
PEST	9526.1304	1.0066	0.0061
⋮	⋮	⋮	⋮
LCO	9563.554	0.995	0.001
LCO	9563.558	1.000	0.001
⋮	⋮	⋮	⋮

5.1.3 Ground Based Follow-up

We obtained follow-up transits for NGTS-Nb from MEarth-South (Irwin et al. 2015), at Cerro Tololo Inter American Observatory (CTIO) on the 26th of October 2021. Five telescopes were used with the RG715 filter taking a total of 1498 images, 323 of which were discarded for further analysis due to them being taken after the meridian flip, which introduces an offset in the out-of-transit data. We noticed a significant linear trend in the data that was detrended during the joint modeling (see Section 5.2.2).

An additional full transit was observed by the Perth Exoplanet Survey Telescope (PEST)[4] on the 7th of November 2021. PEST is located near Perth, Australia. The 0.3 m telescope is equipped with a 5544×3694 QHY183M camera with a gp filter. Images are binned 2x2 in software giving an image scale of $0\farcs7$ pixel^{-1} resulting in a $32' \times 21'$ field of view. A custom pipeline based on `C-Munipack`[5] was used to calibrate the images and extract the differential photometry.

Finally, a full transit was acquired from the Las Cumbres Observatory Global Telescope (LCOGT; Brown et al. 2013) at CTIO, using the SBIG camera and gp filter on the 15th of December 2021. The LCs are shown in Figure 5.5 and the data are summarized in Table 5.2.

5.1.4 SOAR Speckle Imaging

On 2021 Oct 1, the 4.1-m SOAR acquired a high-resolution image of NGTS-N using the HRCam instrument. NGTS-N (TOI-2721) was observed as part of the SOAR TESS survey (Ziegler et al. 2020, 2021). The contrast curve in the I band and autocorrelation functions can be seen in Figure 5.3, where no sign of a companion can be found.

5.1.5 Spectroscopy

We obtained multi-epoch spectroscopy for both NGTS-N with the FEROS spectrograph, mounted on the 2.2-m MPG/ESO telescope at La Silla observatory (Kaufer et al. 1999), in order to determine the planetary nature of the transit signals observed in the photometry.

[4] `http://pestobservatory.com/`
[5] http://c-munipack.sourceforge.net

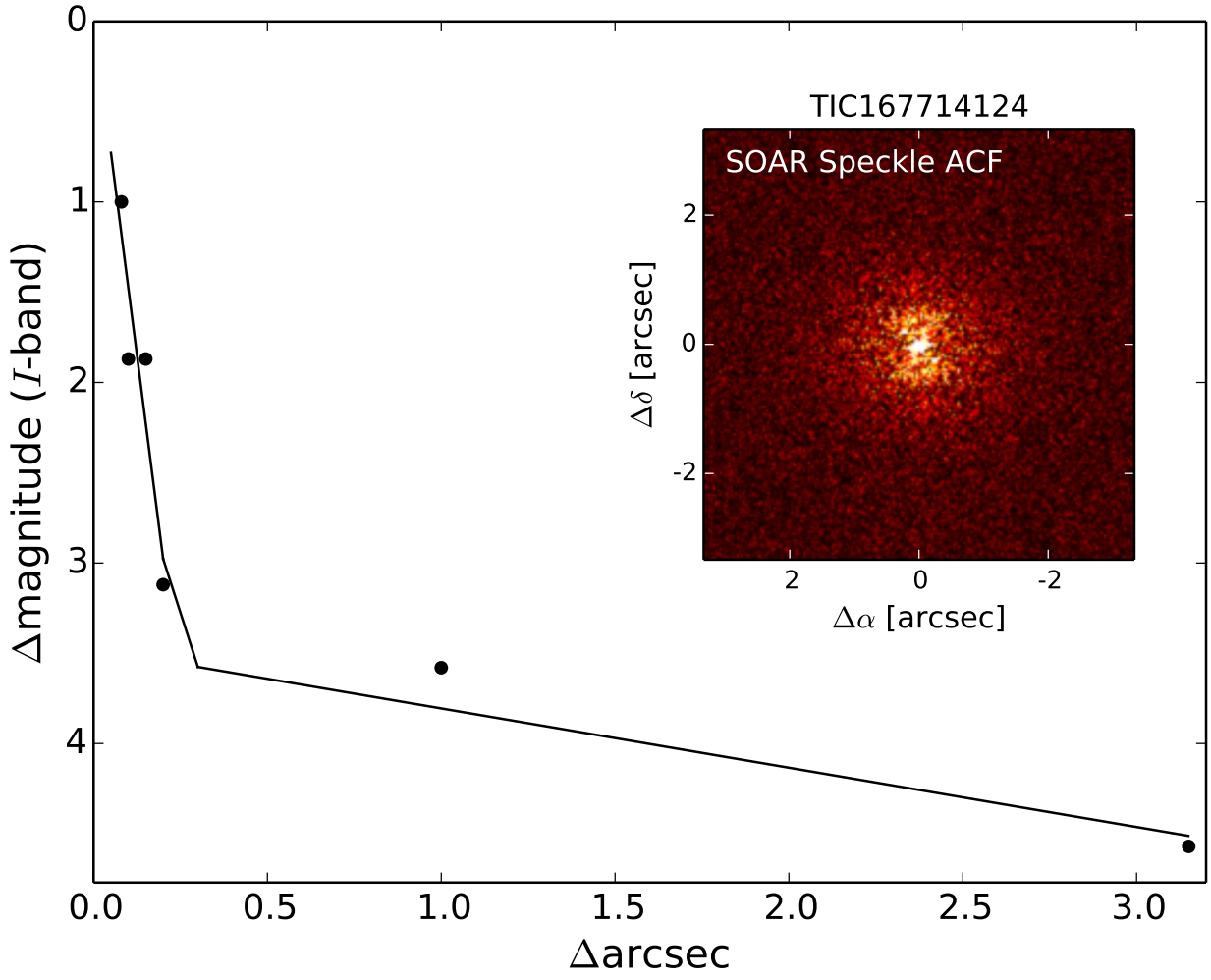

Figure 5.3: Speckle imaging of NGTS-N by HRCam at the Southern Astrophysical Research telescope. The contrast curve plots show the linear fits to the 5-σ contrast curves on either side of 0.″2. The autocorrelation functions are shown inset.

Table 5.3: Radial Velocities. The full table is available in a machine-readable format from the online journal. A portion is shown here for guidance.

BJD (-2450000)	RV (m s^{-1})	ΔRV (m s^{-1})
9493.747	20178.9	15.5
9501.782	20055.9	11.1
9502.796	20053.4	12.2
⋮	⋮	⋮

Table 5.4: SPECIES output on FEROS spectra.

Property	Value	Error
Teff (K)	5760	120
log g	4.41	0.21
[Fe/H]	0.00	0.05
v sin i (km s^{-1})	6.05	0.63

A total of 12 observations were performed under programs 0108.A-9007(A) and 0109.A-9024(A) (PI: JIV). The observations were carried out with the simultaneous calibration mode with a ThAr lamp and reduced with the CERES pipeline (Brahm et al. 2017), which also calculates the RVs using the cross-correlation function (CCF) method. The observed RVs can be found in Table 5.3.

5.2 Analysis

5.2.1 Stellar Properties

SPECIES

We analyzed the 1D stacked FEROS spectra using SPECIES (Soto & Jenkins 2018; Soto et al. 2021), an automated code to derive stellar parameters using high-resolution echelle spectra. It makes use of equivalent widths from a number of neutral and ionized iron lines (measured using line equivalent widths, Soto et al. 2021) to derive the atmospheric parameters (temperature, metallicity, surface gravity, and microturbulence). Together with ATLAS9 model atmospheres (Castelli & Kurucz 2003), it solves the radiative transfer and hydrostatic equilibrium equations using MOOG (Sneden 1973), imposing local thermodynamic equilibrium (LTE) conditions, as well as excitation and ionization equilibrium. The rotational and macro turbulent velocities were derived using spectral line fitting and analytic relations respectively. We summarize SPECIES outputs in Table 5.4.

ARIADNE

Using the outputs from SPECIES as priors, we studied the Spectral Energy Distribution (SED) of the star using ARIADNE[6], a PYTHON package written to fit SEDs with different stellar atmosphere model grids, which have been previously convolved with several publicly available broadband filters, in a Bayesian framework (Vines & Jenkins 2022). In order to sample the parameter space, ARIADNE utilizes the Nested Sampling

[6]https://github.com/jvines/astroARIADNE

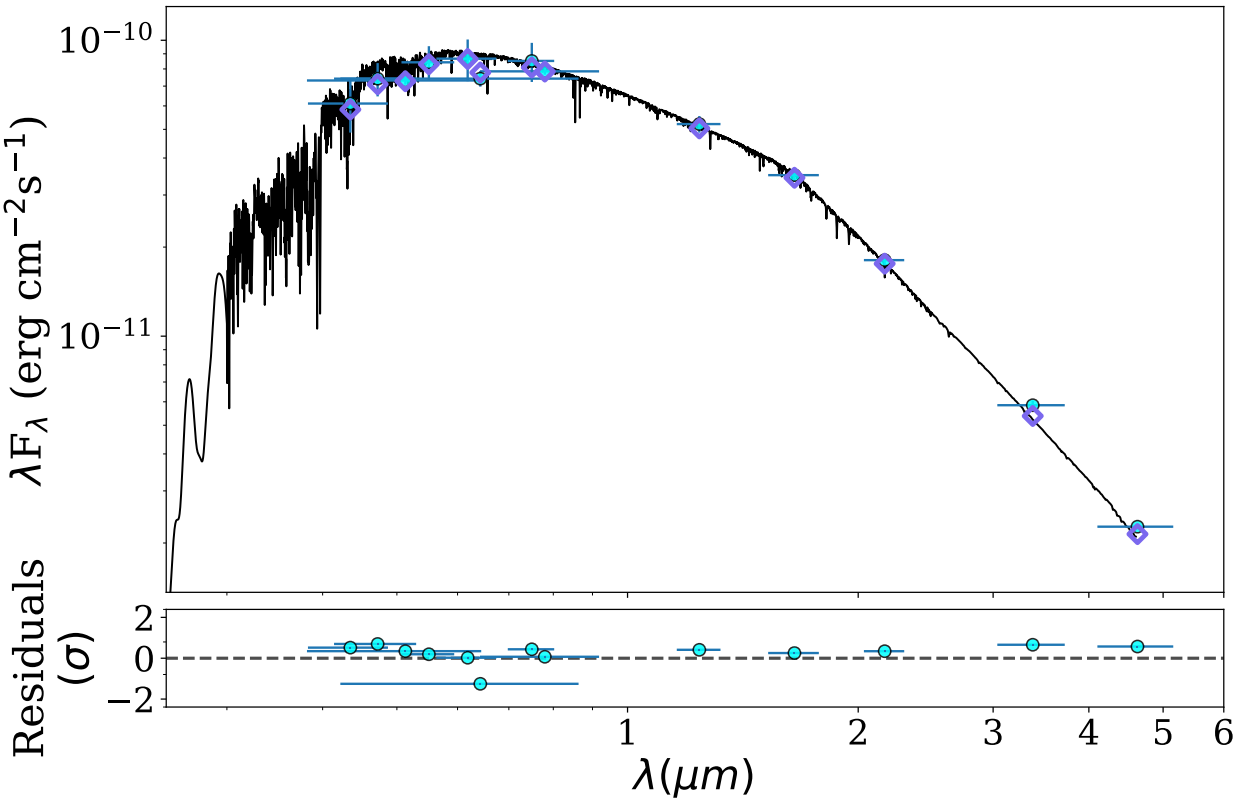

Figure 5.4: The best fitting SEDs (black line) for NGTS-N based on the photometric data (cyan points) presented in Table 5.5. Horizontal error bars show the bandpass width. The pink diamonds show the synthetic magnitudes at the wavelengths of the photometric data. The lower panels show the residuals of the best-fit models.

algorithm implemented in `dynesty`, which calculates the evidence of each model along with the posterior distributions (Skilling 2004, 2006; Higson et al. 2019; Speagle 2019).

`ARIADNE` computes the effective temperature, log g, [Fe/H], Av, and radius of the star using the Gaia DR3 distances from Bailer-Jones et al. (2021), and the line-of-sight V-band extinction found in the SFD dustmap (Schlegel et al. 1998; Schlafly & Finkbeiner 2011) as priors. The final set of parameters is derived through Bayesian Model Averaging, a weighted average that takes the evidence of each model as weights.

We modeled NGTS-N with four atmosphere grids, Phoenix V2 (Husser et al. 2013), BT-Settl (Hauschildt et al. 1999; Allard et al. 2012), Castelli & Kurucz (2003) and Kurucz (1993). In Figure 5.4 we show the SED, and in Table 5.5 we report the relevant observational and derived properties along with the method used.

5.2.2 Global Modelling

Prior to modeling, we binned the NGTS data into one-minute bins to decrease the computational cost of modeling. The modeling itself was performed using `EMPEROR.T`, an upgraded version of `EMPEROR` (Pena & Jenkins 2023, in prep) that can model both LCs and RVs either separately or in a joint model.

`EMPEROR` utilizes the Mandel & Agol (2002) quadratic limb-darkening law implemented in the `PyTransit` `Python` package (Parviainen 2015) with limb-darkening parameters following the parametrization proposed

Table 5.5: Stellar properties of NGTS-N

Property	Value	Source
2MASS I.D.	05214111-3839245	2MASS
Gaia source I.D.	4819647205326045824	*Gaia DR3*
TIC I.D.	TIC-167714124	TIC8
TOI	2721	
Astrometric Properties		
R.A.	$05^{h}21^{m}41^{s}11$	2MASS
Dec	$-38°39'24''.51$	2MASS
$\mu_{\mathrm{R.A.}}$ (mas y^{-1})	-7.5 ± 1.4	UCAC4
$\mu_{\mathrm{Dec.}}$ (mas y^{-1})	-7.5 ± 1.4	UCAC4
Photometric Properties		
V (mag)	13.439 ± 0.026	APASS
B (mag)	14.118 ± 0.017	APASS
g (mag)	13.732 ± 0.011	APASS
r (mag)	13.269 ± 0.035	APASS
i (mag)	13.079 ± 0.037	APASS
G (mag)	13.336 ± 0.003	*Gaia*
BP (mag)	13.630 ± 0.003	*Gaia*
RP (mag)	12.772 ± 0.004	*Gaia*
NGTS (mag)	12.85	This work
TESS (mag)	12.848 ± 0.006	TIC8
J (mag)	12.175 ± 0.023	2MASS
H (mag)	11.822 ± 0.024	2MASS
Ks (mag)	11.775 ± 0.024	2MASS
W1 (mag)	11.695 ± 0.023	WISE
W2 (mag)	11.738 ± 0.020	WISE
Derived Properties		
T_{eff} (K)	5710 ± 70	ARIADNE
$[Fe/H]$	0.00 ± 0.04	ARIADNE
vsini (km s^{-1})	6.1 ± 0.6	SPECIES
log g	$4.43^{+0.14}_{-0.16}$	ARIADNE
$M_s(M_\odot)$	$0.96^{+0.11}_{-0.05}$	ARIADNE
$R_s(R_\odot)$	$1.70^{+0.20}_{-0.21}$	ARIADNE
ρ (g cm^{-3})	$0.585^{+0.021}_{-0.018}$	EMPEROR
Age (Gyr)	9.97 ± 2.58	ARIADNE
Distance (pc)	852^{+99}_{-100}	ARIADNE
A_V (mag)	0.05 ± 0.02	ARIADNE

2MASS (Skrutskie et al. 2006); UCAC4 (Zacharias et al. 2013); APASS (Henden & Munari 2014); WISE (Wright et al. 2010); *Gaia* (Gaia Collaboration et al. 2023)

by Kipping (2016) to model the LCs. We also included a dilution and offset to the light curve as defined by Espinoza et al. (2019), the former of which we fixed to unity during the fitting procedure due to the lack of any significant contaminating sources. Since the MEarth LC shows a clear systematic flux increase with time, a linear trend was included in the model (See Figure 5.5). The final parameter related to the LC is the stellar density, derived from the stellar analysis, which helps decouple the radius ratio and the impact parameter (Sandford et al. 2019; Vines et al. 2019)

The RVs, in turn, are mean subtracted and afterward modeled with a standard Keplerian model, including an instrumental velocity offset γ, a white noise parameter σ, and a first-order acceleration term.

`EMPEROR` utilizes `emcee` v. 2.2.1 and the Parallel Tempering Markov Chain Monte Carlo (PTMCMC) module to perform an initial search of the best-fitting parameters. The following step consists of generating a Gaussian ball around the posterior maximum which works as a starting position for a regular MCMC sampler to gather samples in order to perform parameter inference.

The MCMC set-up we used for sampling was: 5 temperatures, 2000 walkers, and 20000 steps for the PTMCMC, with a burn-in period of half the number of steps, totaling 200 million samples for the search stage, and 2000 walkers with 100000 steps for the sample gathering stage, which results in 100 million samples used for parameter inference. The beta ladder decreases as $1/\sqrt{(5)}^{\mathrm{i}}$ with $\mathrm{i} = 1, 2, ...T$ and T the number of temperatures minus one, as an aggressive temperature increase makes the walkers less likely to become stuck during the searching stage.

Prior Selection

We set the period prior as a Jeffreys (log uniform) prior, starting from 0.1 days to three times the total baseline of the RV data. The eccentricity and argument of periastron were fixed to 0 and $\pi/2$ respectively, due to the periods of both planet candidates recovered from the photometry being small (Anderson & Francis 2012b), and the initial model assessment favored circular orbits. The other planetary parameters have uniform priors. The instrumental velocity offset has a uniform prior, while the instrumental RV jitter has a zero-mean Gaussian prior. The photometric instrumental priors, however, differ, as the offset has a zero-mean Gaussian prior, the white noise uses a Jeffreys prior. The dilution was fixed to unity, and the Kipping parameters use a Uniform prior ranging from 0 to 1. The prior details are found in Table 5.6.

NGTS-N

We found NGTS-Nb to be a HJ with a period of 4.162734 ± 0.000004 days. We tested two different configurations for the global modeling, one with free eccentricity and another with a circular orbit. We found that the preferred model was the latter by a significant amount (Δ BIC = -9758).

NGTS-Nb is inflated with a mass and radius of $1.12 \pm 0.12\,\mathrm{M}_J$ and $1.61 \pm 0.16\,\mathrm{R}_J$ respectively, resulting in a density of $0.30^{+0.11}_{-0.08}$ g cm^{-3}. Coupled with an equilibrium temperature of 1410 ± 20 K (assuming a bond albedo of 0) places NGTS-Nb in a sparsely populated portion of the radius-temperature diagram (see Section 5.3). Figure 5.5 shows the phase-folded LCs and RVs for NGTS-Nb and the model parameters are summarized in Table 5.7.

Table 5.6: Prior choices used in this work

Parameter	Prior
Orbital Parameters	
P [days]	$\ln \mathcal{U}(0.1, 3\max(t_{\rm RV}))$
K [ms^{-1}]	$\mathcal{U}(0, 3\max(\lvert{\rm RV}\rvert)$
T$_c$ [JD]	$\mathcal{U}(\min(t^{\dagger}), \max(t))$
ω [rad]	$\pi/2$ (fixed)
e	0 (fixed)
R_p/R_*	$\mathcal{U}(0.01, 0.5)$
b	$\mathcal{U}(0, 1)$
Stellar Parameters	
ρ_* [g cm^{-3}]	$\mathcal{N}(\mathrm{d}^a, \sigma\mathrm{d}^2)$
q_1^*	$\mathcal{U}(0, 1)$
q_2^*	$\mathcal{U}(0, 1)$
RV Noise Parameters	
γ [ms^{-1}]	$\mathcal{U}(0, 3\max(\lvert{\rm RV}\rvert))$
σ [ms^{-1}]	$\mathcal{N}(3, 3^2)$
Transit Noise Parameters	
offset [ppm]	$\mathcal{N}(0, 0.1^2)$
jitter [ppm]	$\ln \mathcal{U}(0.1, 10000)$
dilution	fixed (1)
Acceleration Parameter	
$\dot{\gamma}$ [ms^{-1}/yr]	$\mathcal{U}(-1, 1)$
trend$_{\rm MEarth}$	$\mathcal{U}(-1, 1)$

$^{\dagger}t$ =Time baseline of *TESS* and NGTS data for NGTS-N.

* Kipping LD parameters.

^{a} the prior density is calculated using the radius and mass from Tables 5.5, respectively.

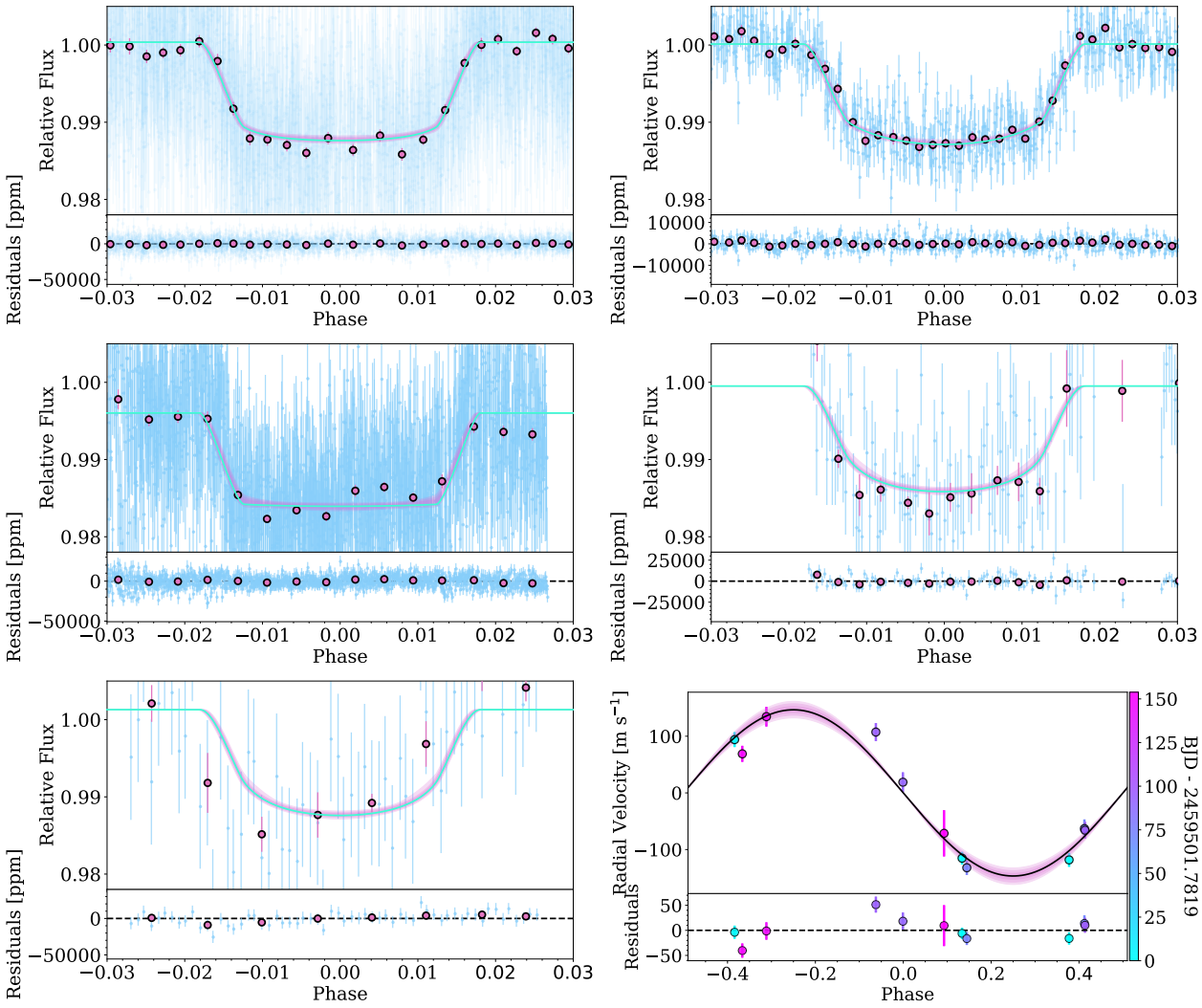

Figure 5.5: NGTS-Nb models. Top: The left and right panels are the phase-folded NGTS and TESS LCs respectively. Middle: This section shows the MEarth and PEST photometric data (left and right respectively). Bottom: The LCO LC and the FEROS RVs folded around the best-fitting period. The pink bands show the 1, 2, and 3σ confidence intervals for the models. The pink circles are the binned photometry in phase space. The bottom panels in each plot show the residuals of the fit.

Table 5.7: Model parameters for NGTS-Nb

Property	Value NGTS-Nb
Fitted Parameters	
P (days)	4.162734 ± 0.000004
K (m s^{-1})	$146.63^{+8.26}_{-5.97}$
e	0 (fixed)
w (deg)	90 (fixed)
T_C (BJD)	2459039.1615 ± 0.0004
R_p/R_*	0.110 ± 0.001
b	0.63 ± 0.01
a/R_*	$8.16^{+0.09}_{-0.08}$
Derived Parameters	
$M_p(M_J)$	1.12 ± 0.12
$R_p(R_J)$	1.61 ± 0.16
ρ_p (g cm^{-3})	$0.30^{+0.11}_{-0.08}$
incl (deg)	85.6 ± 0.1
a (AU)	0.064 ± 0.008
T_{eq} (K)	1410 ± 20
Other Parameters	
$\dot{\gamma}$ (ms^{-1}yr^{-1})	195^{+25}_{-42}
$\gamma_{\rm FEROS}$ m s^{-1}	-27 ± 8
$\sigma_{\rm FEROS}$ m s^{-1}	6 ± 3
$\gamma_{\rm NGTS}$	-0.00036 ± 0.000042
$\sigma_{\rm NGTS}$ (ppm)	6200^{+40}_{-30}
$\gamma_{\rm TESS}$	-0.00013 ± 0.00003
$\sigma_{\rm TESS}$ (ppm)	1110 ± 40
$\gamma_{\rm LCO}$	-0.001 ± 0.001
$\sigma_{\rm LCO}$ (ppm)	8050^{+1200}_{-230}
$\gamma_{\rm MEarth}$	-0.004 ± 0.001
$\sigma_{\rm MEarth}$ (ppm)	6000^{+120}_{-210}
$\gamma_{\rm PEST}$	-0.0005 ± 0.0005
$\sigma_{\rm PEST}$ (ppm)	10^{+50}_{-10}
$q1_{\rm NGTS}$	$0.22^{+0.05}_{-0.04}$
$q2_{\rm NGTS}$	$0.05^{+0.04}_{-0.03}$
$q1_{\rm TESS}$	0.35 ± 0.04
$q2_{\rm TESS}$	0.45 ± 0.05
$q1_{\rm MEarth}$	$0.00^{+0.028}_{-0.003}$
$q2_{\rm MEarth}$	0.60 ± 0.05
$q1_{\rm LCO,PEST}$	$0.94^{+0.04}_{-0.05}$
$q2_{\rm LCO,PEST}$	0.14 ± 0.05
$\rm trend_{MEarth}$	0.029 ± 0.003

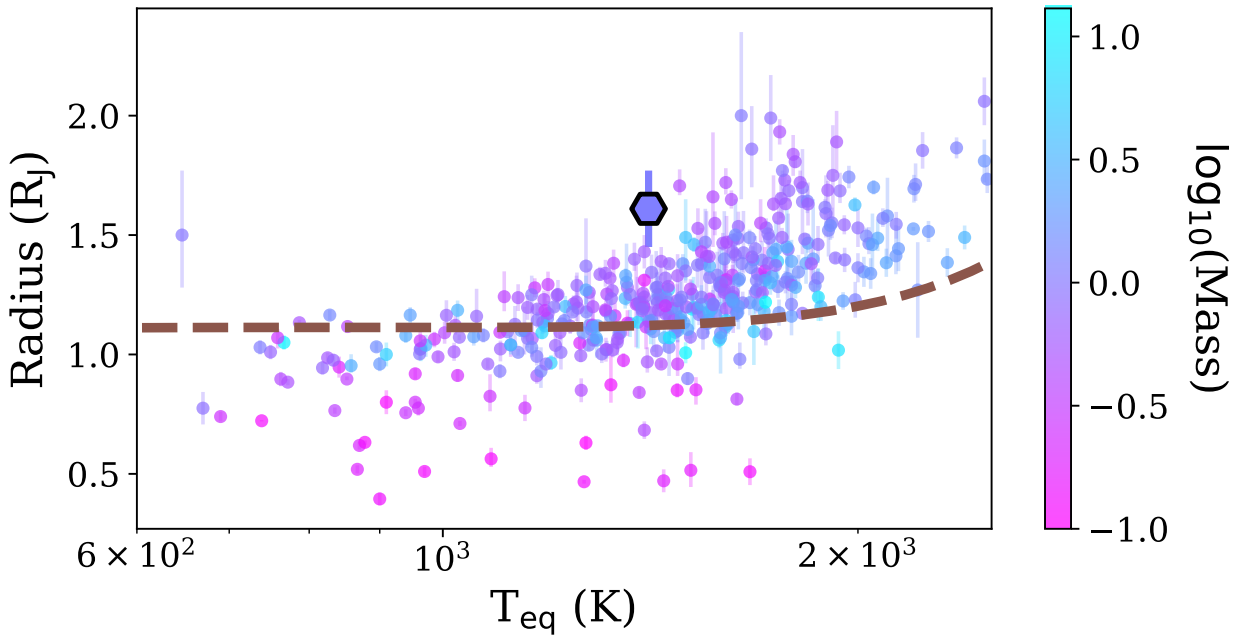

Figure 5.6: Exoplanets with masses ranging from 0.1 to 13 M_J, where both the masses and radii are determined to better than 20% precision taken from TEPCat (Southworth 2011). Each planet has been color-coded by its mass in $\log_{10}$ scale. The hexagon shows the position of NGTS-Nb. The dashed line shows an evolutionary model from Thorngren & Fortney (2018) for a Jovian planet without inflation-inducing effects.

5.3 Discussion

We place these planets in the context of other HJs using the well-studied catalog from TEPCat[7] (Southworth 2011). We studied the radius-equilibrium temperature diagram (Figure 5.6, adapted from Fortney et al. 2021) and, considering the 1σ error on the radii, we find that both planets are significantly above the expected evolution of a pure H/He, 1 M_J , and 4.5 Gyr HJ.

Thus it is reasonable to conclude that these planets indeed are inflated. The question, however, is how inflated are they?

5.3.1 Incident Flux

To answer this we start by studying the mass-radius diagram (Figure 5.7). In it, we can see that NGTS-Nb occupies quite an underpopulated region in the parameter space. Indeed, the neighboring stars in the 1σ region around the star have a mean equilibrium temperature of 1890±200 K, 2.4σ higher than that of NGTS-Nb.

The general consensus regarding the radius anomaly is that the main parameter driving inflation is the incident flux from the host star. A study from Thorngren & Fortney (2018) found that the conversion of incident flux to interior heating needed peaks at around 1600 K, and Hartman et al. (2016) finds that the radii of HJs correlate with the main sequence age of their host stars, providing further evidence that incident flux is one of the main culprits behind inflation. Finally, Demory & Seager (2011) and Miller & Fortney (2011)

[7] https://www.astro.keele.ac.uk/jkt/tepcat/

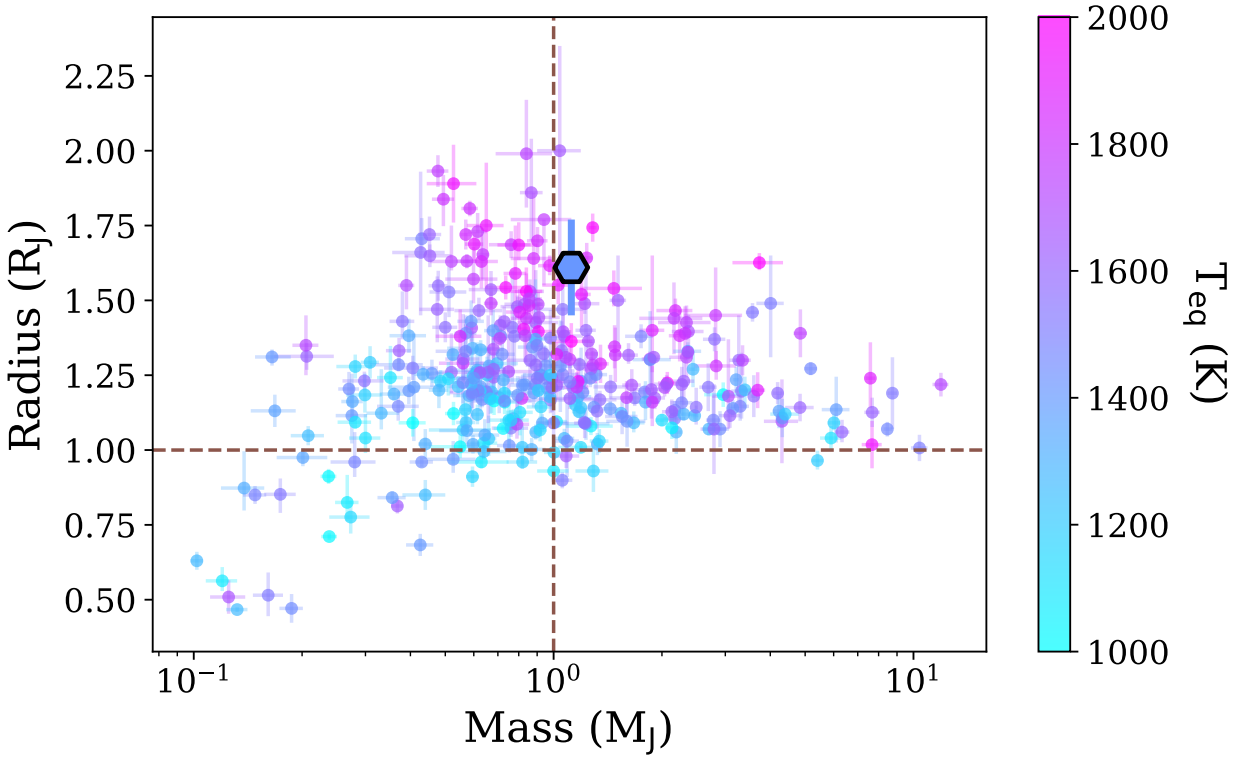

Figure 5.7: Exoplanets with masses ranging from 0.1 to 13 M_J, (where the masses and radii are determined to better than 20% precision), and equilibrium temperatures between 1000 and 2000 K. Each planet has been color-coded by its equilibrium temperature. The hexagon shows the position of NGTS-Nb. The error bars have been suppressed for clarity.

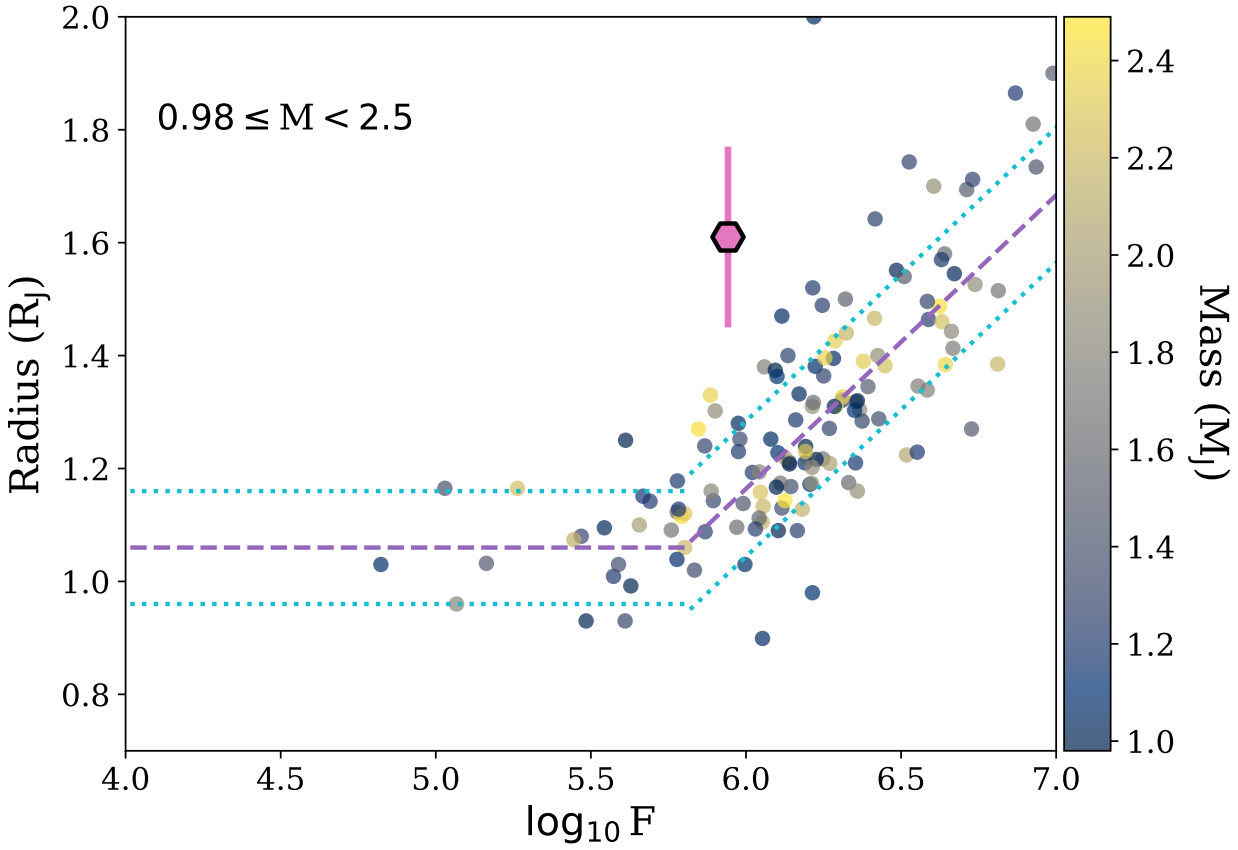

Figure 5.8: Inflated model according to Equation 5.1. NGTS-Nb is shown as a pink hexagon. It is clear that NGTS-Nb is significantly inflated.

established a flux threshold of 2×10^5 Wm^{-2} above which inflation occurs.

We turn to the work by Sestovic et al. (2018) (hereafter S18), who developed a hierarchical Bayesian model that relates the expected inflated radius of a planet, to the incident flux it receives. In their work, they also found a strong correlation between radius inflation and planetary mass, which resulted in four distinct models. The relevant model for this work is Equation 5.1, where F is the incident flux and ΔR is the expected radius inflation, under the mass regime of $0.98 \leq \mathrm{M} < 2.5$ M$_J$ and a baseline of 1.06 ± 0.03R$_J$.

$$\Delta R = (0.52 \pm 0.07) \cdot (\log_{10} F - 5.8) \tag{5.1}$$

We calculate the incident flux of NGTS-Nb to be $8.75^{+0.40}_{0.36} \times 10^5$. Using the previous equation, this results in a ΔR value of 0.07 ± 0.01.

Thus, the expected radius for NGTS-Nb reaches $1.13^{+0.14}_{-0.13}$R$_J$, a significantly lower value than the the observed radius. We contextualize these findings in Figure 5.8, where it is conclusively shown that NGTS-Nb is indeed inflated, and significantly so.

5.3.2 Other Mechanisms

There are other proposed mechanisms that could drive planetary radii inflation, such as gas giant planets having double-diffusive layered convection instead of fully convective atmospheres (Kurokawa & Inutsuka 2015), or the circularization of HJs formed through high eccentricity formation (Gu et al. 2019). Unfortunately, for most of these alternative models, they can not, by themselves, explain the observed distribution of HJs. Of course, there is no reason for a single mechanism to completely drive radius inflation, and indeed, Sarkis et al. (2021) has shown evidence for at least three separate mechanisms acting together.

Another avenue to explain inflated HJs is the possibility of re-inflation, either during the main-sequence, or post-main-sequence. Komacek et al. (2020) studied the reinflation of warm and hot Jupiters and concluded that HJs must evolve along with their host stars, and that the reinflation is greatest between one and ten Gyrs of evolution. Simulations done in their study suggest that for a planet to be as inflated as NGTS-Nb, heat must be deposited at pressures higher than 10^5 bars.

5.4 Conclusions

In this paper, we report the discovery of a new hot Jupiter: NGTS-Nb, from NGTS, *TESS*, PEST, LCO, and MEarth photometry and RV data from FEROS, orbiting the subgiant star NGTS-N. We found the planet to have a mass of 1.12 ± 0.12 M_J, and radius of 1.61 ± 0.16 R_J.

We studied the inflation of NGTS-Nb and found it to be significantly inflated, especially when compared with other HJs having similar radii and masses.

Considering its anomalous inflation with respect to its equilibrium temperatures, this planet highlights the uncomfortably large scatter in the inflation relations of HJs, and they can serve to test and refine existing models such as S18 or Baraffe et al. (2008).

Chapter 6

Summary and conclusions

Chapter 2 presents the discovery of NGTS-6b, a grazing transit ultra-short period hot Jupiter with a period of 21.17 hours, and the first discovery of its kind from NGTS. The joint photometry and radial velocity analysis reveals a planet with a mass of $1.339 \pm 0.028 M_J$ and a radius of $1.326^{+0.214}_{-0.210} R_J$. From the handful of ultra-short period planets in the literature, seven are giant planets with $R_p > 8 R_\oplus$ (WASP-18b, WASP-43b, WASP-103b, HATS-18b, KELT-16b, WASP-19b, and NGTS-10b), and therefore NGTS-6b represents a significant addition to this extreme population. NGTS-6b sits at the center of a distinct clump of ultra-short period hot Jupiters, adding weight to this emerging population.

Being such an extreme system, we investigated the effects of photoevaporation on the planet, applying empirical relations that link the X-ray and bolometric luminosities, L_X/L_{bol}, with stellar age. When used in conjunction with the isochrone-derived age of 9.77 Gyr, the model yields an estimate of $L_X/L_{bol} = 1 \times 10^{-5}$ at the current epoch. This is translated to an X-ray luminosity $L_X = 6 \times 10^{27}$ erg s^{-1}, or equivalently, a flux at Earth of 5×10^{-16} erg s^{-1}m^{-2}. This amount of flux would require a very deep observation with current-generation X-ray telescopes in order to detect the star. The energy-limited method of estimating atmosphere mass-loss yields a loss rate of 1×10^{11} gs^{-1}. Integrating this loss rate across the lifetime of the star, a total mass-loss of about 5% is estimated, which is not enough to have evolved the planet in any significant way.

NGTS-6 was found to likely be metal-rich, with a metallicity of [Fe/H] = 0.11 ± 0.09 dex. Gas giants favor metal-rich stars, with ultra-short period giants, including hot Jupiters, appearing to be even more metal-enhanced, especially when compared to warm Jupiters. Approximately 50% of the ultra-short period hot Jupiter planets host stars are found to be metal-rich ([Fe/H]≥0.1 dex), whereas the smaller super-Earth population, only 30% orbit such stars. Since the ultra-short period hot Jupiter sample is still much smaller than the super-Earth sample, NGTS-6b adds significant statistical weight to this group, and the conclusion that this points towards is that both of these populations form through core accretion processes, with the hot Jupiter sample forming at large separations, later migrating towards the host star, either through disk migration or high-eccentricity processes (such as planet-planet scattering).

In summary, NGTS-6b adds to an emerging group of ultra-short period hot Jupiters, adding significant weight that this is, indeed, a distinct population. Photoevaporation models suggest this planet has not gone through significant evolution, in line with theoretical studies of hot Jupiters. The stellar modeling revealed NGTS-6 is metal-rich, which follows the trend of gas giants favoring metal-rich stars. Finally, the existence

of this planet adds further evidence for the core accretion formation scenario, with an inwards migration through disk-driven interactions of high-eccentricity processes.

In Chapter 3 we presented a new methodology to model stellar SEDs leveraging Bayesian modeling and public archival photometry. The open-source `python` tool, called `ARIADNE`, is publicly available and utilizes Bayesian Model Averaging in order to account for several stellar atmosphere model grids and their different physical and geometrical assumptions.

We found the precision and accuracy of `ARIADNE` to be comparable to interferometric observations, with an RMS of 0.001±0.070, and a mean precision ranging from 2.1% to 4.3% depending on the model averaging method when compared against a set of 135 stars with interferometry observations. Paired with isochrone interpolation, the code can also calculate stellar masses and thus provide bulk densities.

While there are systematic differences between all of the employed models, emerging from the different assumed physics and geometries, these biases are mostly overcome when properly averaging the models' posteriors weighted with their Bayesian evidence. We do note, however, that this does not apply for either masses or ages derived through `ARIADNE`.

`ARIADNE` reaches peak performance when paired with spectroscopically derived priors, especially for parameters such as metallicity and surface gravity, two parameters that do not have a large effect on the overall shape of the SED.

Finally, we found that in the M dwarf regime, there is a systematic overestimation of the radius when compared to the interferometrically derived value, and while the effect is small (well within the 5% interferometric scatter), it shows a weak link in the endeavors of stellar modeling.

In Chapter 4 we present the discovery of HD 18599 b, a dense mini-Neptune orbiting young star (300 Myr) HD 18599. This planet sits on the edge of the Neptune desert, making HD 18599 b the youngest mini-Neptune discovered to date in this region. We found this planet to have a period of 4.137 days, a mass of 25.5±4.6$M_\oplus$, and a radius of 2.70±0.05$R_\oplus$. This results in a bulk density of 7.1±1.4 g cm^{-3}, an unusually high density. We compared this planet to several two-layer composition models and found that it could be composed of 23% H_2O, and 77% rock ($MgSiO_3$) and iron core, with the 1σ uncertainties allowing the water proportion to vary from 10 to 41%.

Using the structure model interpolator, `smint`, we further investigated the possible internal composition of HD 18599 b and found a water mass fraction of 0.3± 0.1, which agrees with the value from two-layer models. Unfortunately, the iron core mass fraction is widely unconstrained with a value of 0.4±0.3. Finally, the gas-to-ore mass ratio analysis shows that the planet has a 1^{+14}_{-1}% mass fraction in H/He. This argues for a steam atmosphere surrounding the planet.

The high mass regime in which HD 18599 b resides is poorly sampled, making it an ideal window into the physical and dynamical processes behind the evolution of young Neptunes and their interactions with active stars. Atmospheric studies of this planet would allow a deeper understanding of the inner composition of the planet, and the physics of young planetary atmospheres. Additional radial velocity measurements could allow for the possibility of discovering further companions in the system, especially since it is known that small planet systems commonly host more than one planet.

Being a young star, HD 18599 shows significant activity, both in its light curve and its radial velocity measurements, thus extracting the Keplerian signal produced by HD 18599 b was the biggest hurdle to

overcome. To this end, we tested several correlated noise models, including autoregression, moving average models, linear correlations with activity indices, and a combination of these techniques. In this case, linear correlations gave rise to a higher posterior probability, while autoregression and moving average models fell short of explaining the correlated noise, likely due to low observational cadence. This makes HD 18599 an ideal testbed for more sophisticated activity models, while simultaneously encouraging more radial velocity observations for this star to be pursued.

In Chapter 5 we present the discovery of NGTS-Nb, a hot Jupiter in a 4.16-day orbit with a mass and radius of $1.12\pm0.12 M_J$ and $1.61\pm0.16 R_J$ respectively. With a bulk density of 0.3 g m^{-3}, this planet is unusually inflated. In the context of hot Jupiters, NGTS-Nb occupies an underpopulated region in the radius-equilibrium temperature diagram. Considering the 1σ region, the equilibrium temperature of NGTS-Nb is 2.4σ away from the mean temperature of 1890 K. The general consensus surrounding the radius anomaly is that the incident flux is the main mechanism driving inflation. Using a hierarchical Bayesian model, we calculate the expected radius of NGTS-Nb to be $1.13^{+0.14}_{-0.13} R_J$, significantly below the measured $1.61 R_J$. This result is at odds with the idea that the incident flux is the main driver behind radius inflation, lending more evidence to recent works that have shown multiple mechanisms acting together.

Another mechanism that might be at play is re-inflation. It has been shown that hot Jupiters begin reinflating as the host star exits the main sequence. Considering NGTS-N appears to be slightly evolved, entering the sub-giant branch, the increased inflation of NGTS-Nb might be explained by re-inflation, however, we are unable to confidently ascertain if NGTS-Nb is consistent with such a scenario.

To summarize, NGTS-Nb is a newly discovered hot Jupiter that shows significant radius inflation for its incident flux. This anomalous planet poses a challenge to the current understanding of inflation models.

Bibliography

Acton, J. S., Goad, M. R., Casewell, S. L., et al. 2020, MNRAS, 498, 3115

Adams, E. R., Jackson, B., Endl, M., et al. 2017, AJ, 153, 82

Addison, B., Wright, D. J., Wittenmyer, R. A., et al. 2019, PASP, 131, 115003

Addison, B. C., Wright, D. J., Nicholson, B. A., et al. 2021a, MNRAS, 502, 3704

Addison, B. C., Horner, J., Wittenmyer, R. A., et al. 2021b, AJ, 162, 137

Agol, E., Steffen, J., Sari, R., & Clarkson, W. 2005, Monthly Notices of the Royal Astronomical Society, 359, 567

Aguichine, A., Mousis, O., Deleuil, M., & Marcq, E. 2021, ApJ, 914, 84

Ahrer, E., Queloz, D., Rajpaul, V. M., et al. 2021, MNRAS, 503, 1248

Alam, S., Albareti, F. D., Allende Prieto, C., et al. 2015, ApJS, 219, 12

Albrecht, S., Winn, J. N., Johnson, J. A., et al. 2012, ApJ, 757, 18

Allard, F., Homeier, D., & Freytag, B. 2012, Philosophical Transactions of the Royal Society A: Mathematical, Physical and Engineering Sciences, 370, 2765

Allende Prieto, C., Majewski, S. R., Schiavon, R., et al. 2008, Astronomische Nachrichten, 329, 1018

Alves, S., Benamati, L., Santos, N. C., et al. 2015, MNRAS, 448, 2749

Ambikasaran, S., Foreman-Mackey, D., Greengard, L., Hogg, D. W., & O'Neil, M. 2015, IEEE Transactions on Pattern Analysis and Machine Intelligence, 38, 252

Ammons, S. M., Robinson, S. E., Strader, J., et al. 2006, ApJ, 638, 1004

Anderson, E., & Francis, C. 2012a, Astronomy Letters, 38, 331

—. 2012b, Astronomy Letters, 38, 331

Anglada-Escudé, G., & Tuomi, M. 2015, Science, 347, 1080

Anglada-Escudé, G., Tuomi, M., Gerlach, E., et al. 2013, A&A, 556, A126

Anglada-Escudé, G., Amado, P. J., Barnes, J., et al. 2016, Nature, 536, 437

Armstrong, D. J., Lopez, T. A., Adibekyan, V., et al. 2020, Nature, 583, 39

Bailer-Jones, C. A. L., Rybizki, J., Fouesneau, M., Demleitner, M., & Andrae, R. 2021, AJ, 161, 147

Bailer-Jones, C. A. L., Rybizki, J., Fouesneau, M., Mantelet, G., & Andrae, R. 2018, AJ, 156, 58

Baines, E. K., McAlister, H. A., ten Brummelaar, T. A., et al. 2008, ApJ, 680, 728

Baines, E. K., White, R. J., Huber, D., et al. 2012, ApJ, 761, 57

Baraffe, I., Chabrier, G., & Barman, T. 2008, A&A, 482, 315

Barnes, S. A. 2007, ApJ, 669, 1167

Barnes, S. I., Gibson, S., Nield, K., & Cochrane, D. 2012, in Society of Photo-Optical Instrumentation Engineers (SPIE) Conference Series, Vol. 8446, Ground-based and Airborne Instrumentation for Astronomy IV, 844688

Bayo, A., Rodrigo, C., Barrado Y Navascués, D., et al. 2008, Astronomy and Astrophysics, 492, 277

Berger, D. H., Gies, D. R., McAlister, H. A., et al. 2006, The Astrophysical Journal, 644, 475

Bianchi, L., Herald, J., Efremova, B., et al. 2011a, Ap&SS, 335, 161

—. 2011b, Ap&SS, 335, 161

Bigot, L., Mourard, D., Berio, P., et al. 2011, A&A, 534, L3

Blackwell, D. E., & Lynas-Gray, A. E. 1998, A&AS, 129, 505

Bodenheimer, P., Lin, D. N. C., & Mardling, R. A. 2001, ApJ, 548, 466

Boisse, I., Bouchy, F., Hébrard, G., et al. 2011, A&A, 528, A4

Boisse, I., Moutou, C., Vidal-Madjar, A., et al. 2009, A&A, 495, 959

Borgniet, S., Perraut, K., Su, K., et al. 2019, Astronomy & Astrophysics, 627, A44

Boro Saikia, S., Marvin, C. J., Jeffers, S. V., et al. 2018, A&A, 616, A108

Bouchy, F., Udry, S., Mayor, M., et al. 2005, A&A, 444, L15

Bourges, L., Mella, G., Lafrasse, S., et al. 2017, VizieR Online Data Catalog, II/346

Boyajian, T., von Braun, K., Feiden, G. A., et al. 2015, MNRAS, 447, 846

Boyajian, T. S., von Braun, K., van Belle, G., et al. 2012, ApJ, 757, 112

Boyajian, T. S., McAlister, H. A., Van Belle, G., et al. 2012, Astrophysical Journal, 746, doi:10.1088/0004-637X/746/1/101

Boyajian, T. S., von Braun, K., van Belle, G., et al. 2013, ApJ, 771, 40

Brahm, R., Jordán, A., & Espinoza, N. 2017, Publications of the Astronomical Society of the Pacific, 129, 034002

Brasseur, C. E., Phillip, C., Fleming, S. W., Mullally, S. E., & White, R. L. 2019, Astrocut: Tools for creating cutouts of TESS images, Astrophysics Source Code Library, record ascl:1905.007, , , ascl:1905.007

Brewer, J. M., Fischer, D. A., Valenti, J. A., & Piskunov, N. 2016, The Astrophysical Journal Supplement Series, 225, 32. http://dx.doi.org/10.3847/0067-0049/225/2/32

Brown, T. M., Baliber, N., Bianco, F. B., et al. 2013, PASP, 125, 1031

Bryan, M. L., Knutson, H. A., Howard, A. W., et al. 2016, ApJ, 821, 89

Bryant, E. M., Bayliss, D., Nielsen, L. D., et al. 2020, MNRAS, 499, 3139

Buchner, J. 2016, Statistics and Computing, 26, 383

—. 2019, PASP, 131, 108005

—. 2021, The Journal of Open Source Software, 6, 3001

Buchner, J., Georgakakis, A., Nandra, K., et al. 2014, A&A, 564, A125

Burrows, A., Hubeny, I., Budaj, J., & Hubbard, W. B. 2007, ApJ, 661, 502

Cale, B. L., Reefe, M., Plavchan, P., et al. 2021, AJ, 162, 295

Calzetti, D. 2001, PASP, 113, 1449

Campbell, B., Walker, G. A. H., & Yang, S. 1988, ApJ, 331, 902

Cardelli, J. A., Clayton, G. C., & Mathis, J. S. 1989, ApJ, 345, 245

Casagrande, L., Schönrich, R., Asplund, M., et al. 2011, A&A, 530, A138

Castelli, F., & Kurucz, R. L. 2003, in IAU Symposium, Vol. 210, Modelling of Stellar Atmospheres, ed. N. Piskunov, W. W. Weiss, & D. F. Gray, A20

Chambers, K. C., Magnier, E. A., Metcalfe, N., et al. 2016a, arXiv e-prints, arXiv:1612.05560

—. 2016b, arXiv e-prints, arXiv:1612.05560

Charbonneau, D., Brown, T. M., Latham, D. W., & Mayor, M. 2000, ApJL, 529, L45

Charbonneau, D., Brown, T. M., Noyes, R. W., & Gilliland, R. L. 2002, ApJ, 568, 377

Chatterjee, S., Ford, E. B., Matsumura, S., & Rasio, F. A. 2008, ApJ, 686, 580

Collier Cameron, A., Pollacco, D., Street, R. A., et al. 2006, MNRAS, 373, 799

Coppejans, R., Gulbis, A. A. S., Kotze, M. M., et al. 2013, Publications of the Astronomical Society of the Pacific, 125, 976

Crane, J. D., Shectman, S. A., Butler, R. P., et al. 2010, in Proc. SPIE, Vol. 7735, Ground-based and Airborne Instrumentation for Astronomy III, 773553

Crepp, J. R., Johnson, J. A., Fischer, D. A., et al. 2012, ApJ, 751, 97

Dall, T. H., Santos, N. C., Arentoft, T., Bedding, T. R., & Kjeldsen, H. 2006, A&A, 454, 341

Dawson, R. I., & Johnson, J. A. 2018, ARA&A, 56, 175

de Leon, J. P., Livingston, J. H., Jenkins, J. S., et al. 2023, MNRAS, 522, 750

Delgado Mena, E., Tsantaki, M., Adibekyan, V. Z., et al. 2017, A&A, 606, A94

Demangeon, O. D. S., Faedi, F., Hébrard, G., et al. 2018, A&A, 610, A63

Demory, B.-O., & Seager, S. 2011, ApJS, 197, 12

Díaz, M. R., Jenkins, J. S., Feng, F., et al. 2020a, MNRAS, 496, 4330

Díaz, M. R., Jenkins, J. S., Gand olfi, D., et al. 2020b, MNRAS, 252

Dotter, A. 2016, ApJS, 222, 8

Dumusque, X., Udry, S., Lovis, C., Santos, N. C., & Monteiro, M. J. P. F. G. 2011, A&A, 525, A140

Durisen, R. H., Boss, A. P., Mayer, L., et al. 2007, in Protostars and Planets V, ed. B. Reipurth, D. Jewitt, & K. Keil, 607

Eastman, J. D., Rodriguez, J. E., Agol, E., et al. 2019, arXiv e-prints, arXiv:1907.09480

Edelson, R. A., & Krolik, J. H. 1988, ApJ, 333, 646

Erkaev, N. V., Kulikov, Y. N., Lammer, H., et al. 2007, A&A, 472, 329

Erspamer, D., & North, P. 2003, A&A, 398, 1121

Espinoza, N. 2018, Research Notes of the American Astronomical Society, 2, 209

Espinoza, N., & Jordán, A. 2016, MNRAS, 457, 3573

Espinoza, N., Kossakowski, D., & Brahm, R. 2019, MNRAS, 490, 2262

Espinoza, N., Bayliss, D., Hartman, J. D., et al. 2016, The Astronomical Journal, 152, 108

Esteves, L. J., De Mooij, E. J. W., & Jayawardhana, R. 2015, ApJ, 804, 150

Feinstein, A. D., Montet, B. T., Foreman-Mackey, D., et al. 2019, PASP, 131, 094502

Feng, F., Tuomi, M., Jones, H. R. A., et al. 2017, AJ, 154, 135

Feroz, F., Hobson, M. P., & Bridges, M. 2009, MNRAS, 398, 1601

Fischer, D. A., & Valenti, J. 2005, ApJ, 622, 1102

Fischer, D. A., & Valenti, J. 2005, The Astrophysical Journal, 622, 1102. http://stacks.iop.org/0004-637X/622/i=2/a=1102

Fitzpatrick, E. L. 1999, PASP, 111, 63

Flowers, E., Brogi, M., Rauscher, E., Kempton, E. M. R., & Chiavassa, A. 2019, AJ, 157, 209

Ford, E. B., Havlickova, M., & Rasio, F. A. 2001, Icarus, 150, 303

Ford, E. B., & Rasio, F. A. 2008, ApJ, 686, 621

Foreman-Mackey, D. 2016, The Journal of Open Source Software, 24, doi:10.21105/joss.00024. http://dx.doi.org/10.5281/zenodo.45906

Foreman-Mackey, D. 2018, Research Notes of the American Astronomical Society, 2, 31

Foreman-Mackey, D., Agol, E., Ambikasaran, S., & Angus, R. 2017a, AJ, 154, 220

—. 2017b, AJ, 154, 220

Foreman-Mackey, D., Hogg, D. W., Lang, D., & Goodman, J. 2013, PASP, 125, 306

Fortney, J. J., Dawson, R. I., & Komacek, T. D. 2021, Journal of Geophysical Research (Planets), 126, e06629

Fragoso, T. M., Bertoli, W., & Louzada, F. 2018, International Statistical Review, 86, 1

Fulton, B. J., Petigura, E. A., Blunt, S., & Sinukoff, E. 2018, PASP, 130, 044504

Gaia Collaboration, Prusti, T., de Bruijne, J. H. J., et al. 2016, A&A, 595, A1

Gaia Collaboration, Brown, A. G. A., Vallenari, A., et al. 2018, A&A, 616, A1

Gaia Collaboration, Vallenari, A., Brown, A. G. A., et al. 2023, A&A, 674, A1

Gelman, A., Carlin, J. B., Stern, H. S., & Rubin, D. B. 2014, Journal of the American Statistical Association, 109, 1325

Gilbert, E. A., Barclay, T., Schlieder, J. E., et al. 2020, AJ, 160, 116

Giles, H. A. C., Collier Cameron, A., & Haywood, R. D. 2017, MNRAS, 472, 1618

Gill, S., Cooke, B. F., Bayliss, D., et al. 2020, MNRAS, 495, 2713

Gillen, E., Hillenbrand, L. A., David, T. J., et al. 2017, ApJ, 849, 11

Gonzalez, G. 1997, MNRAS, 285, 403

Goodman, J., & Weare, J. 2010, Communications in Applied Mathematics and Computational Science, 5, 65

Grandjean, A., Lagrange, A. M., Keppler, M., et al. 2020, A&A, 633, A44

Grandjean, A., Lagrange, A. M., Meunier, N., et al. 2021, A&A, 650, A39

Gray, R. O., Corbally, C. J., Garrison, R. F., McFadden, M. T., & Robinson, P. E. 2003, AJ, 126, 2048

Gu, P.-G., Peng, D.-K., & Yen, C.-C. 2019, ApJ, 887, 228

Günther, M. N., & Daylan, T. 2019, Allesfitter: Flexible Star and Exoplanet Inference From Photometry and Radial Velocity, Astrophysics Source Code Library, , , ascl:1903.003

—. 2021a, ApJS, 254, 13

—. 2021b, ApJS, 254, 13

Hartman, J. D., Bakos, G. Á., Bhatti, W., et al. 2016, AJ, 152, 182

Hatzes, A. P., Cochran, W. D., Endl, M., et al. 2003, ApJ, 599, 1383

Hauschildt, P. H., Allard, F., & Baron, E. 1999, The Astrophysical Journal, 629, 865

Heiter, U., Jofré, P., Gustafsson, B., et al. 2015, A&A, 582, A49

Hekker, S., & Meléndez, J. 2007, A&A, 475, 1003

Henden, A., & Munari, U. 2014, Contributions of the Astronomical Observatory Skalnate Pleso, 43, 518

Henry, G. W., Marcy, G. W., Butler, R. P., & Vogt, S. S. 2000, ApJL, 529, L41

Higson, E., Handley, W., Hobson, M., & Lasenby, A. 2019, Statistics and Computing, 29, 891. https://doi.org/10.1007/s11222-018-9844-0

Hippke, M., & Heller, R. 2019, A&A, 623, A39

Høg, E., Fabricius, C., Makarov, V. V., et al. 2000, A&A, 355, L27

Holczer, T., Mazeh, T., Nachmani, G., et al. 2016, The Astrophysical Journal Supplement Series, 225, 9

Hou, F., Goodman, J., Hogg, D. W., Weare, J., & Schwab, C. 2012, ApJ, 745, 198

Houdebine, É. R., Mullan, D. J., Doyle, J. G., et al. 2019, The Astronomical Journal, 158, 56

Huang, C. X., Vanderburg, A., Pál, A., et al. 2020a, Research Notes of the American Astronomical Society, 4, 204

—. 2020b, Research Notes of the American Astronomical Society, 4, 206

Huber, D., Ireland, M. J., Bedding, T. R., et al. 2012, ApJ, 760, 32

Huber, D., Bryson, S. T., Haas, M. R., et al. 2016, The Astrophysical Journal Supplement Series, 224, 2. http://dx.doi.org/10.3847/0067-0049/224/1/2

Husser, T.-O., von Berg, S. W., Dreizler, S., et al. 2013, Astronomy & Astrophysics, 553, A6. http://arxiv.org/abs/1303.5632{%}0Ahttp://dx.doi.org/10.1051/0004-6361/201219058

Hyndman, R. J. 1996, The American Statistician, 50, 120. http://www.jstor.org/stable/2684423

Irwin, J. M., Berta-Thompson, Z. K., Charbonneau, D., et al. 2015, in Cambridge Workshop on Cool Stars, Stellar Systems, and the Sun, Vol. 18, 18th Cambridge Workshop on Cool Stars, Stellar Systems, and the Sun, 767–772

Irwin, M. J., Lewis, J., Hodgkin, S., et al. 2004, in Society of Photo-Optical Instrumentation Engineers (SPIE) Conference Series, Vol. 5493, Optimizing Scientific Return for Astronomy through Information Technologies, ed. P. J. Quinn & A. Bridger, 411–422

Jackman, J. A. G., Wheatley, P. J., Bayliss, D., et al. 2019, MNRAS, 489, 5146

Jackson, A. P., Davis, T. A., & Wheatley, P. J. 2012, MNRAS, 422, 2024

Jackson, D. G., Watson, C. A., de Mooij, E. J. W., et al. 2023, MNRAS, 518, 4845

Jenkins, J. M., Twicken, J., Tenenbaum, P., et al. 2020a, in American Astronomical Society Meeting Abstracts, Vol. 235, American Astronomical Society Meeting Abstracts #235, 327.02

Jenkins, J. M., Twicken, J. D., McCauliff, S., et al. 2016a, in Proc. SPIE, Vol. 9913, Software and Cyberinfrastructure for Astronomy IV, 99133E

Jenkins, J. S., Jones, H. R. A., Pavlenko, Y., et al. 2008, A&A, 485, 571

Jenkins, J. S., & Tuomi, M. 2014, ApJ, 794, 110

Jenkins, J. S., Murgas, F., Rojo, P., et al. 2011, A&A, 531, A8

Jenkins, J. S., Jones, H. R. A., Tuomi, M., et al. 2016b, ArXiv e-prints, arXiv:1603.09391

—. 2017, MNRAS, 466, 443

Jenkins, J. S., Díaz, M. R., Kurtovic, N. T., et al. 2020b, Nature Astronomy, arXiv:2009.12832

Jofré, P., Heiter, U., Soubiran, C., et al. 2014, A&A, 564, A133

—. 2015, A&A, 582, A81

Jofré, P., Heiter, U., Worley, C. C., et al. 2017, A&A, 601, A38

Johnson, J. A., Huber, D., Boyajian, T., et al. 2014, Astrophysical Journal, 794, doi:10.1088/0004-637X/794/1/15

Jordán, A., Brahm, R., Espinoza, N., et al. 2020a, AJ, 159, 145

—. 2020b, AJ, 159, 145

Kane, S. R., Bean, J. L., Campante, T. L., et al. 2021, PASP, 133, 014402

Kaufer, A., Stahl, O., Tubbesing, S., et al. 1999, The Messenger, 95, 8

Kharchenko, N. V. 2001, Kinematika i Fizika Nebesnykh Tel, 17, 409

Kipping, D. M. 2013, MNRAS, 435, 2152

Kipping, D. M. 2016, Monthly Notices of the Royal Astronomical Society, 455, 1680

Komacek, T. D., Thorngren, D. P., Lopez, E. D., & Ginzburg, S. 2020, ApJ, 893, 36

Konacki, M., Torres, G., Jha, S., & Sasselov, D. D. 2003, Nature, 421, 507

Kovács, G., Zucker, S., & Mazeh, T. 2002, Astronomy and Astrophysics, 391, 369. https://ui.adsabs.harvard.edu/abs/2002A&A...391..369K/abstract

Kovács, G., Zucker, S., & Mazeh, T. 2002, A&A, 391, 369

Kreidberg, L. 2015, PASP, 127, 1161

Kreidberg, L., Line, M. R., Bean, J. L., et al. 2015, ApJ, 814, 66

Kunder, A., Kordopatis, G., Steinmetz, M., et al. 2017, AJ, 153, 75

Kurokawa, H., & Inutsuka, S.-i. 2015, ApJ, 815, 78

Kurucz, R. 1993, ATLAS9 Stellar Atmosphere Programs and 2 km/s grid. Kurucz CD-ROM No. 13. Cambridge, 13

Lachaume, R., Rabus, M., Jordán, A., et al. 2019, Monthly Notices of the Royal Astronomical Society, 484, 2656

Lange, J. U. 2023, MNRAS, 525, 3181

Lebzelter, T., Heiter, U., Abia, C., et al. 2012, Astronomy and Astrophysics, 547, 1

Leconte, J., Chabrier, G., Baraffe, I., & Levrard, B. 2010, A&A, 516, A64

Lee, E. J., & Chiang, E. 2017, ApJ, 842, 40

Li, L., Jiang, X., West, R. A., et al. 2018, Nature Communications, 9, 3709

Ligi, R., Creevey, O., Mourard, D., et al. 2016, Astronomy and Astrophysics, 586, doi:10.1051/0004-6361/201527054

Ligi, R., Dorn, C., Crida, A., et al. 2019, Astronomy and Astrophysics, 631, 1

Lithwick, Y., Xie, J., & Wu, Y. 2012, The Astrophysical Journal, 761, 122

Liu, Y. J., Zhao, G., Shi, J. R., Pietrzyński, G., & Gieren, W. 2007, MNRAS, 382, 553

Lomb, N. R. 1976, Ap&SS, 39, 447

Lopez, E. D., & Fortney, J. J. 2014, ApJ, 792, 1

López-Morales, M., Haywood, R. D., Coughlin, J. L., et al. 2016, AJ, 152, 204

Lovis, C., Dumusque, X., Santos, N. C., et al. 2011, arXiv e-prints, arXiv:1107.5325

Lundkvist, M. S., Kjeldsen, H., Albrecht, S., et al. 2016, Nature Communications, 7, 11201

Luque, R., Nowak, G., Pallé, E., et al. 2019, A&A, 623, A114

M. Green, G. 2018, The Journal of Open Source Software, 3, 695

Maldonado, J., Villaver, E., & Eiroa, C. 2018, A&A, 612, A93

Mallik, S. V., Parthasarathy, M., & Pati, A. K. 2003, A&A, 409, 251

Mamajek, E. E., & Hillenbrand, L. A. 2008, ApJ, 687, 1264

Mandel, K., & Agol, E. 2002, ApJL, 580, L171

Mandell, A. M., Raymond, S. N., & Sigurdsson, S. 2007, ApJ, 660, 823

Martínez-Arnáiz, R., Maldonado, J., Montes, D., Eiroa, C., & Montesinos, B. 2010, A&A, 520, A79

Massarotti, A., Latham, D. W., Stefanik, R. P., & Fogel, J. 2008, AJ, 135, 209

Matsuo, T., Shibai, H., Ootsubo, T., & Tamura, M. 2007, ApJ, 662, 1282

Maxted, P. F. L., Anderson, D. R., Collier Cameron, A., et al. 2011, PASP, 123, 547

Mayo, A. W., Rajpaul, V. M., Buchhave, L. A., et al. 2019, The Astronomical Journal, 158, 165. https://doi.org/10.3847%2F1538-3881%2Fab3e2f

Mayor, M., & Queloz, D. 1995, Nature, 378, 355

Mayor, M., Pepe, F., Queloz, D., et al. 2003, The Messenger, 114, 20

Mayor, M., Udry, S., Lovis, C., et al. 2009, A&A, 493, 639

Mazeh, T., Holczer, T., & Faigler, S. 2016, Astronomy and Astrophysics, 589, A75

McCormac, J., Gillen, E., Jackman, J. A. G., et al. 2020, MNRAS, 493, 126

McQuillan, A., Mazeh, T., & Aigrain, S. 2013, ApJL, 775, L11

Milbourne, T. W., Haywood, R. D., Phillips, D. F., et al. 2019, ApJ, 874, 107

Miller, N., & Fortney, J. J. 2011, ApJL, 736, L29

Mizuno, H. 1980, Progress of Theoretical Physics, 64, 544

Mortier, A., Santos, N. C., Sousa, S. G., et al. 2013, Astronomy and Astrophysics, 557, 1

Morton, T. D. 2015, isochrones: Stellar model grid package, , , ascl:1503.010

Mozurkewich, D., Armstrong, J. T., Hindsley, R. B., et al. 2003, AJ, 126, 2502

Murray-Clay, R. A., Chiang, E. I., & Murray, N. 2009, ApJ, 693, 23

Nordgren, T. E., Germain, M. E., Benson, J. A., et al. 1999, AJ, 118, 3032

Öberg, K. I., Cleeves, L. I., & Loomis, R. 2018, in Astronomical Society of the Pacific Conference Series, Vol. 517, Science with a Next Generation Very Large Array, ed. E. Murphy, 223

Oberst, T. E., Rodriguez, J. E., Colón, K. D., et al. 2017, AJ, 153, 97

O'Donnell, J. E. 1994, ApJ, 422, 158

Olmschenk, G., Ishitani Silva, S., Rau, G., et al. 2021, AJ, 161, 273

O'Toole, S. J., Tinney, C. G., & Jones, H. R. A. 2008, MNRAS, 386, 516

Owen, J. E., & Jackson, A. P. 2012, MNRAS, 425, 2931

Owen, J. E., & Lai, D. 2018, Monthly Notices of the Royal Astronomical Society, 479, 5012

Palle, E., Nowak, G., Luque, R., et al. 2019, A&A, 623, A41

Papaloizou, J. C. B., & Terquem, C. 2001, MNRAS, 325, 221

Parmentier, V., Fortney, J. J., Showman, A. P., Morley, C., & Marley, M. S. 2016, ApJ, 828, 22

Parviainen, H. 2015, MNRAS, 450, 3233

Patra, K. C., Winn, J. N., Holman, M. J., et al. 2020, AJ, 159, 150

Paunzen, E. 2015, A&A, 580, A23

Peña Rojas, P. A., & Jenkins, J. S. 2018, A&A, in prep

Penev, K., Hartman, J. D., Bakos, G. Á., et al. 2016, AJ, 152, 127

Pepe, F., Mayor, M., Rupprecht, G., et al. 2002, The Messenger, 110, 9

Pepe, F., Cristiani, S., Rebolo, R., et al. 2020, arXiv e-prints, arXiv:2010.00316

Perryman, M. 2011, The Exoplanet Handbook (Cambridge University Press), doi:10.1017/CBO9780511994852

Perryman, M. 2018, The Exoplanet Handbook

Petrovich, C., Deibert, E., & Wu, Y. 2018, arXiv e-prints, arXiv:1804.05065

Piaulet, C., Benneke, B., Rubenzahl, R. A., et al. 2021, AJ, 161, 70

Pollacco, D. L., Skillen, I., Collier Cameron, A., et al. 2006a, PASP, 118, 1407

—. 2006b, PASP, 118, 1407

Pollack, J. B., Hubickyj, O., Bodenheimer, P., et al. 1996, Icarus, 124, 62

Pope, B. J. S., Parviainen, H., & Aigrain, S. 2016, MNRAS, 461, 3399

Queloz, D. 1995, Symposium - International Astronomical Union, 167, 221–229

Queloz, D., Henry, G. W., Sivan, J. P., et al. 2001a, A&A, 379, 279

Queloz, D., Mayor, M., Udry, S., et al. 2001b, The Messenger, 105, 1

Quirrenbach, A., Amado, P. J., Caballero, J. A., et al. 2016, in Society of Photo-Optical Instrumentation Engineers (SPIE) Conference Series, Vol. 9908, Ground-based and Airborne Instrumentation for Astronomy VI, ed. C. J. Evans, L. Simard, & H. Takami, 990812

Rafikov, R. R. 2005, ApJL, 621, L69

Rains, A. D., Ireland, M. J., White, T. R., Casagrande, L., & Karovicova, I. 2020, MNRAS, 493, 2377

Rajpaul, V., Aigrain, S., Osborne, M. A., Reece, S., & Roberts, S. 2015, MNRAS, 452, 2269

Ramírez, I., Allende Prieto, C., & Lambert, D. L. 2013, ApJ, 764, 78

Rasio, F. A., & Ford, E. B. 1996, Science, 274, 954

Reiners, A., Bean, J. L., Huber, K. F., et al. 2010, ApJ, 710, 432

Ricker, G. R., Winn, J. N., Vanderspek, R., et al. 2015, Journal of Astronomical Telescopes, Instruments, and Systems, 1, 014003

Robert, C., & Casella, G. 2011, Statistical Science, 26, 102

Robertson, P., Mahadevan, S., Endl, M., & Roy, A. 2014, Science, 345, 440

Rojas-Ayala, B., Covey, K. R., Muirhead, P. S., & Lloyd, J. P. 2012, ApJ, 748, 93

Royer, F., Zorec, J., & Gómez, A. E. 2007, A&A, 463, 671

Saar, S. H. 1998, in Astronomical Society of the Pacific Conference Series, Vol. 154, Cool Stars, Stellar Systems, and the Sun, ed. R. A. Donahue & J. A. Bookbinder, 211

Sanchis-Ojeda, R., Rappaport, S., Winn, J. N., et al. 2014, ApJ, 787, 47

Sandford, E., Espinoza, N., Brahm, R., & Jordán, A. 2019, Monthly Notices of the Royal Astronomical Society, 489, 3149. https://doi.org/10.1093/mnras/stz2348

Santos, N. C., Israelian, G., & Mayor, M. 2004, A&A, 415, 1153

Santos, N. C., Mayor, M., Queloz, D., & Udry, S. 2002, The Messenger, 110, 32

Santos, N. C., Mortier, A., Faria, J. P., et al. 2014, A&A, 566, A35

Sarkis, P., Mordasini, C., Henning, T., Marleau, G. D., & Mollière, P. 2021, A&A, 645, A79

Scargle, J. D. 1982, ApJ, 263, 835

Scarsdale, N., Murphy, J. M. A., Batalha, N. M., et al. 2021, AJ, 162, 215

Schlafly, E. F., & Finkbeiner, D. P. 2011, Astrophysical Journal, 737, doi:10.1088/0004-637X/737/2/103

Schlegel, D. J., Finkbeiner, D. P., & Davis, M. 1998, ApJ, 500, 525

Schwarzschild, K., & Villiger, W. 1906, ApJ, 23, 284

Seager, S., & Mallén-Ornelas, G. 2003, ApJ, 585, 1038

Sestovic, M., Demory, B.-O., & Queloz, D. 2018, A&A, 616, A76

Simpson, E. R., Fetherolf, T., Kane, S. R., et al. 2022, AJ, 163, 215

Sing, D. K., Fortney, J. J., Nikolov, N., et al. 2016, Nature, 529, 59

Skilling, J. 2004, in American Institute of Physics Conference Series, Vol. 735, American Institute of Physics Conference Series, ed. R. Fischer, R. Preuss, & U. V. Toussaint, 395–405

Skilling, J. 2006, Bayesian Anal., 1, 833. https://doi.org/10.1214/06-BA127

Skrutskie, M. F., Cutri, R. M., Stiening, R., et al. 2006, AJ, 131, 1163

Smith, A. M. S., Acton, J. S., Anderson, D. R., et al. 2021, A&A, 646, A183

Sneden, C. A. 1973, PhD thesis, THE UNIVERSITY OF TEXAS AT AUSTIN.

Soto, M. G., & Jenkins, J. S. 2018, A&A, 615, A76

Soto, M. G., Jones, M. I., & Jenkins, J. S. 2021, A&A, 647, A157

Soubiran, C., Le Campion, J. F., Brouillet, N., & Chemin, L. 2016, Astronomy and Astrophysics, 591, 1

Southworth, J. 2011, MNRAS, 417, 2166

Southworth, J., Hinse, T. C., Dominik, M., et al. 2009, ApJ, 707, 167

Southworth, J., Mancini, L., Ciceri, S., et al. 2015, MNRAS, 447, 711

Speagle, J. S. 2019, arXiv e-prints, arXiv:1904.02180

—. 2020, MNRAS, 493, 3132

Spitzer Science, C. 2009, VizieR Online Data Catalog, II/293

Stassun, K. G., Collins, K. A., & Gaudi, B. S. 2017, AJ, 153, 136

Stassun, K. G., Oelkers, R. J., Pepper, J., et al. 2018, AJ, 156, 102

Steffen, J. H., Ragozzine, D., Fabrycky, D. C., et al. 2012, Proceedings of the National Academy of Sciences, 109, 7982

Stevenson, K. B., Line, M. R., Bean, J. L., et al. 2017, AJ, 153, 68

Stokholm, A., Nissen, P. E., Aguirre, V. S., et al. 2019, Monthly Notices of the Royal Astronomical Society, 12, 1

Storch, N. I., Anderson, K. R., & Lai, D. 2014, Science, 345, 1317

Szabó, G. M., & Kiss, L. L. 2011, The Astrophysical Journal, 727, L44

Tamuz, O., Mazeh, T., & Zucker, S. 2005, Monthly Notices of the Royal Astronomical Society, 356, 1466. https://academic.oup.com/mnras/article/356/4/1466/1014047

Tamuz, O., Mazeh, T., & Zucker, S. 2005, MNRAS, 356, 1466

Tanner, A., Boyajian, T. S., Von Braun, K., et al. 2015, Astrophysical Journal, 800, 0

Tayar, J., Claytor, Z. R., Huber, D., & van Saders, J. 2020, arXiv e-prints, arXiv:2012.07957

Terquem, C. 2014, MNRAS, 444, 1738

Teske, J. K., Thorngren, D., Fortney, J. J., Hinkel, N., & Brewer, J. M. 2019, AJ, 158, 239

Thorngren, D. P., & Fortney, J. J. 2018, AJ, 155, 214

Thorngren, D. P., Fortney, J. J., Murray-Clay, R. A., & Lopez, E. D. 2016, ApJ, 831, 64

Tilbrook, R. H., Burleigh, M. R., Costes, J. C., et al. 2021, MNRAS, arXiv:2103.10302

Toledo-Padrón, B., Suárez Mascareño, A., González Hernández, J. I., et al. 2021, A&A, 648, A20

Toner, C. G., & Gray, D. F. 1988, ApJ, 334, 1008

Tonry, J. L., Stubbs, C. W., Lykke, K. R., et al. 2012, ApJ, 750, 99

Torres, C. A. O., Quast, G. R., da Silva, L., et al. 2006, A&A, 460, 695

Torres, G., Andersen, J., & Giménez, A. 2010, A&A Rv, 18, 67

Torres, G., Winn, J. N., & Holman, M. J. 2008, ApJ, 677, 1324

Triaud, A. H. M. J. 2018, in Handbook of Exoplanets, ed. H. J. Deeg & J. A. Belmonte, 2

Tuomi, M., Anglada-Escudé, G., Gerlach, E., et al. 2013a, A&A, 549, A48

Tuomi, M., Jones, H. R. A., Barnes, J. R., Anglada-Escudé, G., & Jenkins, J. S. 2014, MNRAS, 441, 1545

Tuomi, M., Jones, H. R. A., Jenkins, J. S., et al. 2013b, A&A, 551, A79

Vach, S., Quinn, S. N., Vanderburg, A., et al. 2021, arXiv e-prints, arXiv:2111.02416

van Belle, G. T., & von Braun, K. 2009, ApJ, 694, 1085

van Leeuwen, F. 2007, A&A, 474, 653

VanderPlas, J. T. 2018, The Astrophysical Journal Supplement Series, 236, 16. https://doi.org/10.3847%2F1538-4365%2Faab766

Vines, J. I., & Jenkins, J. S. 2022, MNRAS, 513, 2719

Vines, J. I., Jenkins, J. S., Acton, J. S., et al. 2019, MNRAS, 489, 4125

Vogt, S. S. 2002, in Astronomical Society of the Pacific Conference Series, Vol. 270, Astronomical Instrumentation and Astrophysics, ed. F. N. Bash & C. Sneden, 5

Vogt, S. S., Butler, R. P., Rivera, E. J., et al. 2010, ApJ, 723, 954

von Braun, K., Boyajian, T. S., ten Brummelaar, T. A., et al. 2011, ApJ, 740, 49

von Braun, K., Boyajian, T. S., van Belle, G. T., et al. 2014, MNRAS, 438, 2413

Wang, J., & Fischer, D. A. 2015, AJ, 149, 14

Watson, A. J., Donahue, T. M., & Walker, J. C. G. 1981, Icarus, 48, 150

Weiss, L. M., Marcy, G. W., Rowe, J. F., et al. 2013, ApJ, 768, 14

West, R. G., Gillen, E., Bayliss, D., et al. 2019, Monthly Notices of the Royal Astronomical Society, 486, 5094

Wheatley, P. J., West, R. G., Goad, M. R., et al. 2018, Monthly Notices of the Royal Astronomical Society, 475, 4476

White, T. R., Huber, D., Mann, A. W., et al. 2018, Monthly Notices of the Royal Astronomical Society, 477, 4403

Wilson, O. C. 1978, ApJ, 226, 379

Winn, J. N. 2010, arXiv e-prints, arXiv:1001.2010

Winn, J. N., Sanchis-Ojeda, R., & Rappaport, S. 2018, arXiv e-prints, arXiv:1803.03303

Winn, J. N., Matthews, J. M., Dawson, R. I., et al. 2011, ApJL, 737, L18

Winn, J. N., Sanchis-Ojeda, R., Rogers, L., et al. 2017, The Astronomical Journal, 154, 60. https://doi.org/10.3847%2F1538-3881%2Faa7b7c

Wolszczan, A., & Frail, D. A. 1992, Nature, 355, 145

Wright, E. L., Eisenhardt, P. R. M., Mainzer, A. K., et al. 2010, AJ, 140, 1868

Wright, J. T. 2005, PASP, 117, 657

Wright, J. T., Marcy, G. W., Butler, R. P., & Vogt, S. S. 2004, ApJS, 152, 261

Wright, J. T., Marcy, G. W., Howard, A. W., et al. 2012, ApJ, 753, 160

Yee, S. W., Petigura, E. A., & von Braun, K. 2017, ApJ, 836, 77

Yee, S. W., Winn, J. N., Knutson, H. A., et al. 2019, The Astrophysical Journal Letters, 888, L5

Zacharias, N., Finch, C. T., Girard, T. M., et al. 2013, AJ, 145, 44

Zechmeister, M., & Kürster, M. 2009, A&A, 496, 577

Zechmeister, M., Reiners, A., Amado, P. J., et al. 2018, Astronomy and Astrophysics, 609, arXiv:1710.10114

Zeng, L., Sasselov, D. D., & Jacobsen, S. B. 2016, ApJ, 819, 127

Zeng, L., Jacobsen, S. B., Sasselov, D. D., et al. 2019, Proceedings of the National Academy of Sciences, 116, 9723. https://www.pnas.org/content/116/20/9723

Zhou, G., Huang, C. X., Bakos, G. Á., et al. 2019, AJ, 158, 141

Ziegler, C., Tokovinin, A., Briceño, C., et al. 2020, AJ, 159, 19

Ziegler, C., Tokovinin, A., Latiolais, M., et al. 2021, AJ, 162, 192